Abstract of "Mechanics and Molecular Mechanisms in Bio-Nano-Systems"

by Xuliang Qian, Ph.D., Brown University, Feb 2022

How nanomaterials interact with biological systems is of fundamental interest to a wide range of applications, including drug delivery, therapeutics, bioimaging, nanotoxicity and regulation.

In this thesis, we first show a unique mechanism of hexagonal boron nitride (hBN) induced cytotoxicity: a sharp hBN flake could penetrate a lipid bilayer and form a cross-membrane water channel along its exposed polar edges, leading to lysosomal membrane permeabilization (LMP), whereas a round hBN flake could not penetrate a lipid bilayer due to high energy barrier and a lack of long enough polar edges. Our *in vitro* studies confirm the water channel mechanism.

Next, we focus on how biosurfactant molecules assist liquid-phase exfoliation (LPE) of hBN. With molecular dynamics (MD) simulations and free energy calculations (FEC), we pinpoint the driving forces and identify the underlying molecular mechanisms for two processes that assist LPE: biosurfactant deposition and self-assembly on the exfoliated surface of hBN. A general guideline is provided to the design of novel surfactant molecules for more efficient LPE of 2D materials.

Finally, we investigate coacervation and encapsulation of a designed peptide, WA30. Tryptophan (W) residues drive neighboring WA30 peptides together due to hydrophobic interactions, and intermolecular hydrogen bonds (H-bonds) form between the neighboring peptides stabilize the coacervate. A rapid change in the composition of solution near the coacervate might lead to peptide encapsulation.

Overall, this thesis is aimed to provide some of the required theoretical insights towards understanding bio-nano-interactions, specifically, in cell-nanomaterial interactions, biosurfactant assisted liquid-phase exfoliation, as well as peptide coacervation and encapsulation.

Mechanics and Molecular Mechanisms in Bio-nano-systems

by

Xuliang Qian

B.Sc., University of Science and Technology of China, 2016

M.Sc., Brown University, 2018

A dissertation submitted in partial fulfillment of the

requirements for the Degree of Doctor of Philosophy

in the School of Engineering at Brown University

Providence, Rhode Island

February 2022

This dissertation by Xuliang Qian is accepted in its present form

by the School of Engineering as satisfying the

dissertation requirement for the degree of Doctor of Philosophy.

Date _____ _____

Prof. Huajian Gao, Advisor

Recommended to the Graduate Council

Date _____ _____

Prof. Kyung-Suk Kim, Reader

Date _____ _____

Prof. Jing Yu, Reader

Approved by the Graduate Council

Date _____ _____

Prof. Andrew G. Campbell

Dean of the Graduate School

Vita

Xuliang Qian was born November 4th, 1993 in Hangzhou, Zhejiang Province, P. R. China. He attended University of Science and Technology of China (USTC) in 2012 and received the B.Sc. in Theoretical and Applied Mechanics in 2016. In the fall of that year, he started his graduate study in the Solid Mechanics program at Brown University and attained his M. Sc. in School of Engineering in 2018. His research is highly interdisciplinary, spanning across cell-nanomaterial interactions, biomolecular self-assembly on the chemical interfaces and peptide coacervation.

Acknowledgements

First, I would like to thank my advisor, Prof. Huajian Gao, for his mentoring and guidance during the last five years. His pure love, passion, and vision in science and research, his patience and encouragement in mentoring, his constant and consistent kindness, support, and positiveness have led me from an undergraduate student to a true researcher. I am so proud and fortunate to be one of his students.

I would also like to thank my dissertation committee members, Prof. Kyung-Suk Kim and Prof. Jing Yu for willingly taking the time to read my thesis and provide valuable feedback. I want to thank the entire faculty of Solids Mechanics at Brown University for the wonderful education and research environment and thank all the administrative staffs at School of Engineering for providing excellent support.

During my research, I received significant help from group members, collaborators, and friends at Brown University and Nanyang Technological University, Singapore. I would like to thank Prof. Wenpeng Zhu for his help and guidance on my research. I'm sincerely grateful for Dr. Alberto Bianco, Prof. Annette von dem Bussche, Dr. Matteo Andrea Lucherelli, Prof. Jing Yu and Haopeng Li for invaluable discussions and enjoyable collaborations. Many thanks to my fellow group members and all my friends for the joyful time together.

Most importantly, I would like to express my deepest gratitude to my parents, Huijin Bian and Xianfeng Qian, who have supported me throughout my PhD journey with their unfailing love and confidence in my efforts. Accomplishment of this thesis would not be possible without their support and encouragement.

DEDICATED TO MY DEAR PARENTS,

AND ALL OF THOSE WHO LOVE AND SUPPORT ME AS ALWAYS.

Contents

List of Tables

List of Figures

Chapter 1

Introduction

1.1. Brief overview of bio-nano-interactions

Over the past decade, the interactions between nanomaterials and biological systems have become a hot topic for applications in drug delivery, therapeutics, bioimaging, nanotoxicity and regulation [1-8], due to their essential importance in the potential toxicity and health risks. Nanomaterials may interact with plasma membranes prior to cellular uptake [9-13] and with membranes of intracellular vesicles following uptake [14-17] via a toolbox of interaction mechanisms including adhesion, deformation, penetration, lipid extraction, receptor-mediated and frustrated endocytosis, uptake, and cytotoxicity [9, 11, 18-20]. To date, most of the available data for cell-nanomaterial interactions have been accumulated from studies on graphene-based materials, whilst very little is known about the biological interaction of emerging 2D materials including hexagonal boron nitride (hBN). Hence, there is a driving force to study the fundamental biophysical and molecular mechanisms in how emerging 2D materials such as hBN interact with cell membranes, as well as the pathological responses both in vitro and in vivo [4, 21-23].

Another problem in bio-nano-interactions is biosurfactant aided liquid-phase exfoliation (LPE) which is recently emerging as a biocompatible, green, clean, economical, safe, and efficient approach to fabricating two dimensional (2D) materials for biomedical

applications [24-27]. Among various methods for large-scale fabrication, liquid-phase exfoliation (LPE) can produce high yield, high quality 2D materials in aqueous phase [27-29]. Our recent study reported Sodium Cholate (SC) aided liquid-phase exfoliated round hBN (r-hBN) to be safe for human lung epithelial cells [5]. Ruiz and co-works reported that FMN dispersed graphene has very low cytotoxicity [30]. A vast amount of research efforts have been devoted to carbon-based low dimensional materials, and the molecular mechanism of biosurfactant assisted LPE of emerging 2D materials such as hBN remain largely unexplored. It is worthwhile to explore the molecular mechanism of biosurfactant interacting with graphene and other emerging 2D materials, so as to facilitate the design of novel surfactant molecules for more efficient LPE of 2D materials, and potentially, aiding the development of safe, novel, effective nanomedicines.

Delivery of nano-sized particles or capsules to biological cells is of growing interest in the scientific community. In the era of COVID-19, we are witnessing the massive use of lipid-nanoparticle (LNP) based mRNA vaccines [31]. Nano-sized particles hold great promises for applications as vaccine delivery systems with potent adjuvant activities [32]. An unprecedented growth of interests have been devoted to the development and applications of nano-scale delivery systems, with broad applications also in, e.g., the food, agriculture, drug-delivery and renewable energies [33-36]. In particular, micro/nano-encapsulation, a process that involves spontaneous self-assembly of biomolecules on the chemical or biological interfaces into enclosed "capsules" with the size of micrometers or even nanometers, has emerged as a unique and novel field of research. Several compounds have been reported to encapsulate with the formation of a membrane, mostly naturally occurred molecules, including lipids or fatty acids, amphiphilic proteins or peptides, block

copolymers and inorganic colloidal particles [37]. There is a driving force to unravel the molecular mechanism for encapsulation, to expand the study from naturally occurred molecules to the synthetic systems, and to enable *de novo* design with a focus to achieve enhanced functionality and precise control of coacervation and encapsulation [38].

1.2. Outline of the thesis

This thesis is outlined around three problems/projects. Chapter 2 described our discovery of a novel cell-nanomaterial interacting mechanism: hydrophilic channel, induced by the polar edges on hBN nanosheets, can damage lipid membranes albeit leading to lysosomal membrane permeabilization (LMP) and eventually cell apoptosis (cytotoxicity). We then investigated the self-assembly process of biomolecules, ranging from small biomolecules (Sodium Cholate and Flavin Mononucleotide) to *de novo* peptides, on the chemical interfaces: In Chapter 3 we address the problem of biosurfactant self-assembly on 2D material substrates. Chapter 4 demonstrates our recent progress in understanding the molecular mechanism of coacervation and encapsulation of a *de novo* peptide with repetitive sequence of amino acids. We close in Chapter 5 with the major scientific findings and future perspective.

Chapter 2

Boron nitride nanosheets can induce water channels across lipid bilayers leading to lysosomal permeabilization

The work described below is in collaboration with the experimental groups of Dr. Alberto Bianco, Prof. Paolo Samorì and Prof. Annette von dem Bussche. Dr. Matteo Andrea Lucherelli and Dr. Alberto Bianco prepared the hBN samples; Dr. Matteo Andrea Lucherelli, Dr. Matilde Eredia, Prof. Paolo Samorì and Dr. Alberto Bianco performed the characterization of hBN; Ms. Paula Weston and Prof. Annette von dem Bussche performed the cytotoxicity studies on the round and cornered hBN. This work is published on Advanced Materials. (DOI: https://doi.org/10.1002/adma.202103137).

2.1. Introduction

Understanding the interactions between nanomaterials and biological systems, in particular cellular membranes, is fundamental to address important challenges such as the safe design and regulation of novel engineered nanomaterials [6-8], development of drug delivery systems [1], and membrane active nanomedicines [2, 3]. Nanomaterials may interact with plasma membranes prior to cellular uptake [9-13] and with membranes of

intracellular vesicles following uptake [14-17]. The interaction mechanisms include adhesion, deformation, penetration, lipid extraction, receptor-mediated and frustrated endocytosis, uptake, and cytotoxicity [9, 11, 18-20]. In this context, pathological responses to cell interactions with 2D geometries have attracted special attention [10, 39, 40]. To date, most of the available data have been accumulated from studies on graphene-based materials. These studies have shown that material geometries such as shape and size can influence how 2D materials interact with cell membranes. For example, graphene nano- and micro-sheets with atomically sharp edges can spontaneously penetrate cell membranes, leading to lipid extraction and membrane damage [10, 12, 41-44].

In spite of the progress in this realm of research, very little is known about the biological interaction of many emerging 2D materials, in particular hexagonal boron nitride (hBN), which has gained a great interest as substrates for electronic and optoelectronic devices [45-47], and as components in engineered composites due to its excellent chemical and thermal stability [48-50]. In addition, water dispersible hBN nanoplatelets were explored as protein carriers. Bovine serum albumin cross-linked to hBN surface was used as immunostimulant adjuvant following the immunization of mice, leading to higher antibody titers compared to the treatment with the protein alone [51]. Alternatively, hBN exfoliated by a poly(propylene) glycol chain terminated by two adenine molecules allowed the encapsulation of hydrophobic anticancer drugs and their subsequent controlled release triggered either by temperature increase or pH change [52]. In other recent studies, hBN sheets doped with zirconium or grafted onto the surface of cellulose fibers were exploited as new antibacterial complexes [53, 54]. Hitherto, only a few in vitro and in vivo toxicity studies have been performed using hBN, often with conflicting results. For example, sheet-

like BN materials were reported to produce multiple adverse effects on human hepatoma HepG2 cells, such as decreasing cell viability, enhancing intracellular ROS production, causing mitochondrial depolarization, and inducing damage to membrane integrity [55]. By contrast, another study showed hBN nanosheets functionalized with hydroxyl groups were non-cytotoxic to insect hemocytes, L929 mouse cells, and human erythrocytes [56]. In silico studies have also been conducted to investigate the interaction between BN-based materials and cell membranes. For instance, hBN nanotubes were observed to be spontaneously attracted by lipid bilayers and form stable lipid insertion [57], while hBN nanosheets were found only interacting with the polar head groups of lipid molecules, but not passively crossing the lipid bilayer [21]. In addition, lipid extraction of hBN nanosheets was noticed to be temperature-dependent.[58] At this point, a fundamental biophysical understanding of how hBN interacts with cell membranes remains largely unexplored [4, 21-23].

In this context, we have studied how hBN, obtained by liquid-phase exfoliation, interacts with cell membranes by combining molecular dynamics simulations and in vitro imaging. First, we performed molecular dynamics (MD) simulations to identify potential atomic mechanisms of hBN interacting with a lipid bilayer. The simulations show that a sharp hBN wedge with exposed polar edges can induce the formation of water channels along these edges, and such water channels in turn facilitate cell penetration by hBN. In comparison, a round hBN sheet with no or little exposed polar edges does not induce the formation of water channels, while encountering a very high energy barrier against membrane penetration. This discovery led to hypothesize that water channels play essential roles in how hBN interacts with cell membrane. One of the most prominent consequences

is that the hydrophilic water channels along hBN could facilitate cross-membrane transport, leading to lysosomal membrane permeabilization (LMP), which has recently been identified as a possible mechanism of cytotoxicity involving release of cathepsin B and generation of radical oxygen species followed by cell apoptosis. We then focused on validating this hypothesis by preparing two types of hBN nanosheets, one with a rhomboidal, cornered morphology and the other with a round morphology, and proving evidence through in vitro imaging methods that the former displayed cytotoxicity through LMP, while the latter provoked no response.

2.2. Atomistic simulations

2.2.1. Simulation model and methodology

2.2.1.1. All-atom Molecular Dynamics (MD) simulations

All-atom MD simulations based on GROMACS package (version 2018.2) were performed to investigate the interactions between hBN and lipid membrane [59, 60]. An empirical force field was adopted for hBN nanosheets [61-63]. Since the major glycerophospholipids assembled in cell membranes, lysosomes and endosomes are phosphatidylcholine (PtdCho; PC) [64], 1-palmitoyl-2-oleoyl-sn-glycero-3-phosphocholine (POPC) was chosen in our all-atom simulations to construct a pure lipid bilayer with dimensions of 12.1×12.0 nm (with 494 POPC lipids). POPC lipids were modelled by Berger's lipid force field [65], which is a widely used all-atom lipid model for membrane-protein simulations [12, 66-69]. For high computational efficiency, water molecules were represented by a simple point-charge SPC/E model with polarization

correction [70]. The geometric combining rule in Lennard-Jones (LJ) potential was employed for non–bonded interactions of hBN with POPC lipids and water. The smooth particle-mesh Ewald (SPME) method was used to calculate the long-rang electrostatic interactions with a cutoff of 1.2 nm [71]. The simulations were performed with NPT ensembles and periodical boundary conditions in all directions, under constant pressure of P = 1 atm and constant temperature of T = 300 K, which is higher than the phase transition temperature (270 K) of POPC lipids [72, 73]. The simulation box had an initial height of 19.1 nm, which was large enough to prevent the membrane and hBN from interacting with their periodic images. The time step was set at 2 fs. After a 100 ns initial equilibration of solvated lipid systems, r-hBN with radius of 3.2 nm and c-hBN with edge length of 5.4 nm were introduced in the box by replacing some overlapping water molecules. r-hBN was placed at a starting distance of 4 nm above and orthogonal to the lipid bilayer. c-hBN was placed 2 nm above the lipid surface with one of its edge orthogonal to the lipid bilayer. The rationale behind such configuration is that orthogonal orientation of nanosheets exerts weakest confinement on the bilayer, thereby maximizing the entropy and minimizing the free energy of the system [10]. After 10 ns of re-equilibration, the hBN flakes were pulled under constant forces for 40 ns across the bilayer (Figure 2.1). The pulling forces were applied between the centers of mass (COM) of the hBN flakes and the bilayer. The value of the pulling force was selected based on a previous study to accelerate the piercing process within computational capacity [21]. Four atoms on each corner of a rhomboidal hBN and three atoms on a circular hBN were set free to move only in the direction orthogonal to the bilayer (Figure 2.2). The simulations showed that for a relatively small pulling force, 200 kJ/mol/nm, c-hBN can fully penetrate the membrane, whereas r-hBN is

incapable. We increased the pulling force stepwise and found that r-hBN still cannot fully penetrate the membrane under 400 kJ/mol/nm pulling force. Only when the pulling force reached 800 kJ/mol/nm was r-hBN able to fully penetrate the membrane, indicating the difficulty for r-hBN to disrupt the membrane. VMD was used to visualize the simulation results. Analyses were carried out using GROMACS and VMD [74].

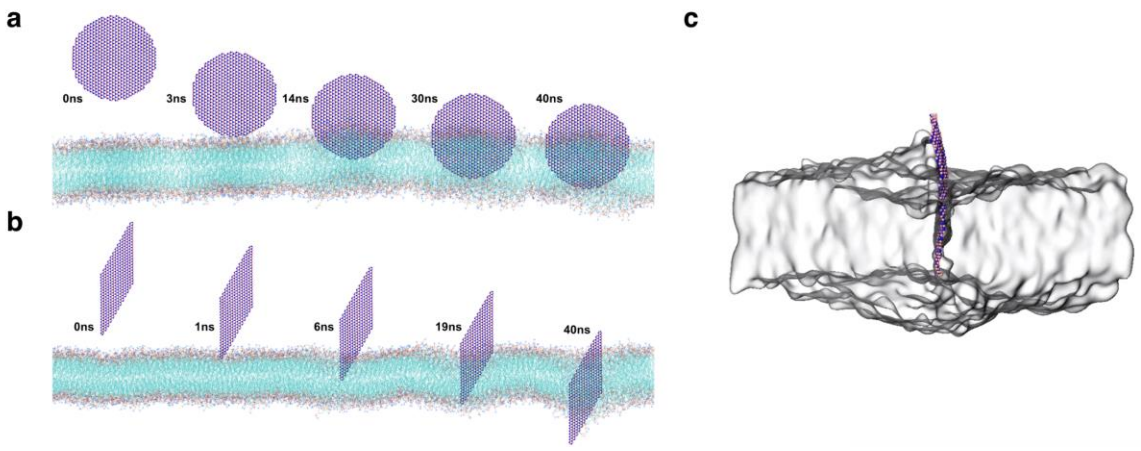

Figure 2. 1. Time evolution of r-hBN (a) and c-hBN (b) piercing lipid bilayer under a pulling force of 200 kJ/mol/nm, and (c) a snapshot showing lipid extraction on the concave surface of r-hBN.

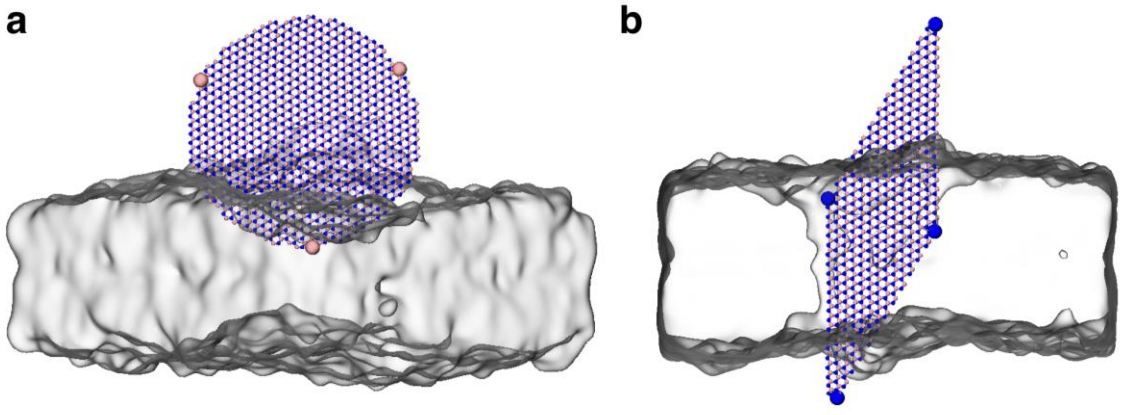

Figure 2. 2. Position restrained atoms on (a) r-hBN and (b) c-hBN flakes.

2.2.1.2. Umbrella Sampling

The pulling simulations helped us calculate the free energy evolution with the umbrella sampling (US) method. Trajectories from the pulling simulations were collected and stratified into an array of windows. One configuration is extracted from each window. For the rhomboidal hBN system, 56 configurations were extracted, with the interval distance taken to be 0.15 nm, whereas for the circular hBN system, 50 configurations were extracted with an interval distance of 0.10 nm (Figure 2.3).

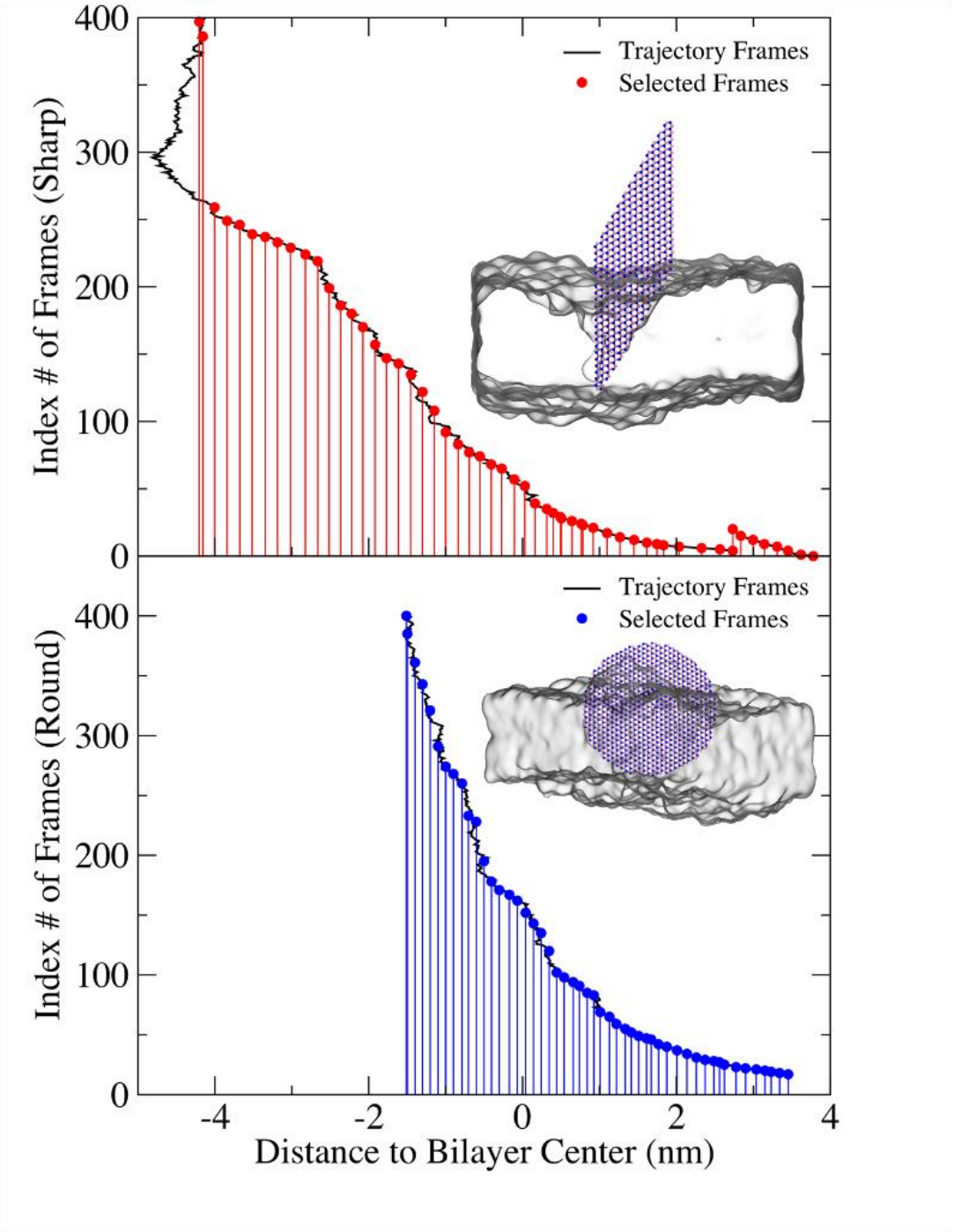

Figure 2. 3. Stratification of reaction coordinates for umbrella sampling.

An open-source python script was modified to automate the stratification process (http://www.mdtutorials.com/gmx/umbrella/Files/setup-umbrella-script.tar.gz).

Restraining by a harmonic potential, each configuration was relaxed for 20 ns independently within its defined US window. After all US simulations were completed, the weighted histogram analysis method (WHAM) was used to calculate the potential of mean force (PMF) [75, 76]. Errors were obtained from the bootstrap method (Bayesian Histograms) using 200 bootstraps. The thermal energy $k_B T$ was used as the unit of energy in the simulations with *T* corresponding to 300 K. At equilibrium, the probability of a system in a state of energy *E* is proportional to $e^{-\frac{E}{k_B T}}$. In this way, the system stability could be explicitly compared at different equilibrium states.

The interaction energies between hBN and lipid bilayer were obtained using GROMACS rerun energy evaluation (Figure 2.4). All energies increase monotonically with respect to pulling, while r-hBN energy profile exhibits a larger slope. This suggests that r-hBN encounters larger resistance than c-hBN when piercing the lipid bilayer.

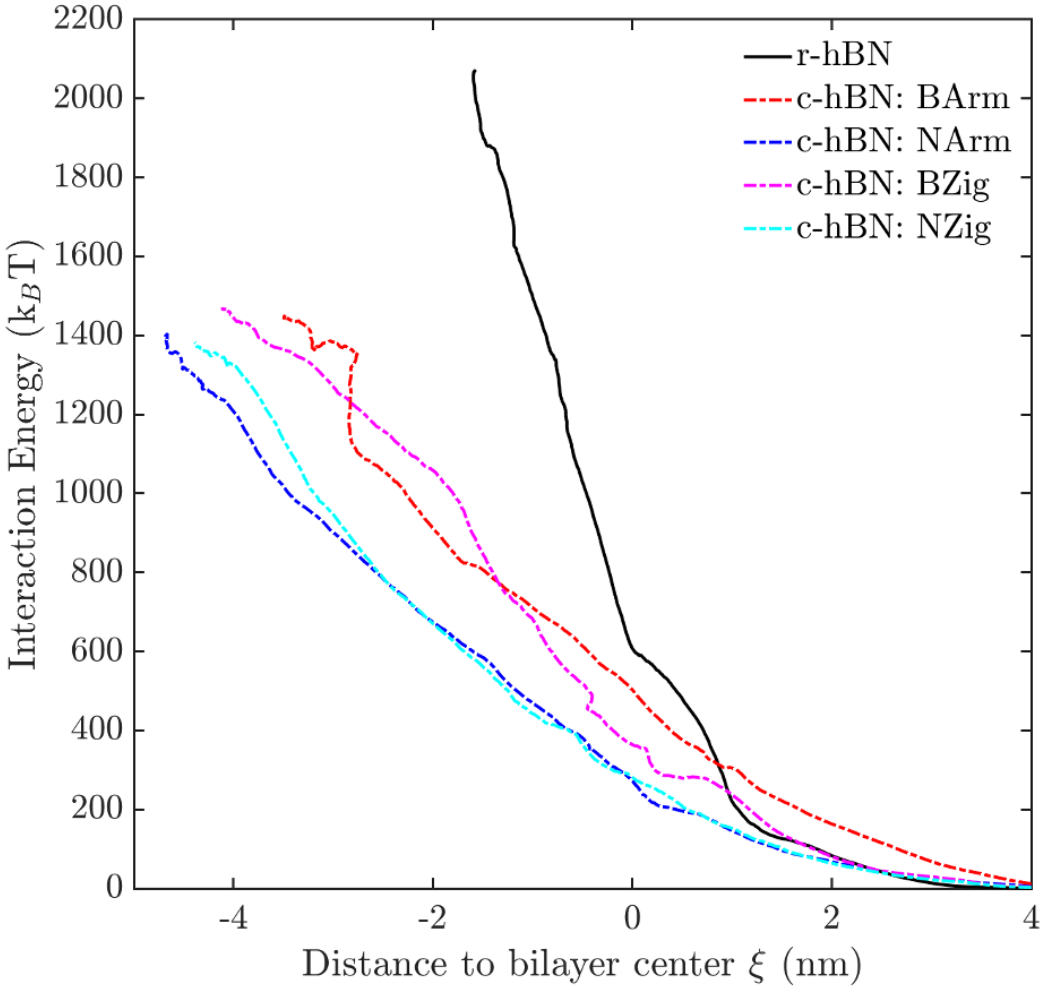

Figure 2. 4. Interaction energies of round/cornered hBN flakes penetrating a lipid bilayer.

2.2.1.3.Free Energy Perturbation

Free Energy Perturbation (FEP) method was used to calculate the binding affinities associated with the hydrophilic channel formation. Configurations of FEP simulations are extracted from MD simulations (Figure 2.5).

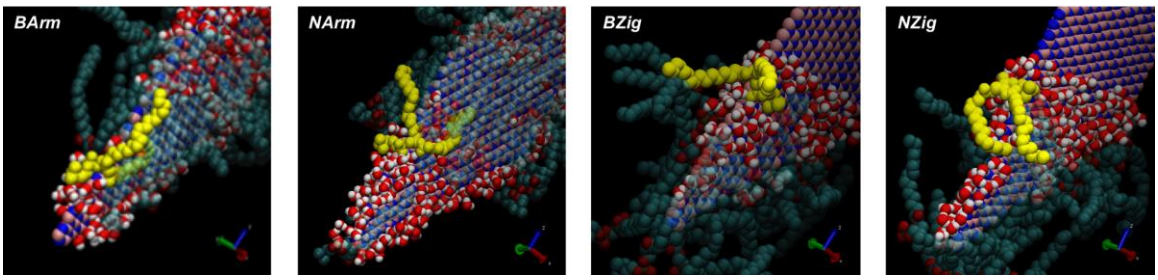

Figure 2. 5. The configurations for FEP simulations are extracted from MD simulations. The selected POPC molecules located at the competition spots with water molecules. In both BArm and NArm cases, the selected lipid molecules block the hydrophilic channel, whereas in BZig or NZig cases, the selected lipid molecules cannot block the channel.

To compute accurate free energy differences by FEP, multiple "alchemical" rather than physical intermediate states were used to minimize the perturbation to the system [77]. The procedure for the computing binding affinities is illustrated in Figure 2.6. $\Delta G_{Lipid\text{-}hBN}$ is the binding affinity of a lipid to the site of interest on hBN. $\Delta G_{Water\text{-}hBN}$ is the binding affinity of water molecules to the corresponding site on hBN. To calculate ΔG_1 and ΔG_2, one lipid on hBN and another lipid in vacuum are annihilated, respectively. In practice, multiple intermediate stages (denoted by λ) are inserted, enabling a gradual annihilation; λ ranges from 0 to 1, with $\lambda = 0$ corresponding to the initial state (lipid not annihilated from the system) and $\lambda = 1$ to the final state (lipid annihilated from the system). Similar procedure could be found in a previous study [78]. After some trial-and-error, we chose 41 intermediate states to balance the accuracy and computational cost. The Multistate Bennett Acceptance Ratio (MBAR) method was used to calculate free energy difference associated with the annihilation process and to estimate the error [79]. The same protocols were applied to calculate ΔG_3, ΔG_4 and $\Delta G_{Water\text{-}hBN}$.

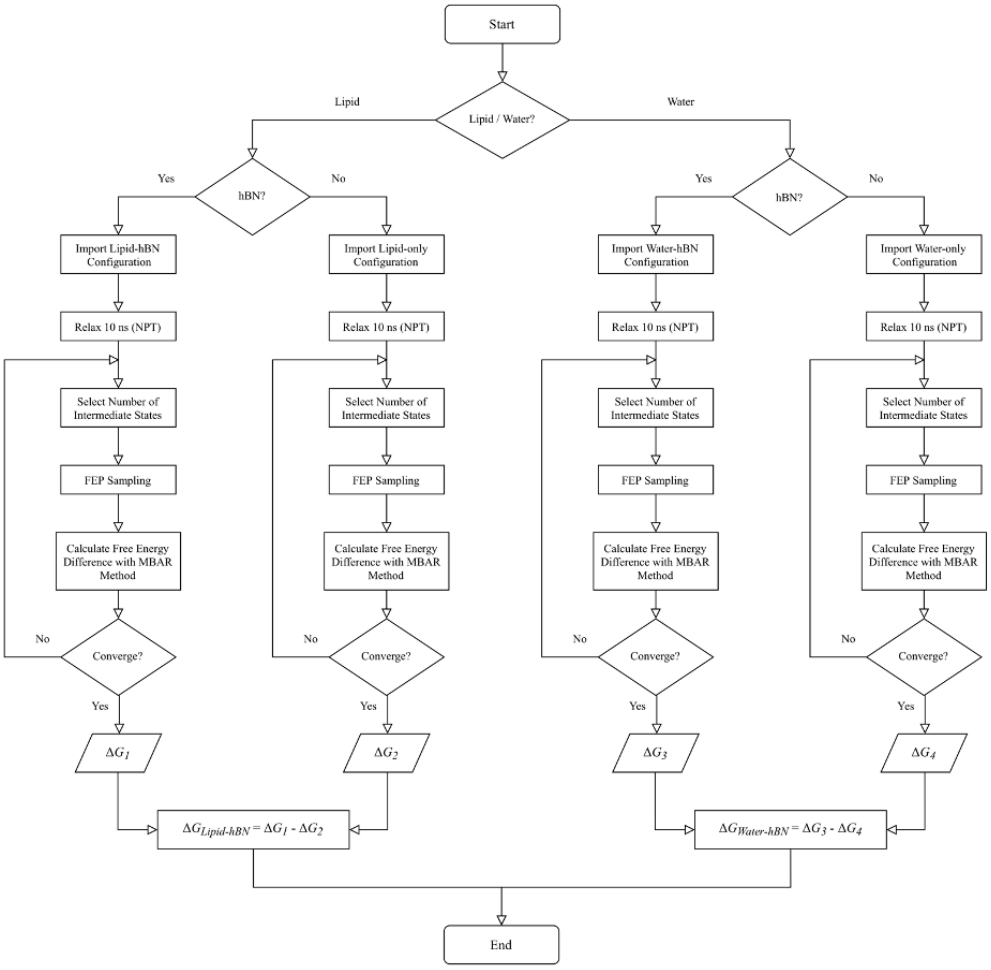

Figure 2. 6. Flow chart for computing binding free energies between water molecules, lipid molecules and hBN.

2.2.2. Energetics of round and sharp hBN piercing a lipid membrane.

We initially conducted all-atom MD simulations to unravel the mechanism on the atomic scale of interaction between hBN and a model lipid bilayer. Two different shapes of hBN flakes were considered: a round hBN (r-hBN) with radius of 3.2 nm and a cornered hBN (c-hBN) with edge length of 5.4 nm. Details of simulation steps can be found in section 2.2.1.1. To determine the free energy evolution associated with hBN piercing, we conducted umbrella sampling (US) simulations.

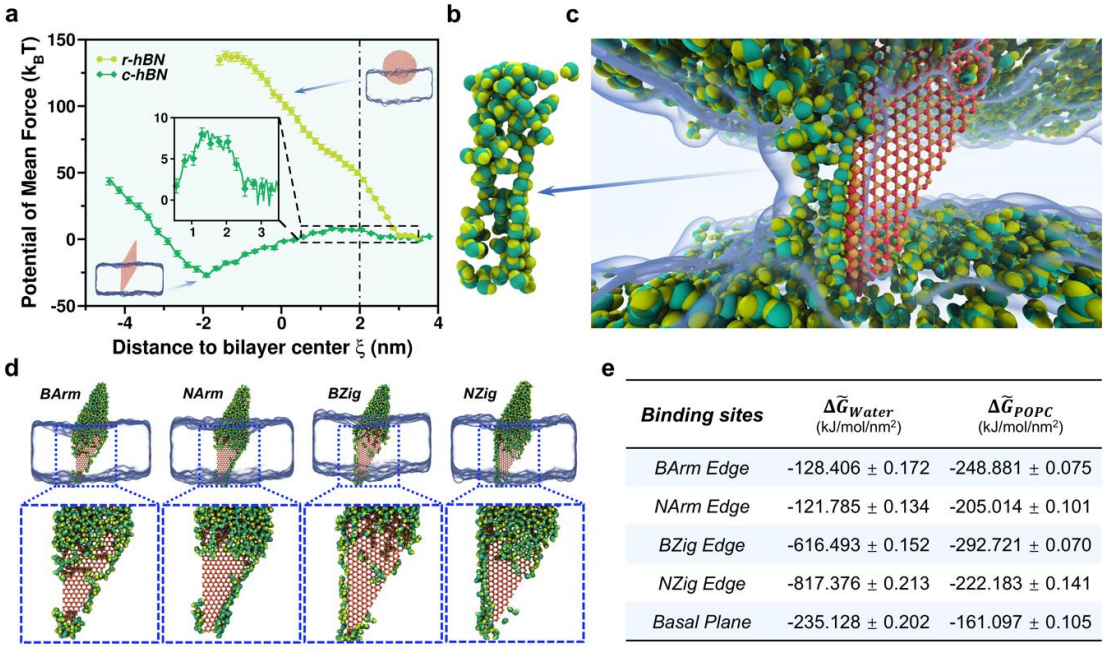

Binding sites	$\Delta\widetilde{G}_{Water}$ (kJ/mol/nm²)	$\Delta\widetilde{G}_{POPC}$ (kJ/mol/nm²)
BArm Edge	-128.406 ± 0.172	-248.881 ± 0.075
NArm Edge	-121.785 ± 0.134	-205.014 ± 0.101
BZig Edge	-616.493 ± 0.152	-292.721 ± 0.070
NZig Edge	-817.376 ± 0.213	-222.183 ± 0.141
Basal Plane	-235.128 ± 0.202	-161.097 ± 0.105

Figure 2. 7. a, PMF profile of hBN piercing the membrane as a function of the distance between the lower tip of hBN and COM of bilayer. Inset: zoom-in view of the PMF profile for c-hBN within the area selected by the dash-line box; representative configurations of r-hBN (upper right) and c-hBN (lower left) piercing lipid bilayer under a pulling force of 200 kJ/mol/nm. **b**,**c**, Simulation snapshots of the hydrophilic channel (**b**) formed along an hBN Zigzag edge (in this case, Nitrogen-dominated Zigzag, or NZig). Fast transportation of water molecules across the lipid bilayer is expected in such channel. Colors for the atoms: orange, boron; red, nitrogen; peacock blue, oxygen; and chartreuse yellow, hydrogen. The water channel is outlined by a transparent blue-grey contour surface in (**c**), remote water and lipid molecules are hidden for clarity. **d**, Atomic configurations, and cross-membrane

water distribution of four c-hBN systems after piercing (*"BArm"* stands for an Armchair edge, which is neighbored by a Boron-dominated Zigzag edge; *"NArm"* stands for an Armchair edge, which is neighbored by a Nitrogen-dominated Zigzag edge; *"BZig"* stands for a Boron-dominated Zigzag edge; *"NZig"* stands for a Nitrogen-dominated Zigzag edge). Insets: zoom-in snapshots of water molecules (marked peacock and yellow) near hBN in each system, colors for the atoms are the same as (**b**) and (**c**), lipid bilayers are represented with transparent blue-grey contour surfaces, remote water molecules are hidden for clarity. **e**, Table of binding free energies per contact area between a water molecule or a 1-palmitoyl-2-oleoyl-sn-glycero-3-phosphocholine molecule and hBN at different binding sites.

Figure 2.7a shows the calculated potential of mean force (PMF) plot, with reaction coordinate selected to be the distance between the bottommost atom of the hBN flake and the center-of-mass (COM) of the membrane. A drastic difference was immediately observed in the behavior of PMF for round and cornered hBN upon piercing into the bilayer. Namely, the PMF for r-hBN piercing keeps increasing and exhibits an energy barrier as high as 135 $k_B T$ as it pierces across the hydrophobic core of the lipid bilayer. By contrast, the PMF for c-hBN exhibits an energy barrier only around 8 $k_B T$ as it pierces into the bilayer, before heading down to an energy minimum around -27 $k_B T$. Further simulations, in which the hBN flakes are pulled orthogonally across a lipid bilayer with constant forces (Figure 2.7a insets), confirm that r-hBN encounters stronger resistance than c-hBN during piercing, supporting the observations from PMF. Movies S1–S4 in our published work show the dynamic processes for such piercing [5].

The PMF for r-hBN is consistent with our intuition that the total free energy should increase monotonically with increasing area of contact between hBN and lipid tail region as well as decreasing interactions between hBN and water, but the behavior for c-hBN is unexpected and suggests an unknown mechanism might be in operation. To shed light on

the underlying mechanism, we investigated the molecular structure at the PMF energy minimum of c-hBN. Interestingly, we discovered a type of cross-membrane hydrophilic channel constituted of water molecules along the pierced zigzag edge of c-hBN (Figure 2.7b,c). A detailed examination of the evolution of this structure revealed that as the lower tip of c-hBN flake approached the bilayer, it brought along water molecules adhering to the hBN surface. During piercing, most water molecules remained at the hydrophilic lipid head region, while those in the vicinity of the zigzag edge managed to enter the hydrophobic lipid tail region by aggregating around the pierced zigzag edge, eventually coalescing into a water channel across the bilayer.

The radius of this water channel was measured to be 1 nm for the single layered hBN. The measurement was done by counting the number of water molecules within specified radii around a zigzag edge within the membrane core (hydrophobic lipid tail region), as illustrated in the Figure 2.8a. A plot of the number of water molecules versus a specified radius can be found in Figure 2.8b. The effective radius r_e of the channel is defined as the turning point beyond which the number of water molecules starts to saturate as the radius increases further. By this definition, the effective radius of an NZig hydrophilic channel of monolayer hBN was indeed 1 nm for the single layered hBN case.

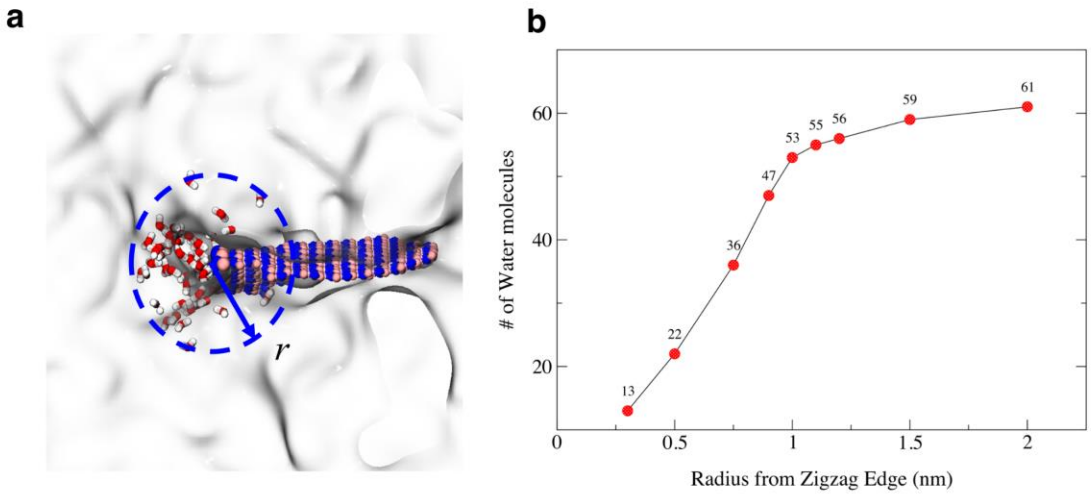

Figure 2. 8. a, Illustration of counting the number of water molecules within certain radius from the Zigzag edge; **b**, Number of water molecules versus specified radius plot shows saturation as the radius increases beyond 1 nm, which is the effective radius of the channel.

2.2.3. Discovery of a cross-membrane water channel induced by the exposed, polar zigzag edge on sharp hBN

To elucidate the mechanism of water channel formation, MD simulations were carried out with one edge of c-hBN positioned orthogonal to the lipid bilayer. The edges of interest included two types of zigzag edges, namely, boron-dominated zigzag (BZig) and nitrogen-dominated zigzag (NZig), and two types of armchair edges, namely, BArm (adjacent to a BZig edge) and NArm (adjacent to an NZig edge), within the bilayer. Note that the hBN armchair edges and basal planes in our simulations are neutral charged and less polarized. The hBN zigzag edges, however, are highly polarized as partial charges on the outermost array of atoms establish electric dipoles with those on the covalent bonded second array of atoms from the edge. The edge normal components of the electric dipole moments are nonzero in the case of zigzag edges, leading to strong polarity. Simulation

snapshots confirm the formation of water channel in all four cases (Figure 2.7d). While a few water molecules were distributed on the basal plane of hBN within the lipid bilayer, no water channels were observed. Closer examinations confirm that the water channel is always associated with a pierced zigzag edge (Figure 2.7d, insets). Detailed MD trajectories leading to the assembly of water channel, and a smaller scale simulation reveals how a water channel was assembled from scratch can be seen in Movies S5–S9 in the published version [5]. In all cases, the water channel is formed spontaneously and remains stable once formed, at least within the simulation time scale (10^1–10^2 ns).

2.2.4. Driving force for the formation of water channel

To pinpoint the driving force behind the water channel formation, the binding free energies between a molecule of interest (lipid or water molecule) on hBN at a site of interest (four types of edges and basal plane) were evaluated using free energy perturbation (FEP) method. The calculations were based on simplified models consisting of a lipid or water molecule adsorbed to one of the following sites: a BArm edge, an NArm edge, a BZig edge, an NZig edge, or a basal plane. The normalized binding affinities of lipid or water molecules to different sites on c-hBN are summarized in the table of Figure 2.7e. These results show that:

(1) Competition between lipid and water molecule on hBN is the driving force for water channel formation,

(2) Armchair edges favor the adsorption of lipid molecules, whereas both zigzag edges and basal plane favor adsorption of water molecules,

(3) Water molecules exhibit stronger binding affinity to zigzag edges than to the basal plane,

(4) Water molecules aggregating around a zigzag edge of c-hBN reduces the total free energy throughout the piercing/assembly process—the longer the channel, the lower the free energy.

These findings provide clear explanations of why the water channel form only along zigzag edges, how their formation facilitates membrane penetration of hBN as well as the PMF behaviors in Figure 2.7a. r-hBN lacking polar edges cannot induce the formation of water channel and, as a result, the total free energy for r-hBN piercing keeps increasing. c-hBN with polar zigzag edges, on the other hand, spontaneously induces water channel formation, leading to the reduction of total free energy and associated energy barrier for membrane piercing.

The water channels discussed above could play essential roles in cell-hBN interaction by facilitating cross-membrane transport. In the following sections, we proved with experiments that the c-hBN induced water channels and resulting cross-membrane transport can induce LMP leading to cathepsin B release and cell death.

2.3. Experimental studies

2.3.1. Preparation and characterization of cornered and round hBN

To prove the water channel hypothesis, two types of hBN particles were designed and synthesized: one with a cornered morphology and the other with a round morphology, consistent with MD simulation. Through a combination of exfoliation and size selection techniques, we prepared c-hBN particles with a graphene-like shape and sharp asperities and r-hBN particles with a curved shape and round edges (Figure 2.9a–d). Exfoliation of hBN in water was achieved using sodium cholate (SC), an efficient dispersant for a wide range of 2D materials [80, 81]. As an exfoliation molecule, SC can effectively disperse hBN flakes from bulk material and stabilize them against reaggregation. The dispersions were stable in water up to a concentration of 1 mg mL^{-1} for more than 24 h.

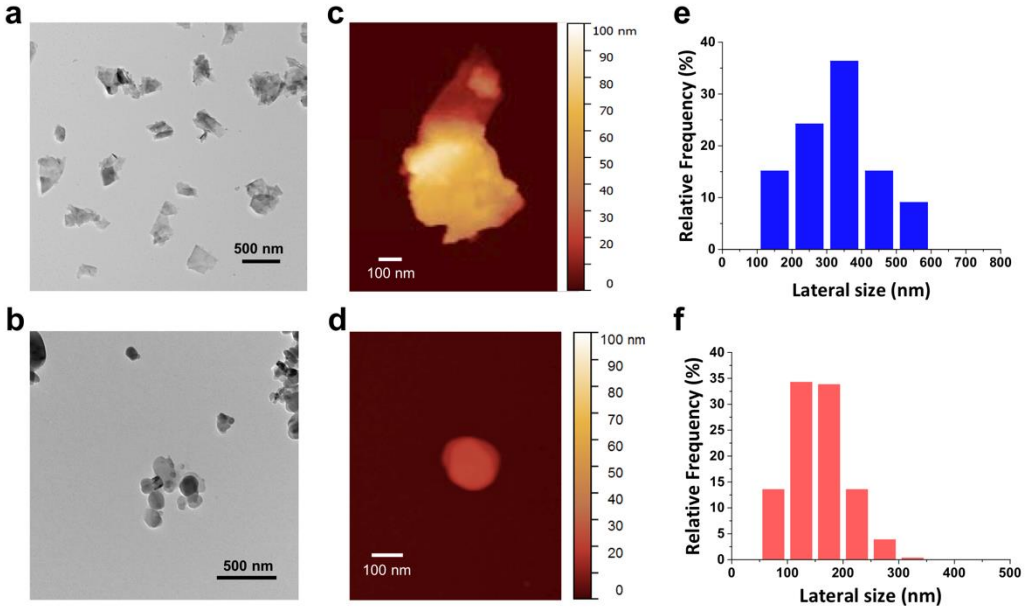

Figure 2. 9. a,**b**, TEM images of c-hBN (**a**) and r-hBN (**b**). **c**,**d**, AFM images of c-hBN (**c**) and r-hBN (**d**), **e**,**f**, Lateral size distribution of c-hBN (**e**) and r-hBN (**f**) calculated from TEM images.

The characterization of the two hBN particles was performed by using various complementary techniques. Transmission electron microscopy (TEM) images indicated that c-hBN is composed of small sheets with an averaged lateral dimension centered at 342 nm (Figure 2.9a,c,e) and with a thickness of 4.69 ± 0.05 nm corresponding to about six layers (Figure 2.10a,b). The shape of the edges and the thickness of the sheets make the morphology of this material very similar to that of few-layer graphene. A statistical analysis comprising hundreds of flakes performed by means of TEM and AFM imaging made it possible to identify the presence of at least one acute angle in the circumference of each flake. Electronic diffraction evidenced the typical hexagonal crystallinity of graphene-like materials (Figure 2.11c), as expected for hBN sheets [82]. These data are in agreement with previous studies on 2D materials and confirm the few-layer nature of hBN dispersions [83]. The r-hBN has instead different shape and sizes (Figure 2.9b,d). The lateral dimension of the round flakes was smaller (average centered at 156 nm) and characterized also by narrower distribution (Figure 2.9f). From HR-TEM images, it was possible to better understand the morphology of this material (Figure 2.12). Most of the particles appear round from above, while from the side, the form is rather ovoid with decreasing thickness in correspondence of the edges, with sharp round periphery and no evidence of clear layers (Figure 2.12a). The morphology of the material resembles to the geometric form of an ellipsoid, with reduced thickness and very thin edges, closed to 2D sheets. The electronic diffraction measurements confirmed a perfect hexagonal crystallinity of these particles, as

in the case of c-hBN (Figure 2.12b). These observations led us to conclude that the shape of this material corresponds to an ovoid compact structure, with flat and hexagonal crystalline edges, and a thickness between 6 and 35 nm (Figure 2.13c,d). Additional features of these two types of hBN have been obtained using scanning electron microscopy (SEM) and X-ray diffraction (XRD). While SEM confirmed the presence of cornered and round nano-objects (Figure 2.14), XRD showed the typical reflection peak located around 2θ ~26.7° (Figure 2.15), according to the phase identification using Crystallography Open Database [80, 84].

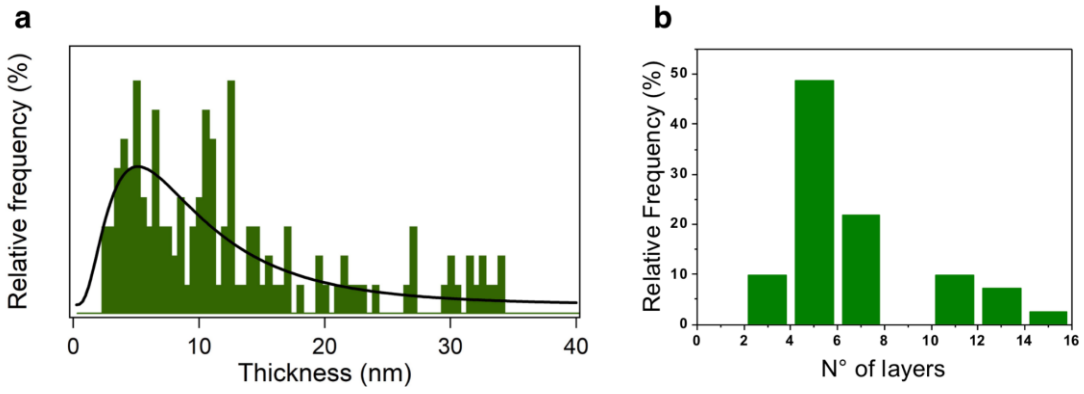

Figure 2. 10. a, Distribution of the thickness of c-hBN sheets from AFM analysis; **b**, Distribution of the number of layers of c-hBN from the analysis of HR-TEM images.

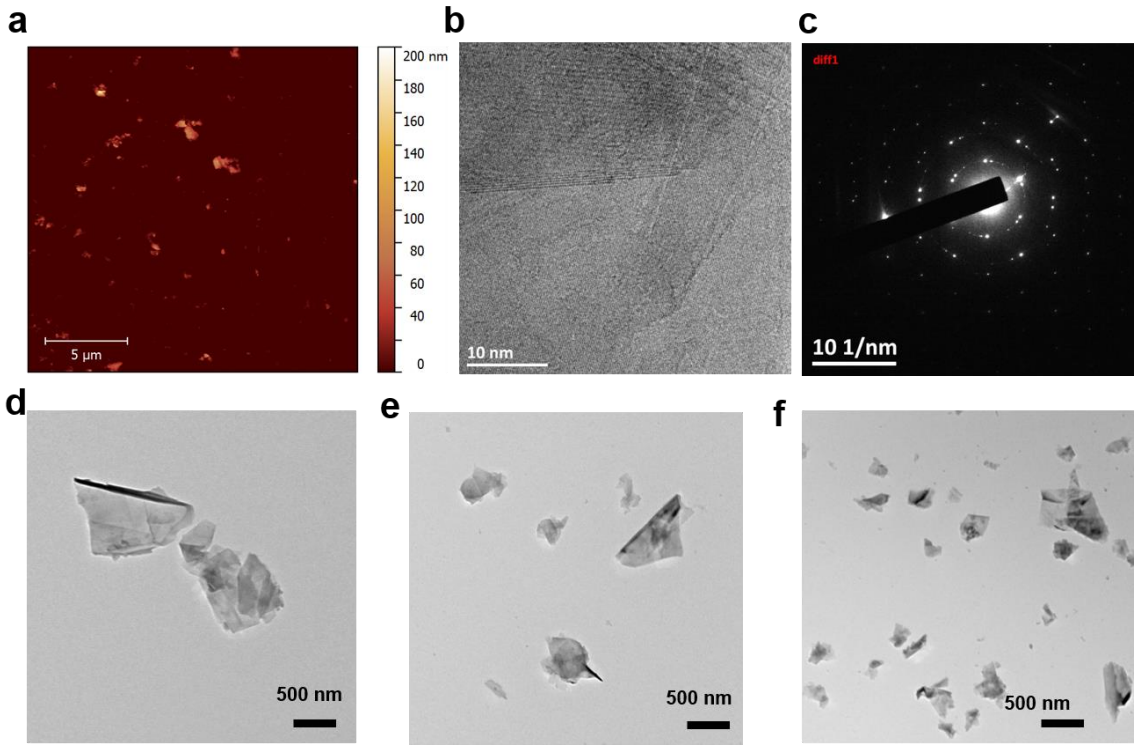

Figure 2. 11. a, AFM image of c-hBN; **b**, HR-TEM image of c-hBN; **c**, Electronic diffraction analysis of c-hBN; **d-f**, Additional TEM images of c-hBN.

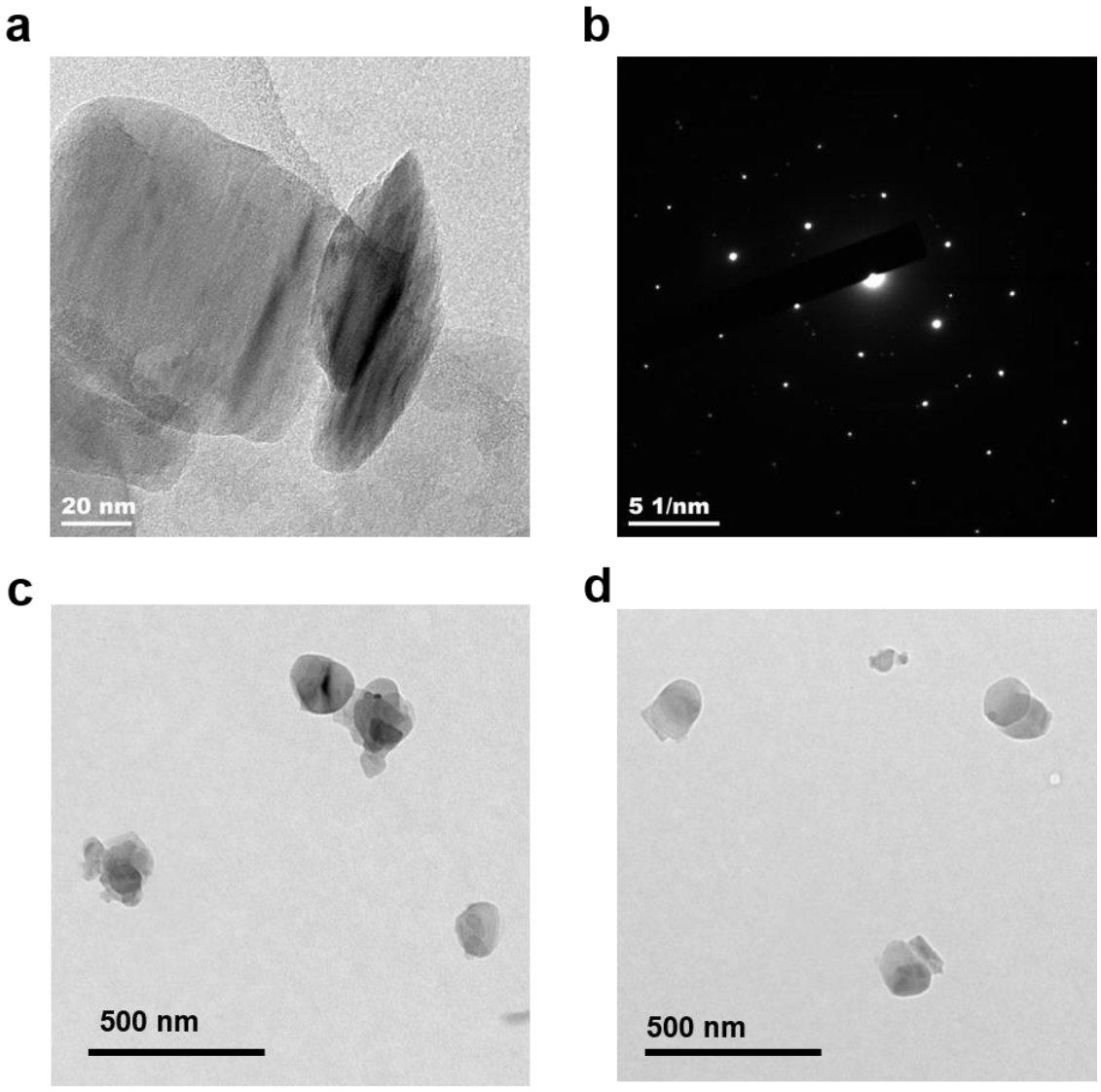

Figure 2. 12. a, Lateral side of a r-hBN particle observed by HR-TEM; **b**, Electronic diffraction of r-hBN particles; **c-d**, Additional TEM images of r-hBN.

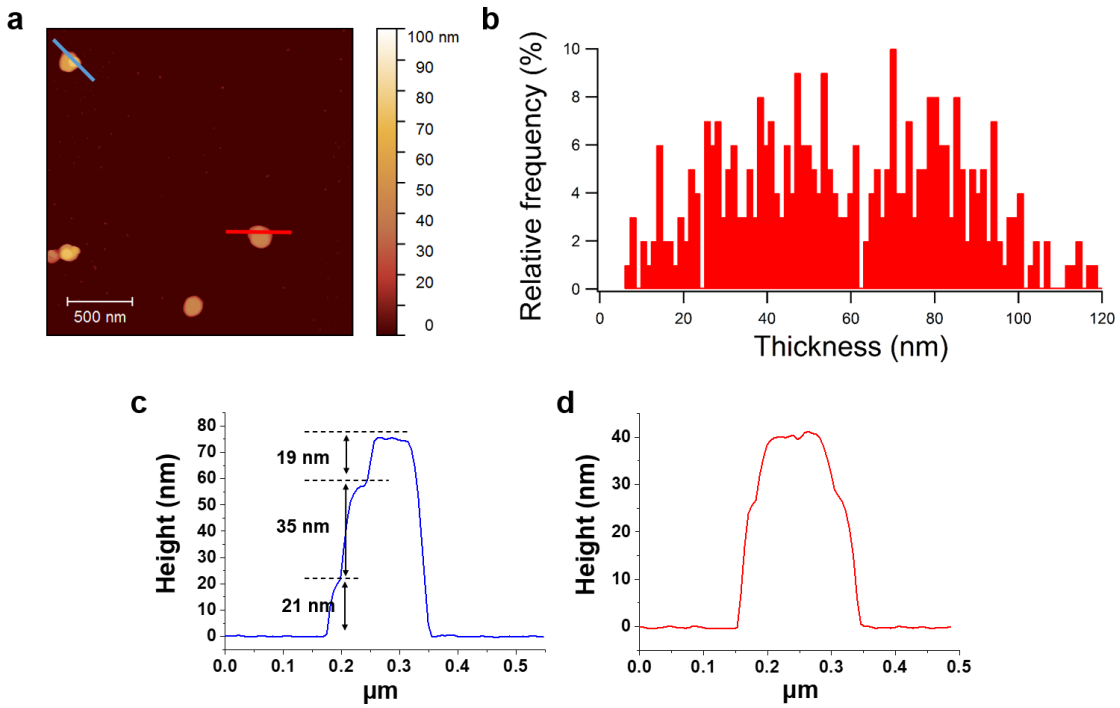

Figure 2. 13. a, AFM image of r-hBN; **b**, Thickness distribution of r-hBN; **c-d**, AFM topographical profile of r-hBN, the blue and red curves correspond to the particles in Figure 2.12.

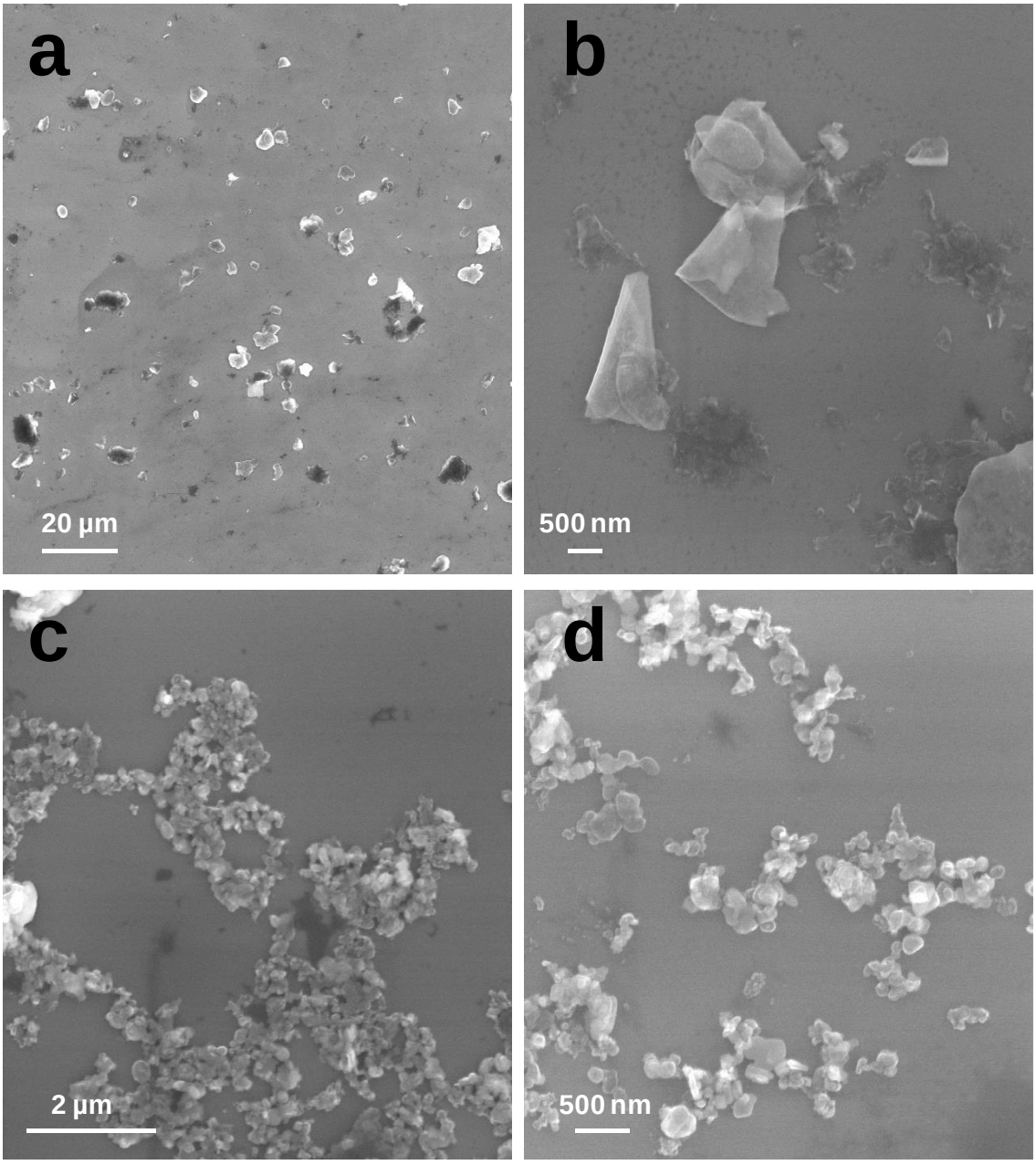

Figure 2. 14. a-b, SEM images of c-hBN; **c-d**, SEM images of r-hBN.

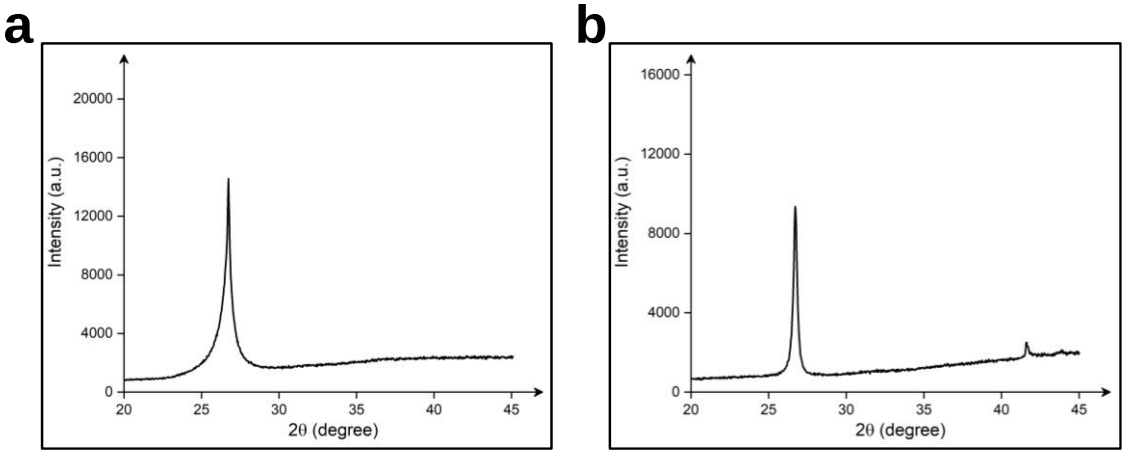

Figure 2. 15. a) XRD image of c-hBN; b) XRD image of r-hBN. The reflection peaks at 26.7° correspond to hkl 002, a distance of 3.330 Å. The peak at 41.6° in panel b corresponds to hkl 100, a distance of 2.168 Å (according to the phase identification in Crystallography Open Database) [80, 84].

2.3.2. Cytotoxicity of hBN to human lung epithelial cells

To verify our hypothesis that only c-hBN would lead to LMP, a series of cellular experiments with bioimaging modalities were conducted. Similar to our previous study [69], we used lung epithelial cells (H460) to determine possible cytotoxic effects caused by hBN. H460 cells are known to internalize nanoparticles by active cellular uptake via endocytosis [85]. Using TEM, we demonstrated that r-hBN mainly localized in lysosomes of the exposed H460 cells (Figure 2.16a), whereas c-hBN is also localized in the cytoplasm (Figure 2.16b), suggesting c-hBN can pierce across the lysosomal membrane. LMP was assessed using a fluorescence assay for one of the lysosomal proteases, cathepsin B, which is activated after releasing into cytoplasm [86]. H460 cells were incubated with different concentrations of c-hBN and r-hBN. Confocal fluorescence imaging showed that cells treated with c-hBN exhibit high level of cathepsin B release into the cytoplasm, suggesting lysosomal permeabilization (Figure 2.16e). Unexposed cells or cells exposed to r-hBN did not reveal significant cathepsin B release into the cytoplasm, revealing no significant lysosomal permeabilization (Figure 2.16c,d). The release of cathepsin B triggered a proteolytic cascade resulting in the activation of caspases, leading to cell death by apoptosis [87]. To investigate further if lysosomal permeabilization results indeed in apoptosis, the generation of superoxide anions in lung epithelial cells was determined. After exposure of cells to different concentration of c-hBN or r-hBN, fluorescence imaging was used to quantify the superoxide anion positive cells. High content imaging revealed that the treatment of c-hBN resulted in a significant higher percent of superoxide anion positive cells in comparison to untreated or r-hBN exposed cells, in a concentration dependent manner (Figure 2.16f–i).

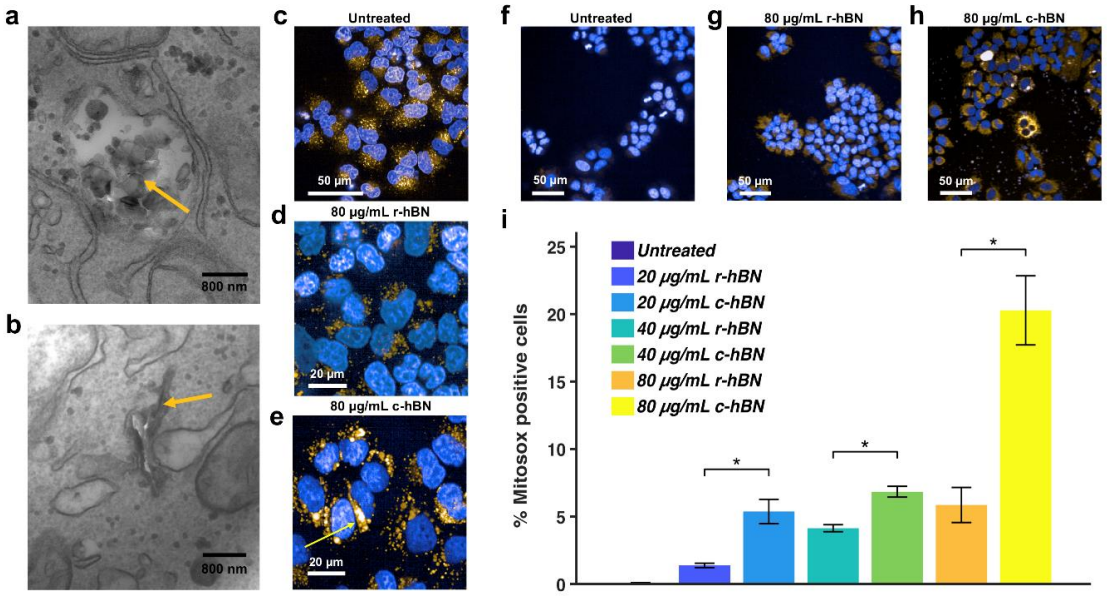

Figure 2. 16. **a**,**b**, Transmission electron micrographs of lung epithelial cells exposed to r-hBN and c-HBN. Round hBN is mainly localized within the lysosomes (**a**), whereas sharp cornered hBN (**b**) is also localized within the cytoplasm (as indicated by the yellow arrows). **c**,**d**,**e**, Lysosomal membrane permeabilization was assessed using a fluorescence assay for a lysosomal protease, cathepsin B, which retains activity following release into the cytoplasm. Confocal fluorescence imaging revealed that unexposed cells (**c**) or cells exposed to 80 µg mL^{-1} of r-hBN (**d**) do not lead to a significant release of cathepsin B as demonstrated by punctate red fluorescent cytoplasmic vesicles. Exposure to 80 µg mL^{-1} of c-hBN (**e**) induced less intense, focal, diffuse fluorescence reflecting release of cathepsin B into the cytoplasm (yellow arrow). **f**,**g**,**h**,**i**, Quantification and imaging of superoxide anion positive cells after exposure of H460 lung epithelial cells to sharp and round hBN**.** Exposure of H460 cells to 80 µg mL^{-1} of r-hBN (**g**) and 80 µg mL^{-1} of c-hBN (**h**) revealed that c-hBN generated a significant increase of superoxide anion positive cells (yellow) in comparison to the untreated control (**f**) or r-hBN (**g**). Hoechst staining (blue) was used to visualize the nucleus; (**i**) Percentage of Mitosox positive cells showing dose-dependent superoxide anion production by r-hBN and c-hBN (*$p<0.05$).

To further investigate if cell viability was affected, the cells were exposed to different concentrations of c-hBN and r-hBN. The cell viability was quantified by employing a fluorescent nucleic acid stain. Cells treated with r-hBN are insensitive to hBN concentration and shows negligible decrease in cell viability, whereas the c-hBN treated

cells shows a significant decrease in cell viability in a concentration dependent manner; the higher the concentration, the more significant the loss of cell viability (Figure 2.17a–e). To verify if the observed reduced cell viability due to c-hBN was caused by apoptosis, a TUNEL assay was employed. As expected, c-hBN exposed cells presented an increased number of apoptotic cells, in comparison to the control or r-hBN, in a concentration dependent manner (Figure 2.17f). These results indicate that higher concentration of c-hBN induces lysosomal permeabilization resulting in cell death. By contrast, r-hBN does not induce LMP, confirming our hypothesis.

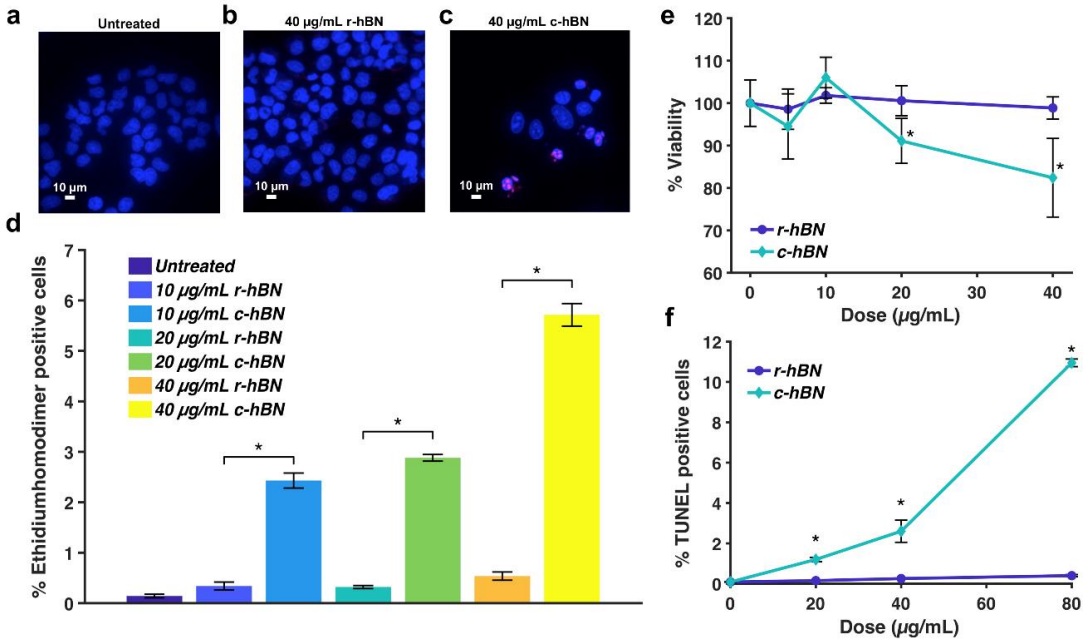

Figure 2. 17. a,**b**,**c**, Visualization of cell death in human epithelial cells after exposure to r-hBN or c-hBN for 24 h. Dead H460 cells are visualized in red. Hoechst staining (blue) was used to visualize the nucleus. (**a**) Control cells; (**b**) cells treated with 40 µg mL^{-1} of r-hBN; (**c**) Cells treated with 40 µg mL^{-1} of c-hBN. Cells exposed to c-hBN (**c**) showed a significant cell loss and red fluorescence, whereas unexposed cells (**a**) or cells exposed to r-hBN (**b**) did not exhibit a significant increase of toxicity. **d**, Cell death using ethidium homodimer/Hoechst fluorescence was determined using single cell quantitative high content imaging. After exposure of lung epithelial cells to r-hBN or c-hBN for 24 h, only c-hBN induced a significant, dose dependent increase of toxicity (*$p < 0.05$). **e**, Cell

viability was confirmed using Quant-iT™ PicoGreen dsDNA Assay Kit that quantitates DNA content. Following exposure of H460 cell with different concentrations of r-hBN and c-hBN for 24 h, viability was assessed. Concentrations above 20 μg mL^{-1} c-hBN caused a significant decrease in viability (*$p < 0.05$). **f**, TUNEL assay was performed to determine the induction of apoptosis. Apoptotic cells were assessed using single cell quantitative high content imaging. H460 cells were exposed to different concentrations of r-hBN and c-hBN for 24 h. Concentrations above 20 μg mL^{-1} c-hBN caused a significant increase of apoptotic cells (*$p < 0.05$).

2.4. Summary

In this work, we discovered for the first time a unique interaction mechanism between hBN flakes and lipid membrane: a sharp hBN could penetrate a lipid bilayer and form a cross-membrane water channel along its exposed polar edges, leading to lysosomal permeabilization. In contrast, a round hBN sheet could not penetrate a lipid bilayer due to high energy barrier and a lack of long enough polar edges. This mechanism is fundamentally different from several known membrane damaging mechanisms of graphene-based materials, including disruptive interactions with the plasma membrane [12, 41, 43, 44, 88, 89], and interruption of the mitochondrial function [44, 89, 90], resulting in oxidative stress responses [89-92], impairment of proteins [93], and DNA/RNA [94], and necrotic or apoptotic cell death [95]. Previous cellular studies and computer simulations suggest that stiffness and hydrophobicity of carbon-based nanomaterials are important factors that can impact lysosomal membrane integrity and trigger an increase in membrane permeability via lipid extraction [10, 12, 17], which consequently causes the release of cell death inducing enzymes (proapoptotic factors) [40, 44, 69]. In this study, we have also examined lipid extraction as a possible mechanism of membrane damaging. In our simulation, shortly after the hBN piercing into lipid bilayer, the system was relaxed for 40 ns without any pulling force. No significant lipid extraction was observed on c-hBN, but limited amount of lipid extraction was observed on r-hBN. Unlike lipid extraction induced by carbon nanomaterials, which takes place on both sides of a nanosheet [40, 78], lipid extraction induced by r-hBN was observed only on one side of an r-hBN sheet (Movies S10 and S11 in the published version [5]). Li et al. have demonstrated that convex, flat,

and concave BN surfaces exhibit different binding affinity to lipid molecules [58]. In our simulation, the r-hBN is slightly curved (Movie S12, in the published version [5]), resulting in selective lipid extraction on the concave side of hBN. Since r-hBN piercing the bilayer is hindered by a high energy barrier, whereas c-hBN cannot induce observable lipid extraction, even after successful piercing, and that r-hBN did not induce LMP in experiments, we can exclude lipid extraction as a significant membrane damaging mechanism of hBN. A recent study of commercial hBN samples (hBN nanopowder and hBN nanoplatelets) with round shapes shows low toxicity and no reduction in cellular viability in adenocarcinoma human alveolar basal epithelial cells (A549 cells), further supporting our hypothesis [4]. Therefore, water channel appears to be a unique cell interaction mechanism for hBN.

Apart from LMP, hydrophilic channels may have further implications, for example, in the rupture of lysosomes leading to a catastrophic release of hydrolytic enzymes to the cytoplasm, consequently causing disruption to the plasma membrane [96]. Other consequences include enabling fast proton transportation, which affects several biological processes and functions [97], and may cause leakage of other important biomolecules, e.g., DNA [98]. In our experimental part of this study, we have found that similar to other nanomaterials, cornered hBN can induce LMP leading to the liberation of cathepsin B in the cytoplasm (Figure 2.16e) and formation of superoxide anions (Figure 2.16i), accounting for a certain degree of toxicity on epithelial lung cells. The combination of enzyme release and ROS formation eventually led to cell dependent apoptosis. Although similar responses can be induced by other types of 2D materials including graphene and graphene oxide (e.g., graphene nanosheets enhanced LMP [99], and graphene oxide

affected lysosomal functions of astroglioblastoma derived cells [100]) we emphasize that the underlying mechanism via hBN induced water channel reported here is unique. Beyond cytotoxicity, our findings may have general implications and similar hydrophilic channels may exist in all binary or multielement 2D materials if they have polar edges. Such water channels can also be designed for a wide range of applications. For example, by functionalizing the hBN (or other binary/multielement 2D materials) and controlling its size and shape, the resulting water channel can be controllably opened or closed, or designed to open to a certain degree, thus achieving tunable permeability of the target membrane. In a biomedical context, hBN-induced water channels can be useful in treating human diseases involving lysosomal dysfunction [101] and ion channel defects [102]. It may also find applications in the treatment of cancer, and in targeted/smart drug delivery systems [103].

It is fair to point out that our FEP calculations of binding affinities between water/lipid and hBN were performed in vacuum condition to reduce the computational burden. In reality, the value of binding affinity in solution may change due to the addition of solvation free energy (the free energy change associated with the transfer of a molecule between ideal gas and solvent at a certain temperature and pressure) [104], which may become even more complicated for multicomponent lipid membrane [58], as each component's interaction with hBN needs to be specified. At this stage, we have not taken all such complications into consideration. In addition, we would like to clarify that it is beyond current experimental capabilities to directly visualize the hBN induced water channel in vitro, due in part to the lack of high-resolution in situ imaging methods and the close-to-transparent appearance of hBN under TEM. Nevertheless, we believe that the

combination of MD simulations, material preparation, in vitro imaging, along with physical reasoning, has provided sufficient evidence for the proposed water channel mechanism, which may prove to be generic for all binary/multielement 2D materials. This discovery may open a range of opportunities for further research, which, for instance, include strategies to functionalize hBN to achieve tunable channels and membrane permeability, thermodynamic and kinetic studies of ion/molecular transport along the channels, developments of drug delivery systems based on polar edges of 2D materials, and 2D material-based anticancer therapy.

Chapter 3

Mechanics of biosurfactant self-assembly on the interface of liquid-phase exfoliation of hexagonal boron nitride

The work described below is in collaboration with the experimental group of Dr. Alberto Bianco. Dr. Matteo Andrea Lucherelli and Dr. Alberto Bianco performed the liquid-phase exfoliation (LPE) experiments and characterized the exfoliated hBN samples. A part of this work on the interaction between Sodium Cholate (SC) and hBN was published on Advanced Materials (DOI: https://doi.org/10.1002/adma.202103137). A new paper on Flavin mononucleotide (FMN) assisted LPE of hBN is in preparation.

3.1. Introduction

Biosurfactant aided liquid-phase exfoliation (LPE) is emerging as a biocompatible, green, clean, economical, safe, and efficient approach to fabricating two dimensional (2D) materials for biomedical applications [24-27]. However, relatively little is known about the underlying molecular mechanisms for this process [105, 106]. Here, we present the first simulation study of how Flavin mononucleotide (FMN) and Sodium Cholate (SC) interact with hexagonal boron nitride (hBN) nanosheets in the context of LPE.

Flavin mononucleotide (FMN) is a phosphorylated derivative of vitamin B2. Consisting of an aromatic isoalloxazine ring and a phosphate moiety, FMN catalyzes important redox reactions in biological systems and serves as coenzymes and photoreceptors [107-109].

Experiments and theoretical studies have reported self-assembly of FMNs on single walled carbon nanotubes (SWCNTs) via π-π interactions and intermolecular hydrogen bonds (H-bonds) between the isoalloxazine moieties [110, 111]. FMN can induce graphene unzipping into nanoribbons ~10 nm in width via self-assembly [112], and is also an efficient surfactant to achieve stable dispersion of highly concentrated, defect-free, few-layer graphene flakes in water [113]. Recently, Ruiz and co-works reported that FMN dispersed graphene has very low cytotoxicity [30].

Despite a vast amount of research on carbon-based low dimensional materials, relatively less has been dedicated to boron nitride nanomaterials. Over the past decade, hexagonal boron nitride (hBN) has gained broad interests for potential applications as drug delivery systems, substrates for electronic and optoelectronic devices, and components in engineered composites due to its excellent chemical and thermal stability. However, many such applications rely on large-scale fabrication of the material [114]. Among various methods, liquid-phase exfoliation (LPE) can produce high yield, high quality 2D materials in water [27-29]. In particular, LPE aided by certain surfactant molecules has become an emerging topic of research [115]. For example, it has been shown that Sodium Cholate (SC) can help exfoliate and stabilize hBN nanosheets in an aqueous phase [116]. Gao and co-workers reported that FMN can disperse boron nitride nanotubes (BNNTs) in water via strong π-π interaction between FMN and BNNT [117, 118]. More recently, an experimental

work systematically studied nine surfactants for LPE of hBN in water, concluding that ionic surfactants are suitable for efficient exfoliation of hBN and can be optimized to increase the dispersion yield [119]. While no studies have reported the interaction between FMN and hBN, and the molecular mechanism of FMN assisted LPE remain largely unexplored, it can still be hypothesized that FMN molecules could interact with the basal plane of hBN in a similar way as in the case of Graphene.

In this section, we explored the molecular mechanism of FMN interacting with hBN in an aqueous phase via molecular dynamics (MD) simulations and free energy calculations. First, we studied the spontaneous deposition of a single FMN molecule onto hBN, focusing on the strong π-π interaction between FMN isoalloxazine moiety and the basal plane of hBN. Then, the interaction of two FMN molecules on hBN was investigated. The simulations demonstrated a self-assembly of FMNs on hBN via two persistent intermolecular H-bonds between the isoalloxazine moieties. We also studied the interaction of two FMN molecules in water without hBN, where the FMNs self-assemble via isoalloxazine stacking and intermolecular H-bonds between the ribityl phosphate moieties. The driving force for FMNs deposition and self-assembly was examined by analyzing the binding free energy at each binding site. These simulations indicated FMN to be a superb candidate as surfactant for LPE of biocompatible/non-toxic hBN in water. Although not covered in this thesis, pilot experiments from our collaborators have shown evidence of FMN being an efficient surfactant for exfoliation of hBN. Systematic LPE experiments and characterization of the exfoliated hBN are still on-going. A new paper on FMN assisted LPE of hBN is in preparation.

Another biosurfactant molecule we studied, Sodium cholate (SC), is a bile acid surfactant which has been widely used in assisting the LPE of Graphene and hBN in water [28, 105, 119]. It has been hypothesized that the hydrophobic moieties of SC can interact with the basal plane of hBN, while the negative charges of SC can stabilize the SC-coated hBN dispersion via electrostatic repulsion [116]. Although the hypothesis is plausible, no experimental or theoretical study had yet able to prove it. Like the study of FMN, we combined MD simulation, material fabrication, and characterization to unravel the molecular mechanism of SC in assisting the LPE of hBN. A part of this section was published on Advanced Materials.

We concluded this chapter by providing a guideline to the design of novel surfactant molecules for more efficient LPE of 2D materials, and potentially, aiding the delivery of novel nanomedicines.

3.2. Atomistic simulations

3.2.1. Simulation model and methodology

3.2.1.1. All-atom Molecular Dynamics (MD)

MD simulations based on the GROMACS package (version 2018.2) were performed to investigate the molecular deposition and self-assembly [59, 60]. FMN and SC molecules were modelled to be dissociated into sodium cations and anions in solution. Automated Topology Builder [120] was employed to generate the topologies and parameters of FMN and SC that were compatible with the GROMOS54a7 force field [121]. All the topologies and parameters can be downloaded freely from the website https://atb.uq.edu.au/index.py.

An empirical force field was adopted for hexagonal boron nitride (hBN) nanosheets [5, 61-63]. Simulation protocols were the same as described in section 2.2.1. The simulation box had an initial height ranging from 7.9 nm to 8.5 nm, with length and width both set to 6.0 nm. The values were large enough to prevent a surfactant molecule from interacting with its periodic images. The time step was set at 2 fs. After 50 ns initial equilibrium of a solvated hBN system, a surfactant molecule (FMN or SC) was introduced into the box by replacing some of the overlapping water molecules. The surfactant molecule, initially fixed in position, was released after 10 ns of re-equilibration for the actual/production simulation, and its interaction with the system was monitored. For the deposition simulation, the initial vertical center-of-mass (COM) distance between surfactant molecule and hBN was set to be 2 nm; For two surfactant molecules' self-assembly on hBN, one surfactant molecule was preloaded on hBN while another was placed 2 nm above hBN basal plane; for two surfactant molecules' self-assembly in water, the initial COM distance between two target molecules were set to be 4 nm. VMD was used to visualize the molecular deposition and self-assembly processes [74]. hBN and surfactant molecules were depicted as large spheres in Figure 3.2 and 3.6, and thickened tubes in Figure 3.3, 3.5 and 3.8. The atoms were colored as follows: hydrogen, white; boron, pink; carbon, cyan; nitrogen, blue; oxygen, red; phosphorus, tan.

3.2.1.2.Free Energy Perturbation (FEP)

FEP method was used to calculate the binding free energies associated with molecular deposition and self-assembly in solution and on hBN. Configurations for FEP calculations were extracted from the corresponding MD simulations. The protocol was

similar to described in section 2.2.1.3. A total of 26 intermediate states were used for FEP. The Multistate Bennett Acceptance Ratio (MBAR) method was used to calculate the change of free energy associated with the annihilation process [79]. Figure 3.1 shows the calculated binding free energies between SC and hBN, corresponding to forward and reverse sampling with a list of sampling length: 2 ns, 4 ns, 8 ns and 16 ns. The calculated binding free energies converged when the sampling length was equal to or greater than 4 ns. Hence, for all FEP simulations, each intermediate state was sampled for 4 ns to balance the accuracy and computational cost. At least three repetitions were conducted.

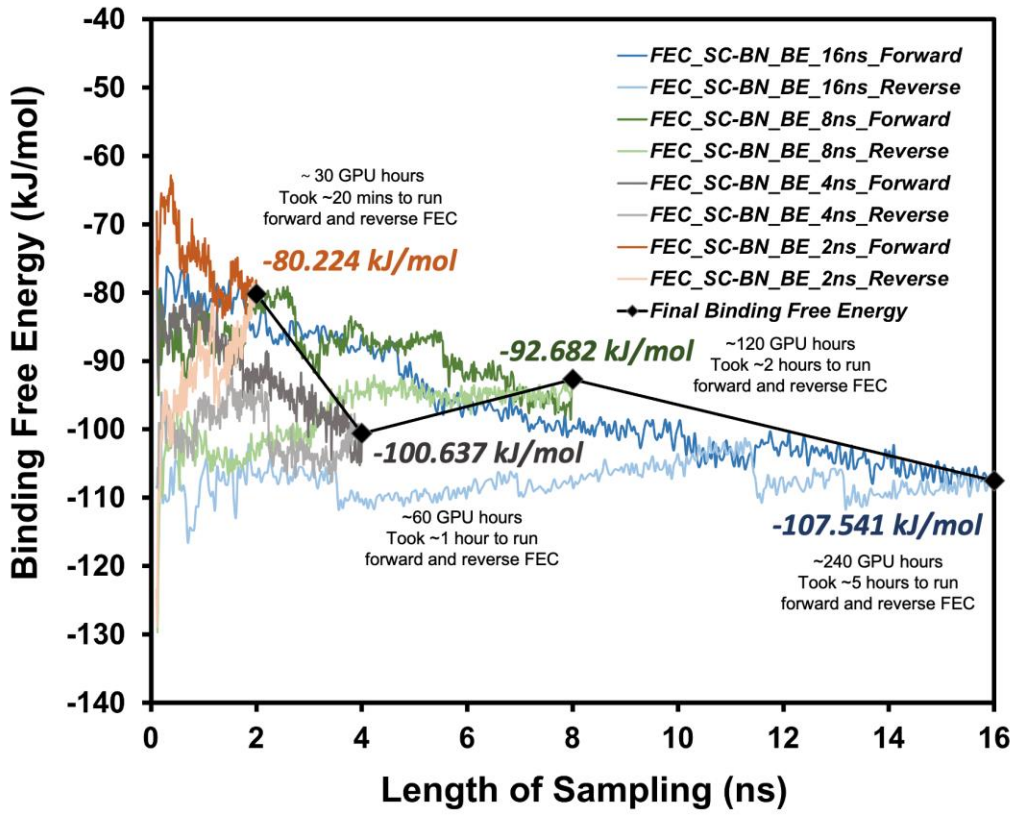

Figure 3. 1. The binding free energies between SC and hBN from the forward and reverse sampling of various sampling lengths. Details of FEC with each sampling length

are listed next to the corresponding final binding free energies. The 4-ns-long sampling is the sweet spot to balance the accuracy and computational costs.

3.2.2. Atomistic modeling and analysis of Flavin Mononucleotide (FMN)

3.2.2.1. Spontaneous deposition of FMN onto hBN

We simulated the interaction between an FMN molecule and a sheet of hBN. Representative simulation snapshots are shown in Figure 3.2b. At 5 ns, the FMN established initial contact with hBN via an oxygen atom (C_4=O) on isoalloxazine moiety. At 5.1 ns, the isoalloxazine moiety of FMN deposited parallelly onto the hBN basal plane. The ribityl-phosphate moiety of FMN remained in aqueous phase until 5.2 ns. After 5.2 ns, the FMN becomes fully deposited onto hBN, and its molecular structure no longer changed. No water molecules were trapped between the deposited FMN and hBN, and no H-bonds were formed between the two.

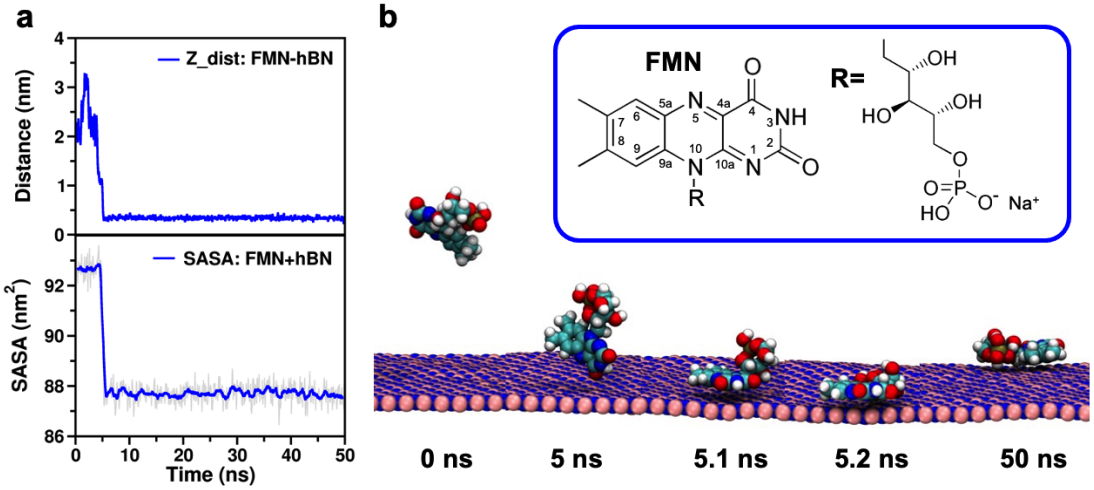

Figure 3. 2. a, Vertical center-of-mass distance (Z_dist) and Surface Accessible Surface Area (SASA) plot against simulation time for a Flavin Mononucleotide (FMN) to interact with hBN; **b**, Simulated trajectory of FMN interacting with hBN. The FMN established

initial contact with hBN at 5 ns and fully deposited onto hBN after 5.2 ns. Water molecules and sodium ion are not displayed for clarity. Inset: Chemical structure of FMN.

To quantify FMN deposition, we evaluated the vertical component of the center-of-mass distance (Z_{dist}) between FMN and hBN basal plane (Figure 3.2a, upper panel). Z_{dist} first increased to 3.27 nm at 1.7 ns, then gradually decreased to 2.41 ns at 3.9 ns, followed by a quick descent from 1.1 nm at 4.9 ns down to 0.32 nm at 5.2 ns. After 5.2 ns, Z_{dist} flattened out, with an average of 0.34 nm. A center-of-mass distance between FMN and hBN basal plane as small as 0.34 nm was clear evidence of strong π-π interaction [122]. Previous studies have also reported π-π interaction between FMN isoalloxazine moiety and SWCNT, Graphene, and BNNT [110-112, 117, 118].

To further understand FMN deposition, we calculated the solvent accessible surface area (SASA) for the complex of FMN and hBN (FMN+hBN). In principle, SASA gives the surface area of a molecule (or a group of molecules) which is accessible to a solvent [123], and can serve as a key indicator for molecular interaction with the surrounding solvents, as in self-assembly [124] and protein folding [125]. In the lower panel of Figure 3.2a, SASA first fluctuated near an initial value of 92.7 nm^2 until 4.9 ns; after 4.9 ns, it quickly dropped from 92.7 nm^2 to 87.2 nm^2 at 5.3 ns. After 5.3 ns, it plateaued to an average of 87.7 nm^2.

Both SASA and Z_{dist} captured the crucial events in the FMN deposition process. The timing of each turning point in SASA plot overlapped perfectly with Z_{dist}. Between 0 and 4.9 ns, the fluctuations of Z_{dist} and SASA near their initial values suggested FMN remaining in the aqueous phase, i.e., pre-deposition state; Between 4.9 and 5.2 ns, the steep

descent in Z_{dist} and SASA indicated a strong driving force for the FMN deposition; From 5.2 ns onwards, the plateaus in Z_{dist} and SASA plots demonstrated that the fully-deposited FMN is stable (Z_{dist} did not change) and its interaction with surrounding solvents robust (SASA did not change). Hence, the simulation and analysis unveiled that:

(1) FMN could spontaneously deposit from the aqueous phase to the hBN basal plane,

(2) The deposition was initiated by the attachment of isoalloxazine moiety on the hBN basal plane, due to π-π interaction,

(3) The driving force for FMN deposition was strong, but no H-bonds were involved.

3.2.2.2. Spontaneous self-assembly of FMN molecules on hBN

We further simulated interaction of multiple FMNs with hBN in water. Particularly, the interaction between two FMN molecules as well as between FMN and hBN were studied. Such interactions were the basis for more complicated, higher-order assembly (i.e., supramolecular assembly). Prior to simulation, one FMN molecule, FMN2, was pre-attached on hBN (configuration was taken from the deposition simulation), while another FMN molecule, FMN1, was placed 2 nm above hBN basal plane and released. Molecular interactions between FMNs and hBN were monitored by Z_{dist} and SASA. 32.1 ns after release, FMN1 deposited from the aqueous phase onto FMN2, as indicated by the dashed box in Figure 3.3a. A stacking between isoalloxazine moieties of FMN1 and FMN2 was observed, as shown in Figure 3.3c. No H-bonds were found between FMN1 and FMN2 during isoalloxazine stacking. The ribityl-phosphate moiety of FMN1 was pushed away from FMN2 due to electrostatic repulsion. The isoalloxazine moiety of FMN2 remained

parallel to hBN during isoalloxazine stacking. Similar isoalloxazine stacking configuration was reported in experiments [126, 127]. Between 32.1 and 34.5 ns, Z_{dist} between FMN1 and FMN2 fluctuated around 0.5 nm, indicating π-π interaction between isoalloxazine moieties of FMN.

The isoalloxazine stacking configuration, however, did not survive long. 2.4 ns after its formation (34.5 ns), FMN1 detached from FMN2. At 35.1 ns, FMN1 directly deposited onto the hBN basal plane, suggesting a stronger driving force for deposition than for isoalloxazine stacking on hBN. After 35.1 ns, Z_{dist} between FMN1 and hBN leveled off to an average of 0.34 nm. Z_{dist} between FMN2 and hBN plateaued for the entire simulation, with the same average value of 0.34 nm. Once again, the average Z_{dist} of 0.34 nm and the stacking configuration indicated π-π interaction between isoalloxazine moieties and the basal plane of hBN.

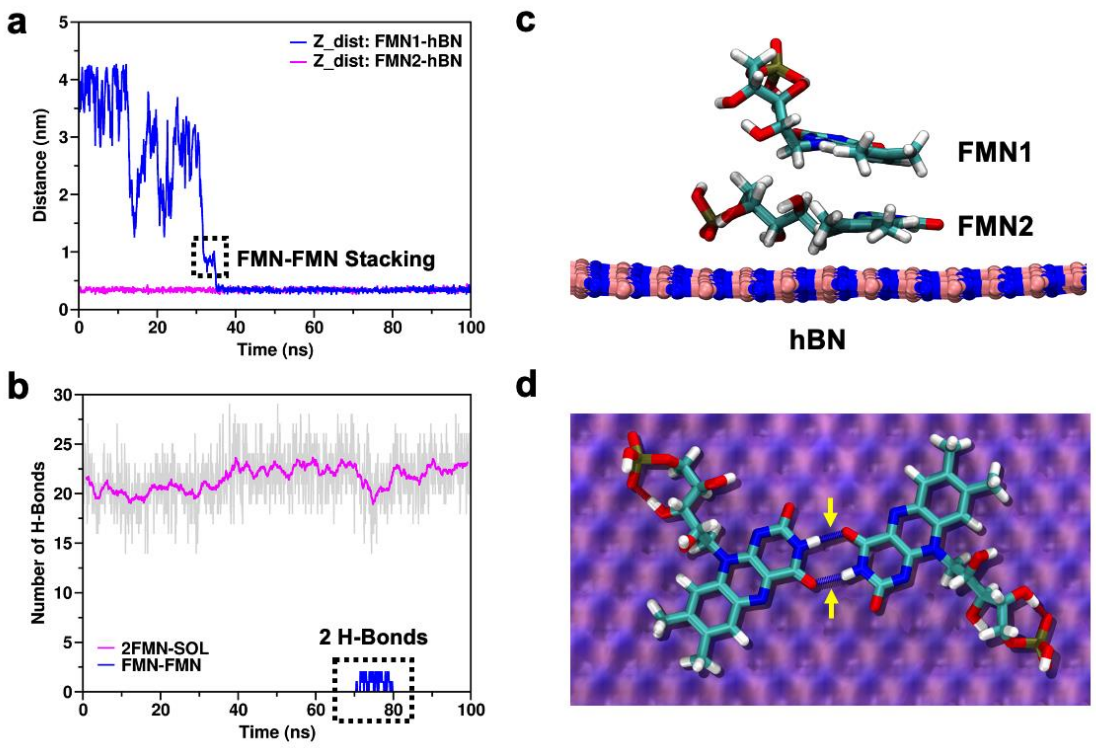

Figure 3. 3. a, Evolution of vertical center-of-mass distance (Z_dist) in the 2FMN-hBN simulation. The dashed box indicates the onset of FMN-FMN stacking on hBN. **b**, Total number of H-Bonds between FMN molecules and water (2FMN-SOL: magenta), as well as between two FMN molecules (FMN-FMN: blue). The dashed box highlights the period of FMN self-assembly on hBN via 2 H-Bonds, between 70 ns and 80 ns. **c**, Simulation snapshot of FMN1 stacking on the isoalloxazine moieties of pre-loaded FMN2 before depositing onto hBN basal plane. **d**, Simulation snapshot of FMN self-assembly on hBN. The assembly is stabilized by two inter-isoalloxazine H-bonds, as highlighted by the yellow arrows. The H-bonds are found between N_3-H and C_4=O atoms on the isoalloxazine moieties of FM1 and FM2. Water molecules and sodium ions are not displayed for clarity.

Between 70.5 and 79.7 ns, the two FMN molecules were found to undergo self-assembly on hBN, as highlighted by the dashed box in Figure 3.3b. Two persistent H-bonds were observed between a donor N_3-H, and an acceptor C_4=O on the isoalloxazine moieties of FM1 and FM2, respectively. Similar patterns of self-assembly had been reported in experiments [110, 112, 128]. Figure 3.3d is a magnified MD snapshot showing the

intermolecular H-bonds between isoalloxazine moieties, which stabilized the FMN self-assembly on hBN. At 79.7 ns, the self-assembly disintegrated due to H-bond disruption.

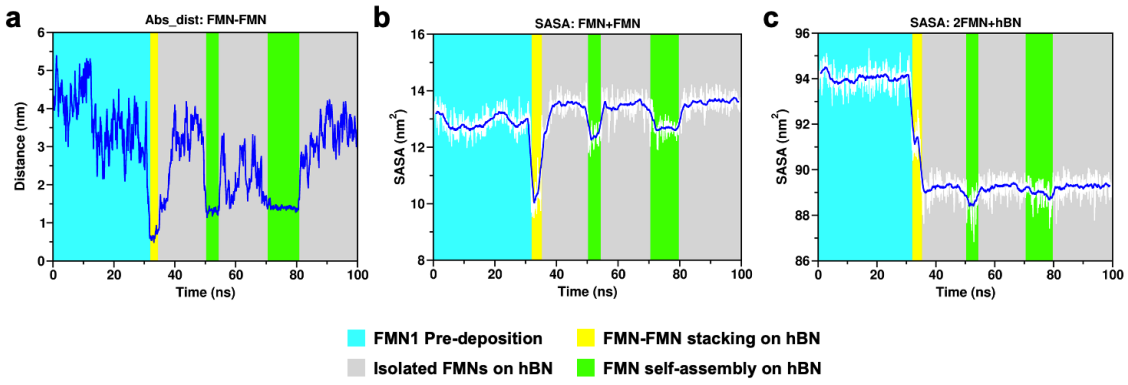

Figure 3. 4. a, Evolution of the absolute center-of-mass distance (Abs_dist) between the two FMN molecules in the 2FMN-hBN simulation. **b-c**, Evolution of the solvent accessible surface area (SASA) for the complex of two FMN molecules, i.e., FMN+FMN (**b**), as well as the complex of two FMN and hBN, i.e., 2FMN+hBN (**c**). Color palettes in each graph implies different stages of interaction, cyan: FMN1 in the aqueous phase, yellow: FMN-FMN stacking on hBN, grey: both FMNs deposited on hBN basal plane but isolated from each other, green: FMN self-assembly on hBN basal plane.

To better understand the process of FMN self-assembly on hBN, three indicators were evaluated:

(1) The absolute COM distance (Abs_{dist}) between FMN1 and FMN2,

(2) SASA for a complex of 2 FMNs (FMN-FMN),

(3) SASA for a complex of 2 FMNs and hBN (2FMN+hBN).

As shown in Figure 3.4, four stages of simulation were highlighted by corresponding colors in the background of each graph. During FMN-FMN stacking and FMN self-assembly, all three indicators showed local minimum behaviors. We noticed another period of FMN self-assembly between 50.3 and 54.4 ns. The simulation trajectory revealed such

self-assembly was due to non-covalent, hydrophobic interaction between the methyl groups on the isoalloxazine moieties of FM1 and FM2, and no H-bonds were formed between FM1 and FM2 in this assembly. At 54.4 ns, the hydrophobicity-driven self-assembly disintegrated due to a shift in relative position of the FMNs, breaking the hydrophobic interaction between methyl groups.

For FMN deposition on hydrophobic substrates such as CNT, it was reported that the ribityl phosphate moiety of FMN always remained in the aqueous phase, providing an anionic repulsion between nanotubes [129]. However, our study showed that the ribityl phosphate moieties would deposit onto hBN basal plane. Upon deposition, the ribityl-phosphate moiety oriented almost perpendicular to the isoalloxazine moiety, increasing the total occupied area per FMN molecule on hBN, thereby negatively affecting the maximal areal density of FMN deposited on hBN. On the other hand, our simulation showed that the overall structure of deposited FMN was stable and robust. With the FMN molecules undergoing self-assembly along the direction of isoalloxazine moieties, while the deposited ribityl phosphate moieties acted as spacers/interfaces between FMN directional self-assemblies, it suggests a new, non-covalent, chemical pathway of functionalizing hBN with one-dimensional / directional FMN self-assembly, similar to the case of Graphene [112].

Apart from stacking and self-assembly, we also observed large fluctuations of Abs_{dist} in FMN pre-deposition (cyan color) and isolation on hBN (grey color). Although restricted to move only in-plane, the simulation trajectory revealed that a deposited FMN could still move freely on the basal plane of hBN. Hence, the FMN remained highly mobile after deposition onto hBN basal plane. Similar phenomenon had been reported in simulation and experiment, where a deposited planar molecule exhibits unimpeded mobility on 2D

material surface, due to low energy barriers comparable to the thermal energy at room temperature for rotation and displacement on the basal plane of 2D materials [130, 131].

3.2.2.3. Self-assembly of FMN molecules in solution

It has been reported that FMNs could self-assemble in water via isoalloxazine stacking into dimers [126, 127, 132]. To test the validity of our model, we simulated the interaction of two FMN molecules in water (without hBN). The equivalent concentration of FMN was 11 mM, a value known for its self-assembly [133]. The critical events of FMN self-assembly in water in Figure 3.5c suggest three stages of interaction: (1) Pre-assembly stage (0 - 35 ns), (2) Initiation stage (35 - 60 ns), and (3) Stabilization stage (60 - 100 ns). Prior to 35 ns, the two FMNs were essentially isolated, as indicated by the large fluctuation of Abs_{dist} (Figure 3.5a). At 35 ns, Isoalloxazine stacking was observed to initiate FMN self-assembly. After this, the ribityl-phosphate moieties experienced reorientation until two intermolecular H-bonds were formed between ribityl phosphate moieties of FMN1 and FMN2, at 60 ns. The molecular structure of FMN self-assembly remained unchanged until 78 ns, when a “ratcheting” movement shifted the relative position of ribityl phosphate moieties on FMN1 and FMN2, breaking an H-bond. From 91 ns onwards, the broken H-bond was restored, and the structure of the assembly no longer changed. Despite the changes in H-bonds, the isoalloxazine stacking seemed robust following the onset of self-assembly (35 ns).

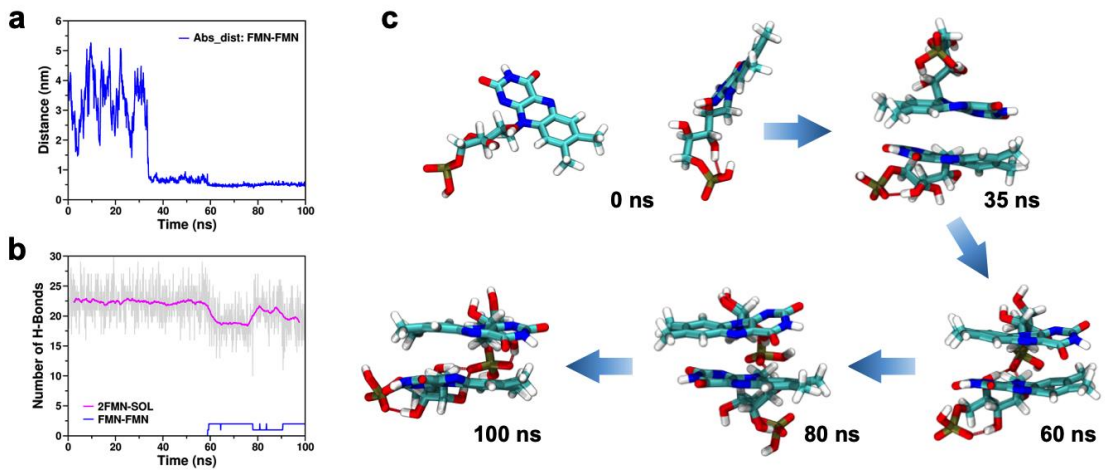

Figure 3. 5. (a) Evolution of the absolute center-of-mass (COM) distance (Abs_dist) between two FMN molecules in solution. (b) Total number of hydrogen bonds (H-Bonds) between the FMN molecules and water (2FMN-SOL: magenta), as well as between the two FMN molecules (FMN-FMN: blue). The self-assembly of FMNs saturates at 2 inter-FMN H-Bonds. (c) Simulation snapshots showing the critical steps of FMN self-assembly in solution. The self-assembly process is initiated by isoalloxazine stacking (35 ns) and stabilized by inter-FMN H-bonds (from 60 ns onwards). Water molecules and sodium ions are not displayed for clarity.

To quantify FMN self-assembly in water, the absolute center-of-mass distance between FMNs and the number of H-bonds were monitored (Figure 3.5a-b). In the approaching stage, the Abs_{dist} first fluctuated near its initial value of 4 nm until 33.3 ns, then quickly decreased to 0.68 nm at 35 ns. In the assembly stage, Abs_{dist} reached the first plateau at an average value of 0.67 nm. In the post-assembly stage, Abs_{dist} decreased to 0.483 nm at 60ns, then reached the second plateau with an average value of 0.52 nm, indicating π-π interaction between the isoalloxazine moieties of FMN.

In general, the Abs_{dist} indicator accurately described the approaching stage (0~35 ns). However, the change of absolute COM distance was barely noticeable (~0.1 nm) after the

approaching. Fortunately, the number of H-bonds between FMN molecules ($N_{FMN-FMN}$) could probe the later stages with high accuracy. As shown in Figure 2c, $N_{FMN-FMN}$ increased from 0 to 2 at 59.4 ns, then plateaued until 78.1 ns. Between 78.1 ns and 90.6 ns, $N_{FMN-FMN}$ temporarily dropped to 1, before regaining N=2 from 90.6 ns onwards. We also calculated the number of H-bonds between FMN and solvent (water) molecules, $N_{mol-sol}$. An interesting trend was observed: the timing of a decrease in $N_{mol-sol}$ overlapped perfectly with the increase of $N_{FMN-FMN}$, and vice versa for the increase of $N_{mol-sol}$. This is because the maximum number of H-bonds in a FMN with external environment is determined by its H-bond donors and acceptors. To establish or break an H-bond with another FMN molecule, the number of donors and acceptors available for solvent molecules would decrease or increase, correspondingly. The evolution of $N_{FMN-FMN}$ and of $N_{mol-sol}$ suggested that FMN self-assembly in water saturated at two persistent intermolecular H-bonds (between ribityl phosphate moieties). Thus, our simulation and analysis agreed well with existing literature in that FMNs in solution could spontaneously self-assemble into dimers via π-π interaction between the isoalloxazine moieties and two intermolecular H-bonds between ribityl-phosphate moieties.

3.2.3. Atomistic modeling and analysis of Sodium Cholate (SC)

To investigate the interactions between SC molecules and hBN, all-atom MD simulations were performed. The simulation box had an initial height ranging from 7.9 nm to 8.5 nm, with length and width both set to 6.0 nm. The values were large enough to prevent a SC molecule from interacting with its periodic images. After a 50 ns initial

equilibration of a solvated hBN system, a SC molecule was introduced at the center of the simulation box to replace some of the overlapping water molecules. The SC molecule, initially fixed in position, was released after 10 ns of re-equilibration for the actual simulation. Figure 3.6a shows the trajectory of the SC molecule interacting with hBN. At 3.1ns after releasing, it moved to the vicinity of the hBN and established a loose attachment with hBN via its polar carboxylate group; between 3.1 ns and 3.9 ns, the SC molecule underwent some orientational alignments and became firmly attached to hBN, as evidenced by a decrease in SC-hBN interaction energy (Figure 3.6d); from 4.1 ns to 20 ns, the SC molecule migrated on hBN while remaining firmly attached to it (Figure 3.6d, inset) with negligible change in the interaction energy.

We have also simulated multiple SC molecules interacting with hBN. In the case of two SCs (Figure 3.6b), the initial configuration consisted of one SC firmly attached on hBN (pre-coated SC) and the other initially introduced at the center of the simulation box before setting free (free SC). The free SC established loose attachment with hBN at 17.9 ns, followed by firm attachment at 18.4 ns. At 45 ns, the two SCs self-assembled into a dimer via hydrophobic interactions. The self- assembled SC-SC dimer remained stable for the entire duration of the 50 ns simulation period; further simulation for another 50 ns confirmed its stability. In the case of 14 SCs (Figure 3.6c, Movies S13, S14 in the SI of the published work[5]), with 13 pre-coated on hBN and one free, the free SC became attached on top of the pre-coated SCs at 2.6 ns and then slid down to establish direct contact with hBN at 7.6 ns. From 7.6 ns to 20 ns the initially free SC became incorporated into the existing SCs to form a slightly larger monolayer coating on hBN. A top view of the final snapshot taken at 20 ns is shown in Figure 3.6e.

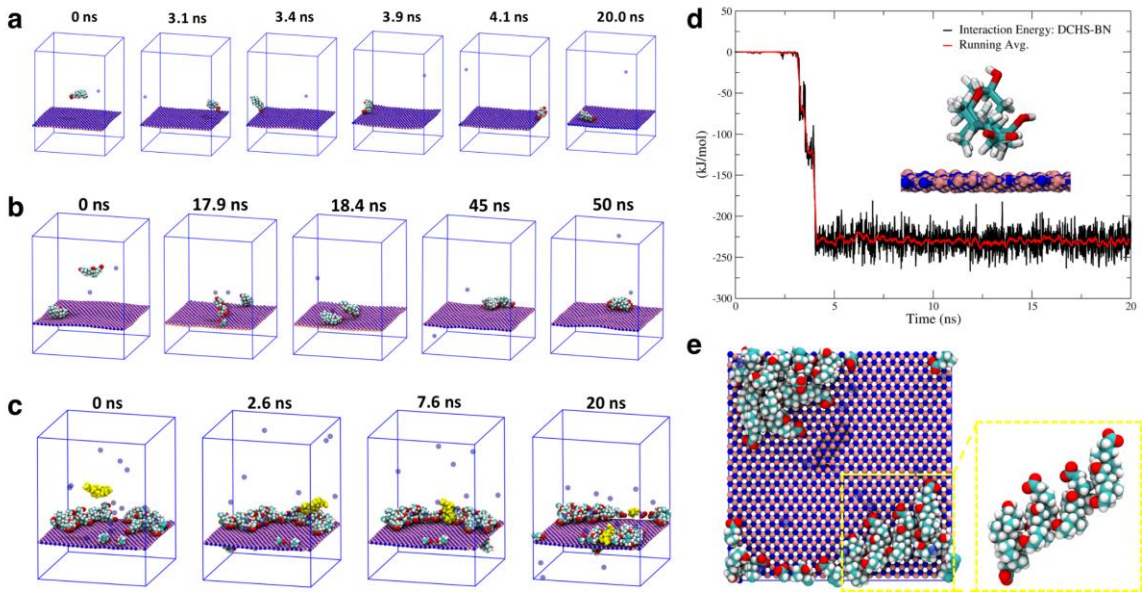

Figure 3. 6. Time evolution of SC molecules interacting with an hBN sheet: **a**, a single, initially free, SC molecule landing and attaching to the hBN; **b**, an initially free SC attaching and self-assembling with another SC pre-coated on hBN; **c**, an initially free SC depositing and incorporating into a monolayer of 13 SCs pre-coated on hBN; **d**, interaction energy between SC and hBN; inset: configuration of an SC after its firm attachment on hBN; **e**, top view of the configuration shown in (**c**) at 20 ns; inset: magnified view of a self-assembled SC aggregate within the area marked with yellow dashed box.

FEP method was used to calculate binding affinities associated with the interaction between SC molecules and hBN. The processes used to calculate the binding affinities are illustrated in Figure 3.7. In Figure 3.7a, we first determined the energy difference ΔG_{AB} between a monolayer hBN (marked with letter "Q") in water (state A) and in vacuum (state B), and then the energy difference ΔG_{BC} between a monolayer hBN in vacuum (state B) and when it is in a bilayer hBN (state C). The hBN-hBN binding affinity is calculated as: $\Delta G_{bind}^{hBN} = \Delta G_{AC} = \Delta G_{AB} + \Delta G_{BC}$. Similarly, in Figure 3.7b, we determined the energy difference ΔG_{DE} between a single SC molecule in water (state D) and in vacuum (state E), and then the energy difference ΔG_{EF} between the SC in vacuum (state E) and when it is

firmly attached on hBN (state F). The SC-hBN binding affinity is calculated as: $\Delta G_{bind}^{SC-\mathrm{h}BN} = \Delta G_{DF} = \Delta G_{DE} + \Delta G_{EF}$. In Figure 3.7c, we determined the energy difference ΔG_{GH} between a SC pre-coated on hBN (state G) and in vacuum (state H), and then the energy difference ΔG_{HI} between a SC in vacuum (state H) and when it is in a self-assembled SC-SC dimer on hBN (state I). The SC-SC binding affinity on hBN is: $\Delta G_{bind}^{SC-SC\,(\mathrm{h}BN)} = \Delta G_{GI} = \Delta G_{GH} + \Delta G_{HI}$. The calculated binding affinities were summarized in Table 3.1, with all values normalized by the contact area. The negative values of $\Delta G_{bind}^{SC-\mathrm{h}BN}$ and $\Delta G_{bind}^{SC-SC\,(\mathrm{h}BN)}$ suggest both SC-hBN binding and SC-SC self-assembly are energetically favorable.

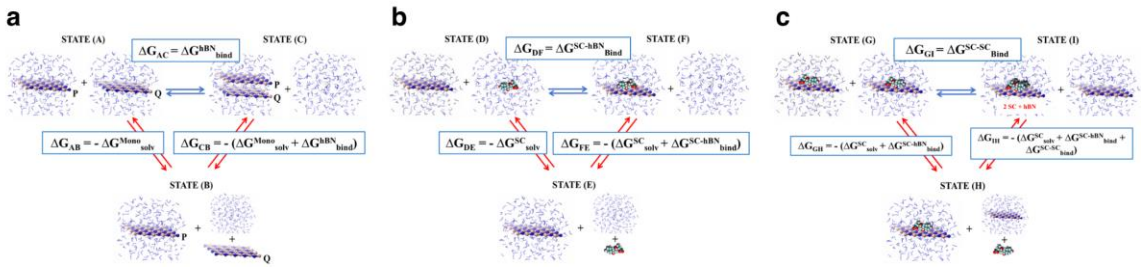

Figure 3. 7. Computational processes for calculating free energy differences ΔG between the following states: **a**, a monolayered hBN in water, in vacuum, and when it is in a bilayer hBN; **b**, an initially free SC in water, in vacuum, and when it is firmly attached on hBN; and **c**, a SC pre-coated on hBN, in vacuum, and when it is in a self-assembled SC-SC dimer on hBN.

Table 3. 1. Normalized binding free energies in SC-hBN interaction.

Name	$\Delta\widetilde{G}_{bind}^{hBN}$	$\Delta\widetilde{G}_{bind}^{SC-hBN}$	$\Delta\widetilde{G}_{bind}^{SC-SC\ (hN)}$
(kJ/mol nm^{-2})	-630.51 ± 0.27	-104.30 ± 2.29	-25.28 ± 3.70

3.2.4. Driving force of biosurfactant deposition and self-assembly on hBN

The molecular self-assembly from solution to substrate is usually governed by the balance between molecule–substrate, molecule–molecule, solvent–substrate and molecule–solvent interactions [134]. To understand these interactions in FMN deposition and self-assembly, binding energies ΔG were calculated at three different sites, FMN-hBN, FMN-FMN in solution and FMN-FMN on hBN. Molecular configurations for the calculation were taken from the MD simulations. We compared the results side-by-side with the binding energies of SC, an efficient biosurfactant molecule that is known to assist LPE of graphene and hBN [28, 116], as shown in Table 3.2.

Table 3. 2. The binding free energies of FMN and SC molecules at binding sites of interests

Molecule Name	Flavin Mononucleotide (FMN)	Sodium Cholate (SC)
$\Delta G_{Mol-hBN}$ [a†]	-141.028 ± 0.498	-100.480 ± 6.083
$\Delta G_{Mol-Mol}$ (in solution) [b†]	-80.330 ± 7.127	-46.314 ± 1.726
$\Delta G_{Mol-Mol}$ (on hBN) [c†]	-95.454 ± 6.514	-29.026 ± 5.433

(kJ/mol)

[a] Reference state: the target molecule is in solution and infinitely far away from hBN; Final state: the target molecule is on hBN (the binding site).

[b] Reference state: both target molecules are in solution and infinitely far away from each other; Final state: two target molecules self-assemble into a stable aggregate/dimer in solution.

[c] Reference state: both target molecules are on hBN but infinitely far away from each other; Final state: two target molecules self-assemble into an aggregate/dimer on hBN.

[†] Abbreviations: Mol-hBN stands for molecular binding between one target molecule and hBN, Mol-Mol stands for molecular binding between two target molecules, either in solution or on hBN.

Since the calculated ΔG values are all negative, the corresponding binding process should be energetically favorable, consistent with MD simulations. For a FMN molecule

to bind onto hBN basal plane, the free energy would drop by $\Delta G_{FMN\text{-}hBN}$ = 141.028 kJ/mol. In comparison, the adsorption energy of FMN on SWCNT is 2 eV [135, 136], which is within the same range as our calculation. For two FMNs preloaded on hBN to self-assemble via two H-bonds, the total free energy would drop by $\Delta G^{(hBN)}_{FMN\text{-}FMN}$ = 95.454 kJ/mol. In comparison, for two FMNs to form an assembly via isoalloxazine stacking in water, the total free energy would drop only by $\Delta G^{(Water)}_{FMN\text{-}FMN}$ = 80.330 kJ/mol. Although ΔG for FMN-FMN stacking on hBN was not calculated, the MD trajectory, Z_{dist} and SASA already showed FMN-hBN binding to be stronger than FMN-FMN stacking on hBN. Moreover, FMN-FMN stacking on hBN and in solution are both dominated by π-π interaction. Hence, if we assume ΔG in both cases to be identical, we will see a driving force of 15.124 kJ/mol in favor of FMN-hBN binding than FMN-FMN stacking on hBN.

We also found that SC binding to the sites of interest is weaker than FMN. Particularly, SC self-assembly on hBN would decrease total free energy by $\Delta G_{SC\text{-}hBN}$ = 29.026 kJ/mol, only 1/3 times that in the case of FMN. Contrary to FMN self-assembly on hBN, SC self-assembly on hBN appeared to be dominated by hydrophobic interaction. No H-bonds were found in the assembly. SC molecules oriented in a "back-to-back" fashion to shield the hydrophobic methyl groups from water, while all hydrophilic groups (hydroxyl groups and carboxylate group) were facing towards the aqueous phase to reduce energy penalty (Figure 3.8, 3.9). Based on the energetics, we propose that FMN should be an efficient surfactant/stabilizer for LPE of hBN, which may stabilize higher concentration of hBN dispersion in water as compared to the case of SC.

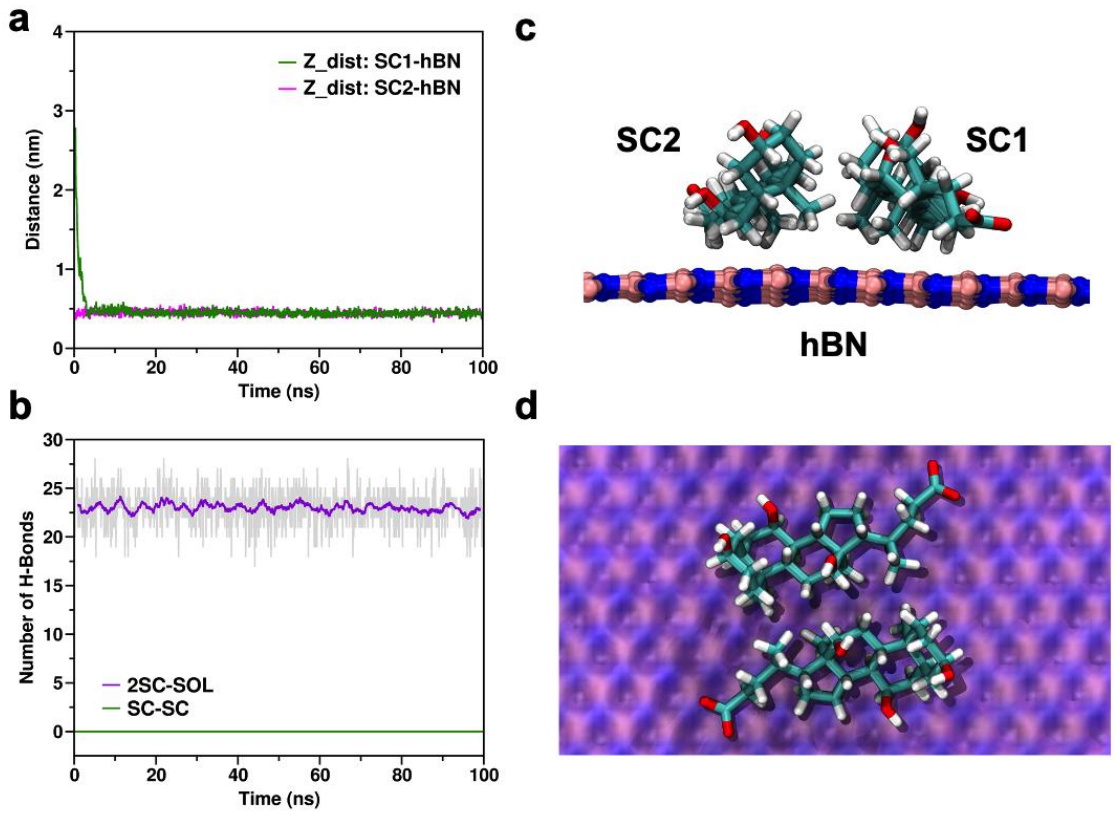

Figure 3. 8. a, Evolution of vertical center of mass distance (Z_dist) in the 2SC-hBN simulation. **b**, Total number of H-Bonds between SC molecules and water (2SC-SOL: purple), as well as between two SC molecules (SC-SC: green). No H-bonds are formed during the self-assembly of two SC molecules on hBN. **c-d**, Simulation snapshot showing SC-SC assembly after SC1 fully deposited on hBN. The side view (**c**) unveils no H-bonds in the SC self-assembly. Instead, the assembly is held together by the hydrophobic methyl moieties. The top view (**d**) reveals that SC molecules orient in a "back-to-back" fashion to shield the hydrophobic methyl groups from water, while all hydrophilic groups (hydroxyl groups and carboxylate group) are facing towards the aqueous phase. Water molecules and sodium ions are hidden for clarity.

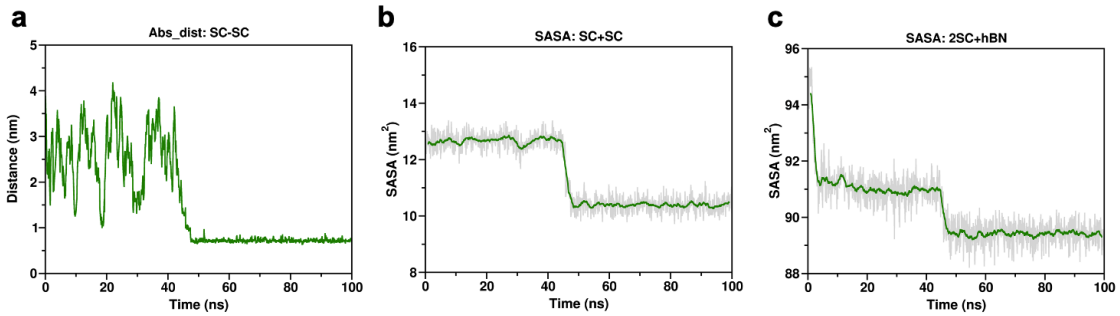

Figure 3. 9. a, Evolution of the average center of mass distance between two SC molecules in the 2SC-hBN simulation. **b-c**, Evolution of SASA for complex of two SC molecules, i.e., SC+SC (**b**) and complex of two SC and hBN, i.e., 2SC+hBN (**c**).

3.2.5. Guidelines to the design of novel surfactant molecules for LPE

Finally, we purpose a guideline for the design of future generation biosurfactant molecules to enhance LPE:

(1) Aromatic/flat molecules (FMN) can be functionalized with donors and accepters, makes them rich in H-bond donors and accepters, to boost H-bonds formation.

(2) Non-aromatic molecules (SC) can be made amphiphilic with adequate hydrophobic and hydrophilic functional groups, to enhance hydrophobic interaction on 2D material substrates.

3.3. Discussions

3.3.1. Literatures showing the self-assembly of FMN on substrates

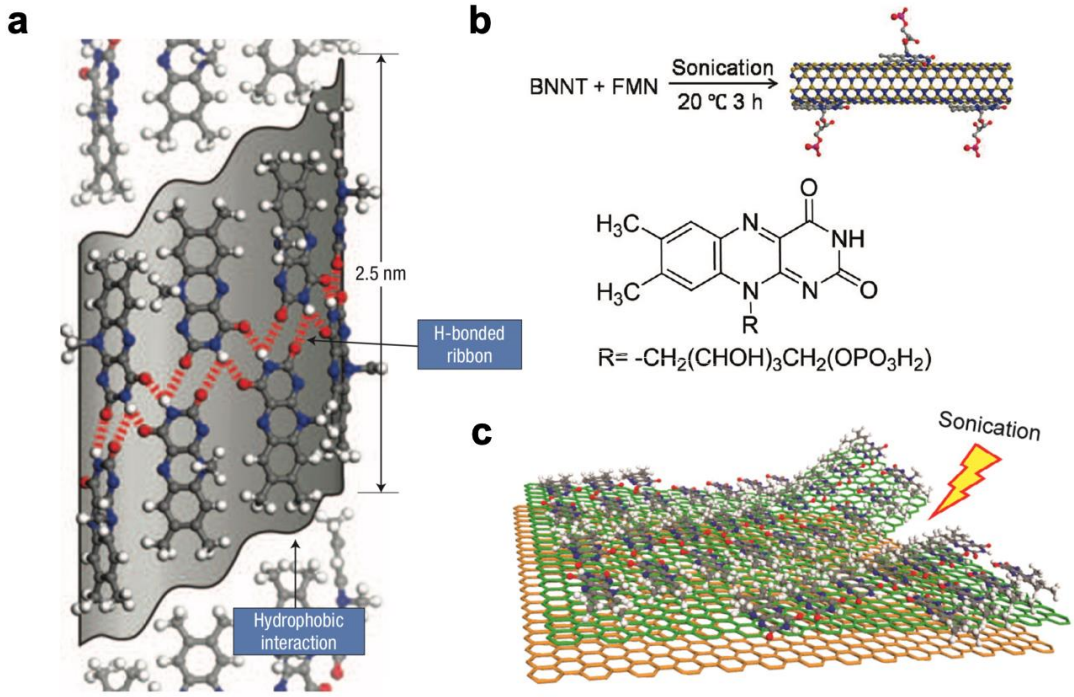

Figure 3. 10. a, Top view of FMN wrapped around an 8_1 SWCNT in helical pattern, stabilized by H-bonds between adjacent isoalloxazine moieties and hydrophobic interaction between FMN and the side wall of SWCNT [110]. **b**, Schematic representation of the formation process of an FMN/BNNT Nanohybrid, where π-π stacking interactions between FMN and BNNT play an important role [117]. **c**, Pictorial illustration of FMN assembly-assisted unzipping of graphene into graphene nanoribbons (GNR) upon sonication. Unzipping is propagated along the weak interaction line between dimethyl tail groups [112].

3.3.2. Evaluation of the quantity of SC deposited on c-hBN and r-hBN

The quantity of SC adsorbed onto the surface of c-hBN and r-hBN was evaluated by X-ray photoelectron spectroscopy (XPS) and elemental analysis methods. The XPS analysis was carried out on hBN powder deposited on double face Cu scotch tape (Farnell, 19 mm, mod. 1182). The percentage composition of the samples was evaluated through the deconvolution of survey spectra (Figure 3.11), showing 4.5% w/w and 3.0% w/w (mass ratio) of SC deposited on c-hBN and r-hBN, respectively.

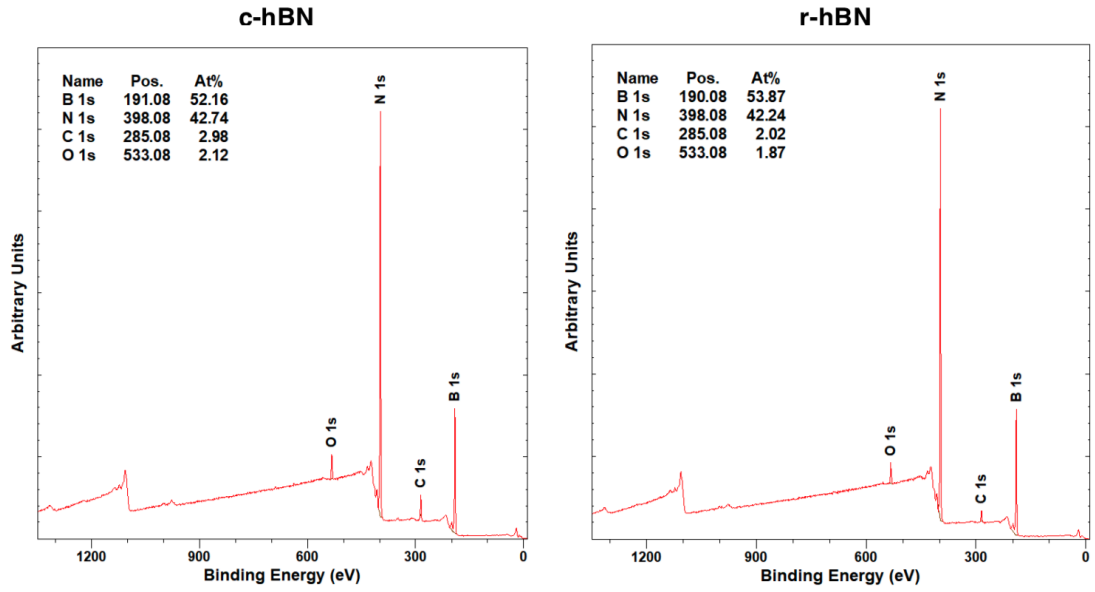

Figure 3. 11. XPS survey spectra of the c-hBN and r-hBN powders.

Similar mass ratios of SC deposited on c-hBN and r-hBN were obtained by elemental analysis (Table 3.3). c-hBN appears to adsorb more SC molecules per unit mass than r-hBN, probably due to the polar free zigzag edges in the c-hBN flakes. However, in this chapter, we mainly focus on the interaction between surfactant molecules and the basal

plane of hBN. We did not study the edge effect in such interactions. Nevertheless, we confirm experimentally that SC can spontaneously deposit onto the surface of c-hBN and r-hBN.

Table 3. 3. Quantity of SC adsorbed onto hBN was evaluated using XPS and elemental analysis (EA), and similar values of weight percentage of carbon and SC/hBN mass ratio were obtained from both methods.

Samples	***Weight % C*** *(XPS)*	***Weight % C*** *(EA)*	***w/w % SC/hBN*** *(XPS)*	***w/w % SC/hBN*** *(EA)*
r-hBN	2.02	1.75	3.0	2.6
c-hBN	2.98	2.42	4.5	3.6

3.4. Summary

In this chapter, we have demonstrated that FMN and SC molecules can self-assemble on hBN via a toolbox of mechanisms including: π-π interactions between the FMN isoalloxazine moieties and the basal plane of hBN, intermolecular hydrogen bonds (H-bonds) between the FMN isoalloxazine moieties, and hydrophobic interaction between the SC methyl moieties. Three MD simulations were setup to analyze the molecule behavior in FMN deposition and self-assembly. We used the FEP method to pinpoint the driving force, and proposed FMN to be superior/better than SC in assisting LPE of hBN. Experimental evidence has confirmed the theoretical/simulation results. Through all our comprehensive simulations and experiments, we can conclude that both FMN and SC are both efficient surfactants in assisting LPE of hBN in water. These surfactants might also be useful in the scalable production of other 2D materials [137]. We concluded by providing a general guideline for the design of novel surfactant molecules for efficient LPE of 2D materials: functioning the aromatic/flat molecules (such as FMN) with H-bond donors and accepters, boosting the formation of H-bonds, and making non-aromatic molecules (such as SC) amphiphilic to enhance their hydrophobic/hydrophilic interaction in water and on 2D materials. These findings could aid the design of novel surfactant molecules for more efficient LPE of 2D materials, and the development of novel nanomedicine delivery systems.

Chapter 4

Molecular mechanisms of coacervation and encapsulation with designed peptides

The work described below is in collaboration with the research groups of Prof. Jing Yu, Prof. Tian Liu and Prof. Konstantin Pervushin. Prof. Tian Liu's group performed the transcriptome analysis. Prof. Jing Yu and Prof. Tian Liu's groups performed the selection, *De novo* synthesis and characterization of the target peptide molecules. Dr. Harini Mohanram and Prof. Konstantin Pervushin performed the NMR experiments. Haopeng Li and Prof. Jing Yu performed the peptide encapsulation experiments. A paper on this project is currently in preparation.

4.1. Introduction

Today, we are witnessing an unprecedented growth of interests in the development and applications of nano-scale delivery systems, with broad applications in, e.g., the food, agriculture, drug-delivery and renewable energies [33-36]. Nano-sized particles also hold great promises for applications as vaccine delivery systems with potent adjuvant activities [32].

In particular, micro/nano-encapsulation, a process that involves spontaneous self-assembly of biomolecules on the chemical or biological interfaces into enclosed "capsules"

with the size of micrometers or even nanometers, has emerged as a unique and novel field of research due to its high bioavailability [138], high stability, controlled release of active compounds [35] (e.g. lipophilic and hydrophilic vitamins [139], vaccine antigens and adjuvants [140], anti-cancer [141] and anti-microbial drugs [142], etc.), and low technological barrier for scale-up manufacturing [33-36, 137, 138, 141].

Several compounds have been reported to encapsulate with the formation of a membrane, including lipids or fatty acids, amphiphilic proteins or peptides, block copolymers and inorganic colloidal particles [37]. For example, alginate, a natural polymer extracted from seaweed, has been widely used for cell encapsulation, wound healing, drug delivery, and tissue engineering applications due to its ability to ionically cross-link in water [143-145]. Polypeptides between 25 to 40 amino acids were found to assist encapsulation of bioactive lutein via electrostatic attraction [146]. Moreover, nanocomplexes of biotinylated peptides can encapsulate DNA via self-assembly, whose use in gene delivery was being evaluated in preclinical trials [147, 148].

Coacervation is a process to form droplets spontaneously through liquid–liquid phase separation (LLPS). LLPS results in a dense phase typically rich in macromolecules, separating from the dilute phase [149-151]. Among various methods, coacervation is an important route to achieve micro/nano-encapsulation. Coacervation are more likely to occur with the natural biomolecules, such as chitosan, heparin, and polypeptides [152, 153]. While this method shows promise, the process to achieve efficient coacervation, the control of size, shape, and biocompatibility are not well studied. Furthermore, a lack of knowledge to the encapsulation mechanism hindered its application in the real-world scenarios [34, 36]. Hence, there is a driving force to unravel the molecular mechanism for coacervation

and encapsulation, to expand the study from naturally-occurred molecules to the synthetic systems, and to enable *de novo* design with a focus to achieve enhanced functionality and precise control of coacervation and encapsulation [38].

In this chapter, we investigated the molecular mechanism for coacervation and encapsulation of a *de novo* peptide, WA30. This peptide is originated from the Asian corn borer (*Ostrinia furnacalis*), a destructive pest of maize. The larvae of Asian corn borer feed on the tassel and kernel of maize at younger instars (1st to 4th) and bore into the plant by feeding on stalks at later instars (5th and 6th). (Note that Instar means a stage in the life of an arthropod between two successive molts). After six instar stages, the larvae transform into pupae within the stems of host plant, before becoming moths [154-156]. The dark-colored cuticle of a larva head functions like a "helmet", protecting the larva when it bores through the plant. A picture of *Ostrinia furnacalis* and a zoom-in view of the dark-colored head cuticle is shown in Figure 4.1.

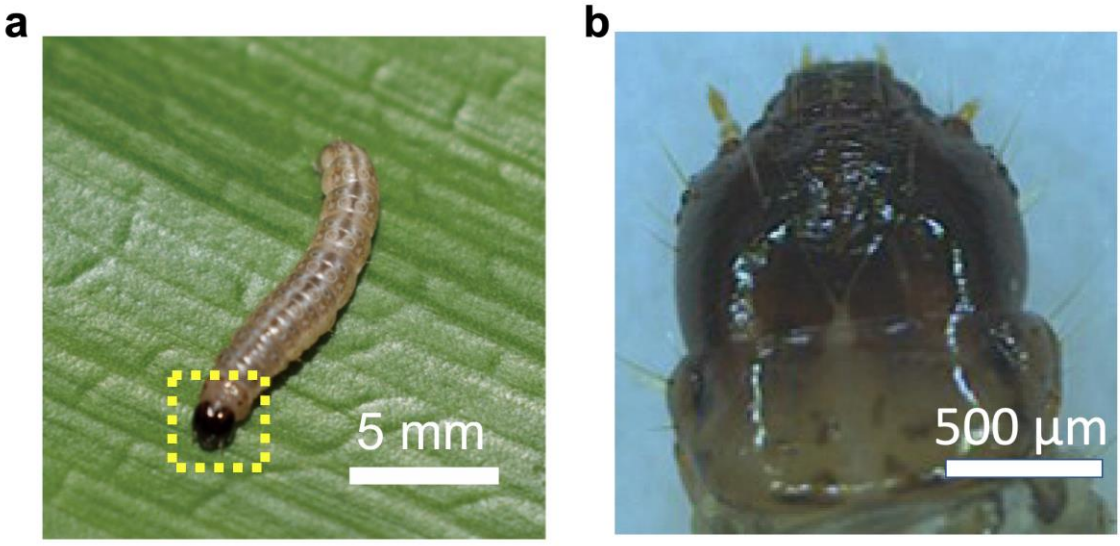

Figure 4. 1. a, Overall view of a *Ostrinia furnacalis* larva, with its head boxed in yellow; **b**, Zoom-in view showing the dark-colored, head cuticle of *O. furnacalis* larva.

Curious about the deterministic protein that enables the pressure-sustaining functionality of the larva's head cuticle, and the dynamics of its transcriptome in response to molting, RNA sequencing was conducted, and the expression level was evaluated. A total of 227 head cuticle proteins were identified. Figure 4.2 shows a heat map for the expression level of head cuticle proteins, measured between the fourth and fifth instars, the onset of larvae bore into the stem of the host plant. Due to molting, the highly expressed proteins at day 1 of the fifth instar are prone to make up the new cuticle layer. Interestingly, one highly expressed protein was found to possess a repetitive sequence (#114364209). This repetitive sequence was studied by using *de novo* synthesis to produce the repetitive peptide WA30. The sequence of WA30 can be seen in Figure 4.2c.

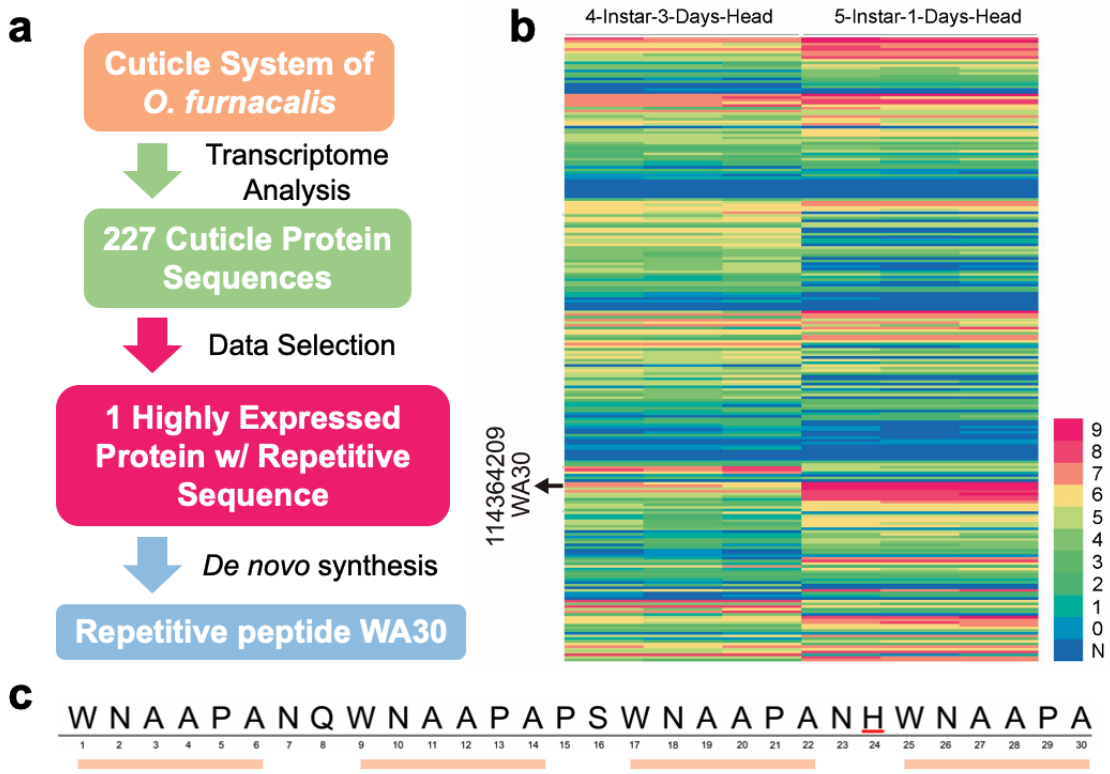

Figure 4. 2. a, Flow chart of *De novo* sequencing and screening for the protein of interest; **b**, Heatmap of protein abundance differences in the head cuticle of *Ostrinia furnacalis*. Proteins that were significantly altered at $q < 0.05$ were categorized. A total of 227 head cuticle proteins were identified. The expression levels of three corn borer larvae before and after the fourth molting were ranked from high to low using the rainbow color map from red (9) to blue (N). The protein 114364209 which contain 'WA30' was one of the highly expressed head cuticle protein after molting. **c**, The sequence of WA30 peptide. Note that the highlighted 'WNAAPA' segments are the repetitive domains.

As the name suggests, WA30 consists of 30 amino acids, including four segments of repeating amino acids (WNAAPA). Each segment, WNAAPA, consists of both hydrophobic and hydrophilic amino acids. Three spacers, each with 2 hydrophilic amino acids, were inserted intentionally between two repeating segments of WNAAPA, with a focus to enhance the solubility of WA30 in water. In-solution NMR was then conducted to determine its molecular structure in solution, prior to encapsulation. Two helical regions were identified from the NMR measurement. The NMR structure was later used as an input for MD simulations.

Although solvable in water, WA30 is insolvable in acetone. Encapsulation of WA30 peptides into hollow spheres was observed by flushing adequate amount of acetone into WA30 water solution. The process to manufacture WA30-based hollow spheres is shown in Figure 4.3a. The mean diameter of hollow spheres is around 700 nm. The mean thickness of the sphere membrane is around 70 nm, about 1/10 of the mean diameter. AFM and TEM images of the encapsulated spheres can be seen in Figure 4.3b,c. Thioflavin T (ThT) fluorescence of WA30-based hollow spheres indicated the β-sheet has formed during the process of hollow sphere formation (Figure 4.4).

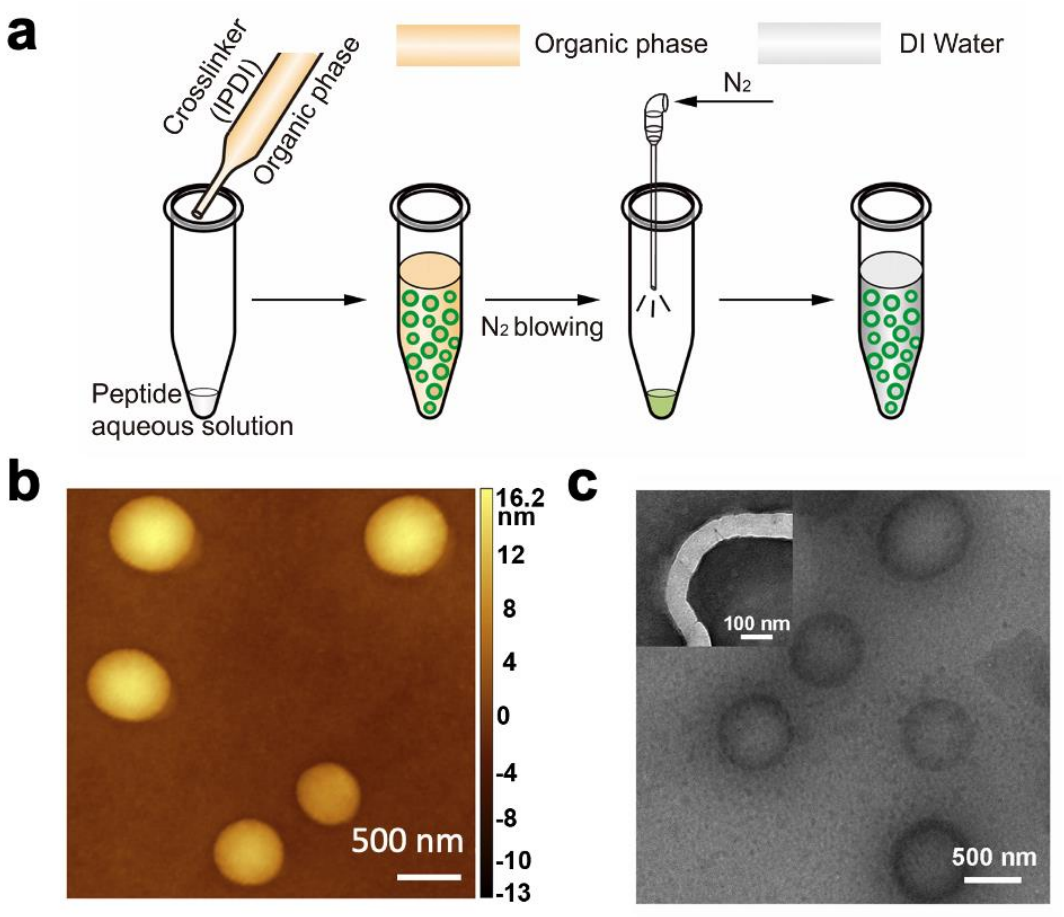

Figure 4. 3. a, Flow chart of preparation peptide-based hollow spheres; After repeated mixing, the crosslinking agent IPDI and acetone were quickly added to the high concentration peptide aqueous solution. After 6 hours of standing crosslinking, the organic solvent was volatilization accelerating by blowing nitrogen to obtain peptide-based hollow sphere aggregation. The vesicles dispersion could be obtained again by adding water; **b**, AFM of WA30 encapsulated hollow spheres; **c**, TEM of WA30 encapsulated hollow spheres, inset: zoom-in view showing the cross-section of WA30 encapsulated hollow sphere.

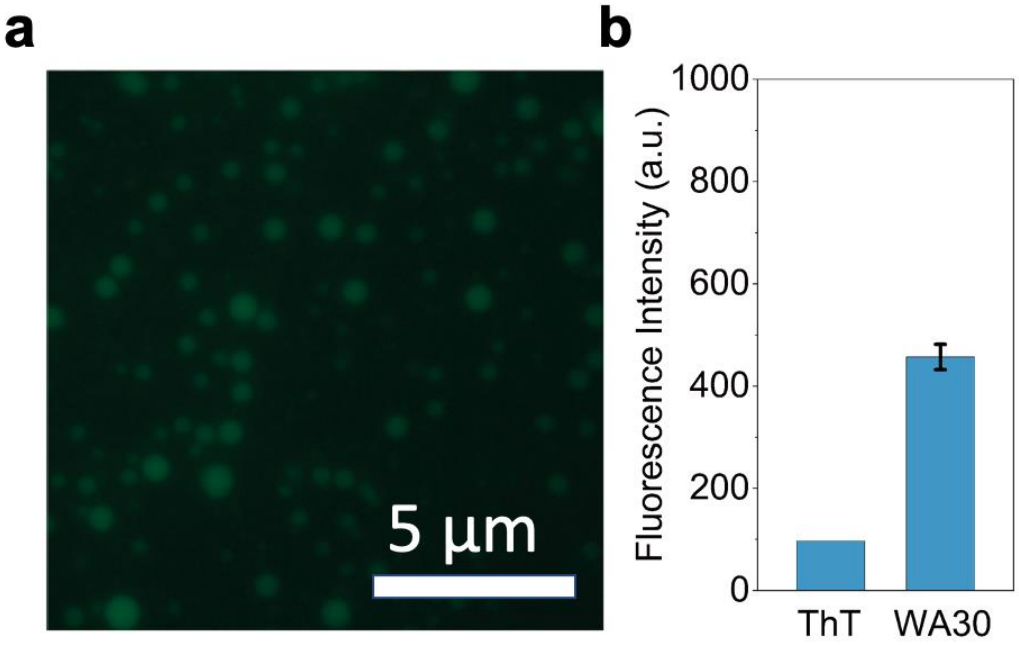

Figure 4. 4. a, Thioflavin T (ThT) fluorescence of peptide-based hollow spheres assembled by WA30; **b**, The dependence of Thioflavin T (ThT) fluorescence intensity with the formation of the WA30-based vesicles. All samples were excited at 450 nm and the emission at 482 nm was measured. The addition of peptide-based vesicles to 50mM ThT solution significantly enhanced the fluorescence intensity. By comparison, the peptide aqueous solution hardly affected the emission intensity of ThT. The fluorescence signal caused the increase mainly came from ThT combined with peptide spheres (left), indicated the β-sheet has formed during the process of forming hollow spheres.

To probe the ideal condition for WA30 encapsulation, a broad range of acetone-water volume ratios were tested, and a phase diagram was plotted (Figure 4.5a). Typically, WA30 can form hollow spheres when the volume ratio (Acetone/Water) exceeds 7:1. FTIR experiments was conducted to determine the evolution of peptide secondary structures corresponding to each volume ratio. We found that the encapsulation of WA30 was accompanied by a significant increase in the composition of β-sheet and a decrease in the composition of all other secondary structures (Figure 4.5b).

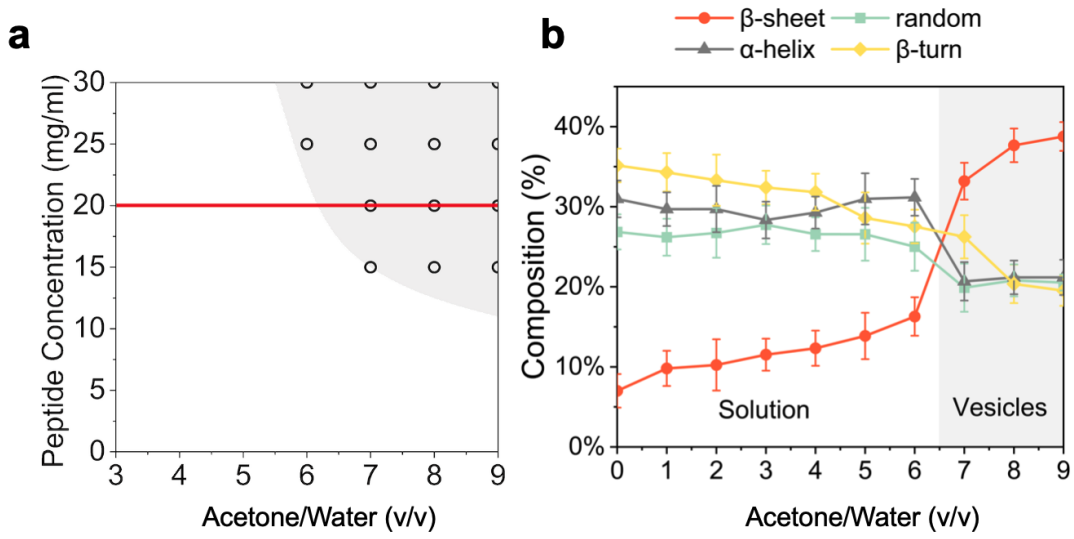

Figure 4. 5. a, Phase diagram of peptide in acetone/water mixtures. Peptide is soluble in blank zone and assemblies into vesicles in the filled zone; **b**, Change of secondary structure with increasing acetone proportion. All composition data were obtained by fitting the attenuated total reflection Fourier transform infrared spectroscopy absorption in the amide I peak located at 1600 cm^{-1} to 1700 cm^{-1}. The peptide concentration was 20 mg mL^{-1}, which has been marked with a horizontal solid red line in (**a**).

To pinpoint the molecular mechanism for coacervation and encapsulation, we first performed MD simulation of a single WA30 in water and compared it with the NMR results. Next, we augmented the simulation system to study the behavior of multi-peptide interaction. The simulation demonstrated that WA-30 peptides could self-assemble into a coacervate along a fixed direction. We investigated the underlying molecular mechanisms and the driving forces for WA30 self-assembly by looking into MD trajectories, secondary structures, number of H-bonds, RMSD and RMSF. We wrapped up this chapter with a MD simulation of water-acetone mixing, which is the key to WA30 encapsulation process, and provided a hypothesis to the encapsulation mechanism. A paper on this project is currently in preparation.

4.2. Atomistic simulations

4.2.1. Simulation model and methodology

All-atom MD simulations based on the GROMACS package (version 2018.2) were performed to investigate peptide coacervation and water-acetone mixing [59, 60]. For peptide simulations, WA30 peptides were modelled with the AMBER 99SB-ILDN force field [157]. The pdb2gmx command in GROMACS was used to add hydrogens, cap the terminal residues, and generate the topology files. TIP3P water model was used to model water molecules as recommended by the AMBER force field [158, 159]. For single peptide simulation, an open-source program was used to automatically create a solvation shell of water molecules with a thickness of 5A around the peptide molecule (http://www.mpibpc.mpg.de/grubmueller/solvate). 1 nm padding distance was set around the generated solvation shell to prevent the peptide molecule from interacting with its periodic images. More water molecules were added randomly to fill the gap. In total, 6411 water molecules were added, and the total number of atoms in the simulation box was 19651. The molar concentration of WA30 in water was 8.53 mmol/L (equivalent to the mass concentration of 26.78 mg mL^{-1}). This is within the same range of concentration as used in experiments (10~30 mg mL^{-1}). Basic protocols for simulation were the same as described in section 2.2.1 and 3.2.1.1. Multi-step energy minimization (EM) and equilibration was used to minimize disturbance to the peptide structure [160]. A test run of 10 ns was followed by a production simulation of 500 ns. Both were performed in the NPT ensemble with the Parrinello-Rahman pressure coupling and V-rescale temperature coupling method [161-163]. For eight-peptides simulation, eight single-peptide simulation

boxes were stacked into a larger cell, with a total volume of 1588.29 nm^3 and molar concentration of 8.36 mmol/L. Same EM and equilibration protocols as the single-peptide simulation were used here. However, due to the limit of computational resources, we could only conduct a 100-ns-long production simulation at a time. The interactions among peptide chains and with the system were monitored by root mean square deviation (RMSD), root mean square fluctuation (RMSF), number of H-bonds and Surfactant Accessible Surface Area (SASA), etc., using the relevant GROMACS commands. In the water-acetone mixing simulation, GAFF potential [164] was used to model the acetone molecules, and water molecules were modelled by a simple point-charge SPC/E model with polarization correction [70]. VMD was used to visualize the molecular structure of WA30 and the biphasic mixing system [74]. New cartoon representation was used to visualize the secondary structures of WA30 peptide. The side chains were depicted as thickened licorices in Figure 4.14-4.16 and 4.18. The single-letter code and color for corresponding secondary structures are: T, peacock, hydrogen bonded turn; E, light yellow, extended strand in parallel and/or anti-parallel β-sheet conformation.; B, dark yellow, residue in isolated β-bridge (single pair β-sheet hydrogen bond formation); H, magenta, α-helix; G, blue, 3_{10} helix; I, red, π-helix; C, white, random coil.

4.2.2. Validify of MD model by comparing with NMR.

Figure 4.2c shows the amino acid sequence of WA30 peptide. In total, there are 4 repeating domains with sequence of WNAAPA. Between them, there are three different spacers, each consists of two amino acids, to assist the solubility of the peptide in water while bringing in possibilities of folding into various secondary structures. W, or

Tryptophan, is a highly hydrophobic amino acid due to its aromatic side chain. However, the hydrophobicity of WA30 is reduced by the neighboring hydrophilic asparagine (N) and proline (P) amino acids. Overall, WA30 is solvable in water, which enables our collaborator to conduct in-solution NMR experiments.

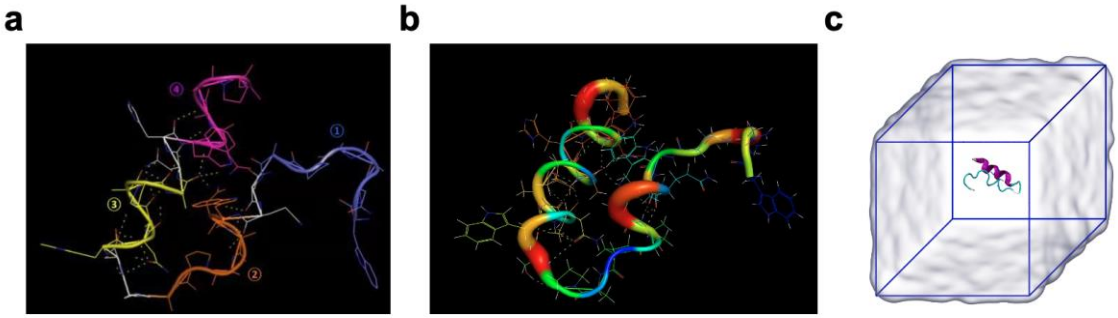

Figure 4. 6. a, NMR structure of WA30; **b**, B-factor representation of C-alpha atoms on the backbone of WA30; **c**, MD simulation setup with a single WA30 in water, the molecular structure of WA30 was taken from the NMR structure.

Figure 4.6a shows the NMR structure of WA30 in an aqueous solution. Figure 4.6b shows the representation of B-factor, a.k.a. Debye-Waller factor [165, 166], of WA30 backbone atoms. B-factor is a measure of the vibrational energy of a structure or structure component. [167] In protein structures obtained by NMR, each atom in the structure has a recorded B-factor, and (generally) atoms with a low B-factor correspond to relatively rigid portions of the structure, and *vice versa*.[168, 169] Generally speaking, the backbone atoms located near both termini and on the central spacer (PS) are flexible, while the backbone atoms in helical domains are relatively rigid. We import the NMR measured structure into a simulation box using the methods as described in 4.2.1, the equilibrated configuration is shown in Figure 4.6c. A 500-ns-long simulation was run, and the simulated structure was

compared with NMR to test the validity of simulation model. Details on the comparison of results are discussed in the following section.

4.2.2.1.MD configurations of WA30 peptide in the long simulation

To start with, we conducted a 500 ns MD simulation of a single WA30 peptide in water. Two typical indicators for protein folding/unfolding, the radius of gyration (Rg) and the solvent accessible surface area (SASA), were evaluated. If a protein is stably folded, it will likely maintain a steady value of Rg and SASA; If a protein unfolds, its Rg and SASA will vary over time. As shown in Figure 4.7, the total radius of gyration for WA30 peptide fluctuated around the initial value of 9 Å, without many changes. Similarly, SASA of WA30 maintained a steady value around 26.3 nm^2 (Figure 4.7).

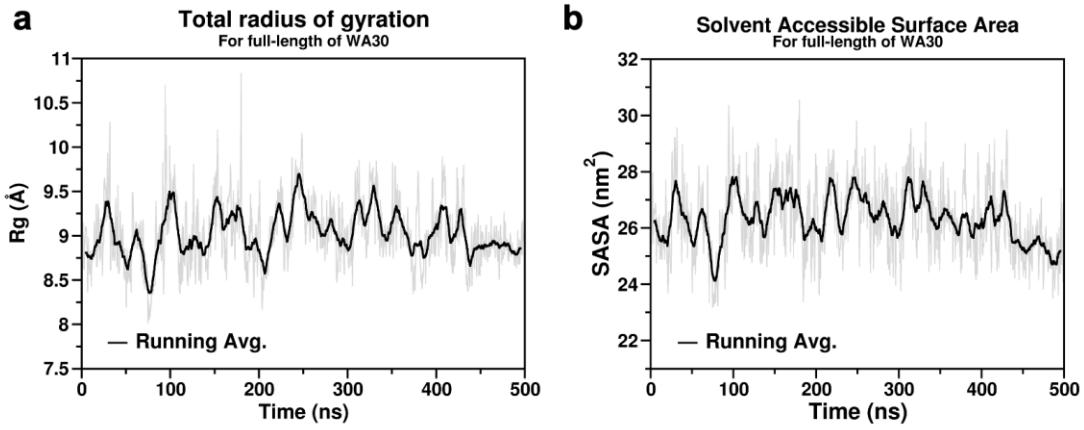

Figure 4. 7. a, Evolution of total radius of gyration (Rg) for the full-length of WA30 peptide; **b**, Evolution of solvent accessible surface area (SASA) for the full length of WA30 peptide.

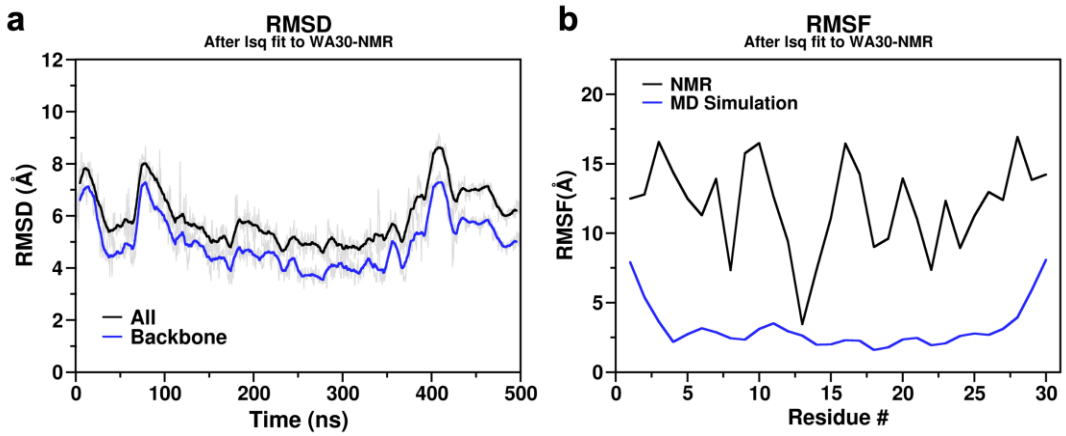

Figure 4. 8. a, Root-mean-square-deviation (RMSD) for all atoms (black) and backbone-only atoms (blue) of the simulated WA30, after least-square-fit to the NMR structure; **b**, Root-mean-square-fluctuation (RMSF) of WA30 C-alpha atoms for NMR (black) and MD simulation (blue), after least-square-fit to the NMR structure.

Figure 4.8a showed the root-mean-square-deviation (RMSD) of all atoms and backbone-only on the simulated WA30 peptide, after least-square-fit to the NMR structure. We found that in all cases, the RMSD were less than 1 nm. Focal increases of RMSD were observed at 17.5 ns, 82.5 ns and 415.5 ns. The average value of all-atom RMSD was 5.97 Å, and the average RMSD for backbone atoms was 4.98 Å, suggesting no sign of severe structural distortion. We also analyzed the root-mean-square-fluctuation (RMSF) of C-alpha atoms on the backbone of WA30 peptide. As shown in Figure 4.8b, the termini atoms exhibited relatively large RMSF of up to 8 Å. The average RMSF of C-alpha atoms in MD simulation was 3.15 Å, smaller than the RMSF calculated from NMR, which is given by the following equation:

$$RMSF_{NMR} = \sqrt{\frac{3B}{8\rho^2}}$$

Where the letter ***B*** stands for B-factor. The average RMSF calculated from B factor is 12.06 Å. In the following sections, we found the interaction between different WA30 peptides might explain the deviation here.

4.2.2.2.Evolution of WA30 peptide's Secondary Structures

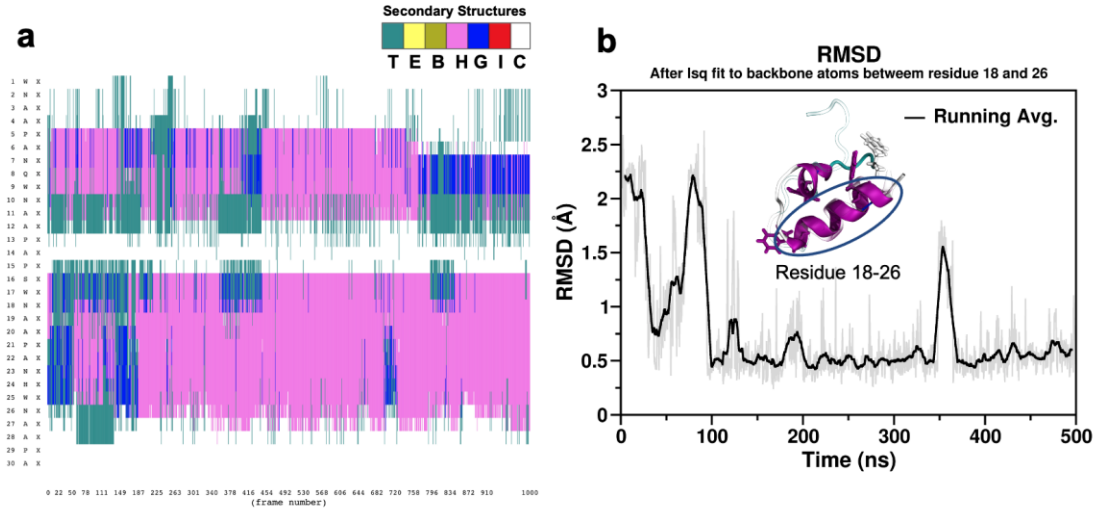

Figure 4. 9. a, Evolution of the secondary structures for WA30 peptide. Note that the horizontal axis is the frame number, which is equal to 2 times the simulated time. The single-letter and color codes on the top right corner stand for the corresponding secondary structures: T, peacock, hydrogen bonded turn; E, light yellow, extended strand in parallel and/or anti-parallel β-sheet conformation.; B, dark yellow, residue in isolated β-bridge (single pair β-sheet hydrogen bond formation); H, magenta, α-helix; G, blue, 3_{10} helix; I, red, π-helix; C, white, random coil. **b**, RMSD for backbone atoms of the simulated WA30 between residue 18 and 26, after least-square-fit to residue 18 and 26 of the NMR structure. Inset: the final snapshot taken at 500 ns of MD simulation; the circle indicates residue 18 to 26 of WA30 peptide.

The evolution of WA30 secondary structures was plotted against the frame number (simulated time*2) in Figure 4.9a. Its vertical axis corresponds to the residue number of amino acids, and color blocks represent segments of peptide with same secondary

structures. We found that the secondary structure of WA30 underwent negligible changes. At 329 ns (frame #758), the α-helix between residue 5 and 9 changed into 3_{10} helix and remained unchanged. We also assessed the RMSD of the α-helix between residue 18 and 26, as shown in Figure 4.9b. The RMSD was measured by least square fitting the MD trajectory to the backbone atoms between residue 18 and 26 from NMR structure. RMSD fluctuated near an initial value of 2 Å until 100 ns, when it reached a plateau with an average of 0.5 Å. At 355 ns, RMSD increased to 1.5 Å but quickly decreased back to 0.51 Å. After 375 ns, RMSD maintained a steady value of 0.5 Å. Hence, the 500-ns-long simulation proved that the MD model could accurately reproduced the secondary structures and dynamic features (fluctuation) of WA30 peptide in solution, thereby confirming the validity of the simulation model.

4.2.3. Multiple peptides can coacervate in water.

We augmented the system by stacking the single-peptide simulation box into a 2x2x2 fashion, using the corresponding command in GROMACS (**gmx nbox**). A total of eight WA30 peptide chains were placed in the augmented simulation box (Figure 4.10). Periodic boundary conditions in x, y and z directions still applied in the augmented MD simulation model.

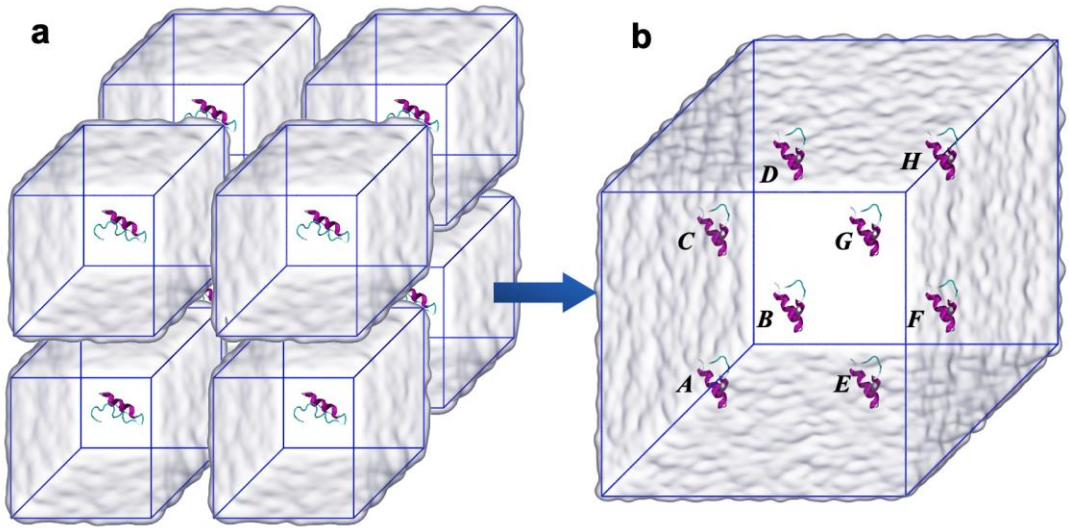

Figure 4. 10. Illustrations showing the augmentation of MD simulation model, **a**, eight simulation cells, each containing a single WA30 peptide, were stacked into a 2x2x2 fashion; **b**, The augmented MD model containing eight WA30 peptides, namely, chain A, B, C, D, E, F, G, and H.

After EM, equilibration, and test run for 10 ns, we found that three peptide chains (A, B, E) already self-assembled into a trimer, as shown in Figure 4.11. Three peptides assembled along an assembly direction. It is especially clear when looking at both front view and side view of the trimer: the assembly appeared to be loose and elongated in the front view, while being dense and compact in the side view. Moreover, the secondary structures of peptide chains in the trimer remained unchanged, and that peptide chains appeared to interact with each other via the flexible secondary structure such as random coils and hydrogen turns.

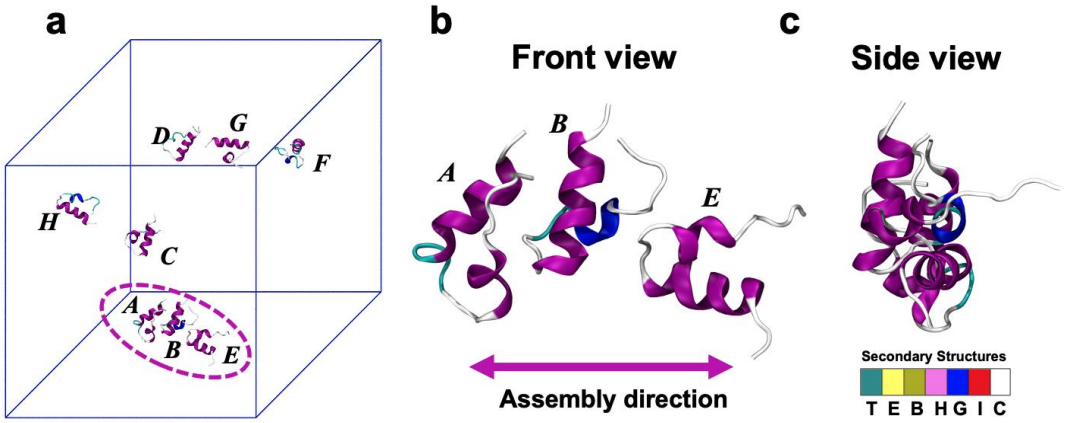

Figure 4. 11. a, MD configuration showing three WA30 peptides, chain A, B and E (circled in purple), self-assembled into a trimer. **b**, The front view of the trimer. It appears that WA30 peptides prefer to assemble along the direction as indicated by the purple arrows. **c**, The side view of the trimer. Secondary structures are indicated by the same color and single-letter codes as in Figure 36. Water molecules are not displayed for clarity.

The pre-assembled MD configuration was used as an input for an additional 100-ns-long MD simulation. Towards the end of 100-ns-long simulation, we found that all eight peptides self-assembled into a stable, rod-like octamer, 8 nm in length, 4 nm in width, and 3 nm in thickness. A graphic illustration of the final configuration was shown in Figure 4.12. Apparently, the peptides self-assembled along a fixed direction. Although new secondary structures emerged after self-assembly, we found most helical structures were well-preserved. The octamer appeared to be stable once formed, at least within the simulated time scale (10^1~10^2 ns). Similar to what is observed in Figure 4.11, peptides appeared to interact with their neighboring chains via the flexible coils and turns.

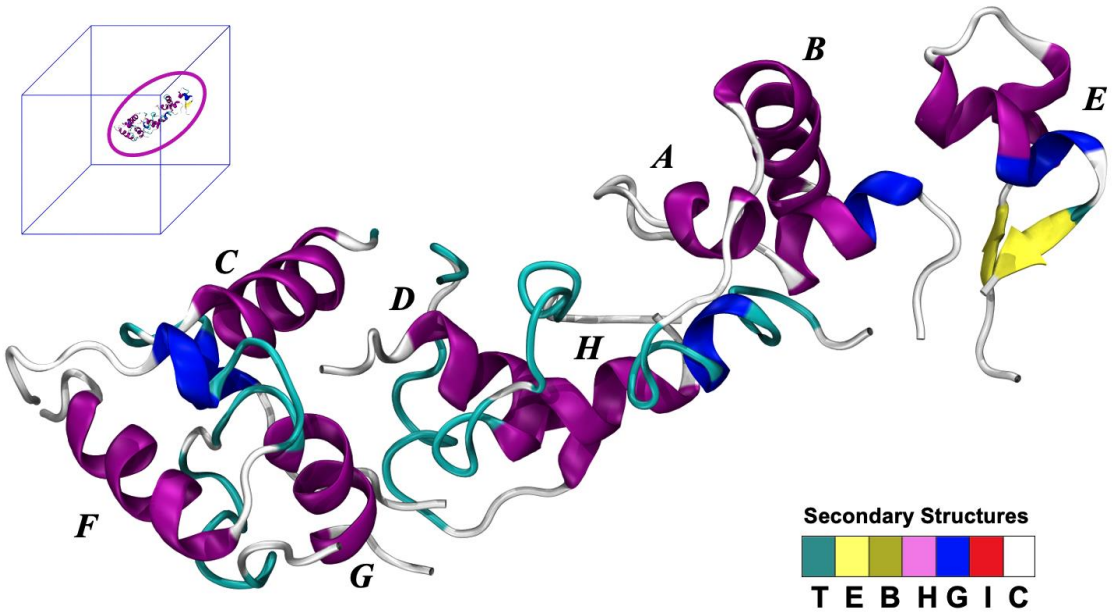

Figure 4. 12. The final configuration of 100-ns-long simulation shows directional self-assembly of WA30 peptides into an octamer. Top left corner shows the location of the octamer (circled in purple) in the simulation cell. Secondary structures are indicated by the same color and single-letter codes as in Figure 4.9. Water molecules are not displayed for clarity.

4.2.3.1.Peptide coacervation with negligible change of secondary structures

We analyzed the evolution of secondary structures for all peptide chains by plotting them against the frame number (simulated time*2), as shown in Figure 4.13. In the vertical axis, the first column represents the sequential number of amino acids, the second column stands for the single-letter-code of amino acids, and the third code represents the name of peptide chains. We found that chain B, C, D and F had negligible changes to their secondary structures. Chain G and H lost their α-helix secondary structure between residue 5 and 11, while maintaining the α-helix between residue 18 and 26 intact. Chain A lost its α-helix secondary structure between residue 18 and 26, while maintaining the α-helix between residue 5 and 11 intact. Chain E formed β-sheet secondary structure within itself,

near the flexible C-terminal and N-terminal (residue 4 & 5, residue 27 & 28). While the simulation and the secondary structures analysis revealed the overall behavior of WA30 peptides' self-assembly and coacervation in water, detailed analysis on the full structure of peptides (including the side chains) is crucial to the understanding of molecular mechanisms for peptide coacervation, and possibly, encapsulation.

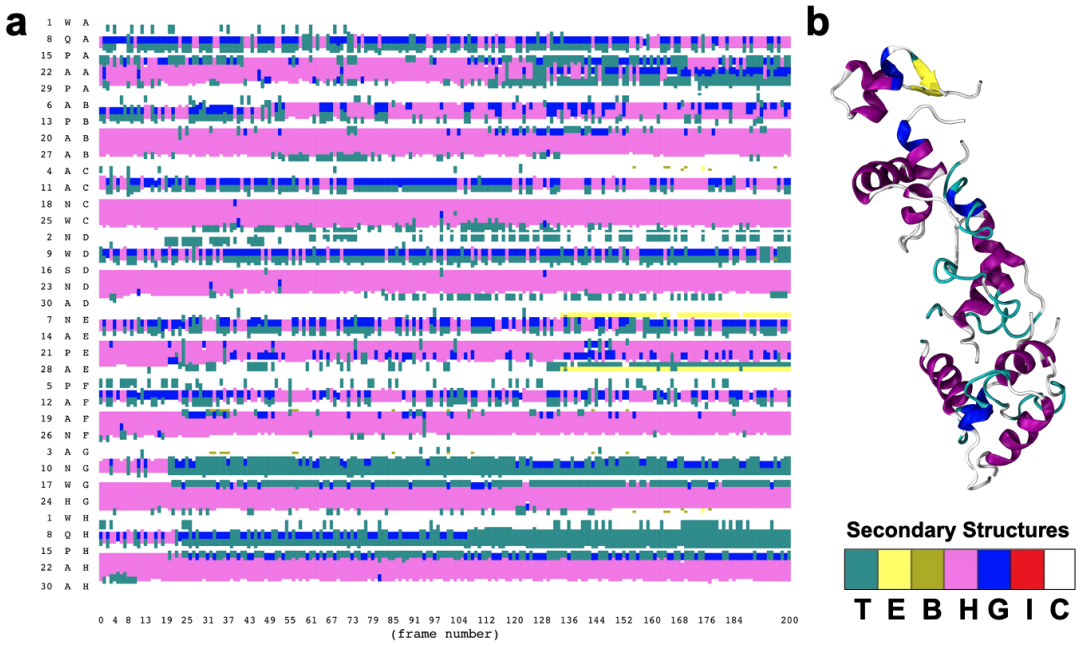

Figure 4. 13. a, Evolution of the secondary structures for all eight WA30 peptides. Note that the horizontal axis stands for the frame number, which is equal to 2 times the simulated time. The vertical axis stands for the number and name of amino acids (first two columns), as well as the name of the peptide chain (the last column). **b**, The MD snapshot of WA30 peptides self-assembled into an octamer, taken at 100 ns. Secondary structures are indicated by the same color and single-letter codes as in Figure 4.7. Water molecules are not displayed for clarity.

4.2.3.2.Persistent β-sheet formation during peptide coacervation

To understand the molecular mechanisms for peptide coacervation, we studied the β-sheet formation by extracting the traces of persistent β-sheet formation from the secondary structure graph, and pinpointed the relevant molecular configurations from the MD trajectories. In Figure 4.14, zoom-in view of chain G and chain F showed the formation of an isolated β-bridge, i.e., single pair of amino acid aligned in a way to form a coupled 'bridge'. The isolated β-bridge was formed between residue 3 Alanine on chain G and residue 15 Proline on chain F, from 16 ns till 76.5 ns. Another example of isolated β-bridge, formed between residue 2 Asparagine on chain C and residue 28 Alanine on chain G, is shown in Figure 4.15. At 87.5 ns, residue 3 Alanine on chain C and residue 27 Alanine on chain G joined in with the existing β-bridge to form an extended β-sheet, which required at least 2 pairs of residues. However, the lifetime was shorter than the isolated β-bridge between chain G and F. After 88.5 ns, no isolated β-bridge or extended β-sheet was observed between chain C and G.

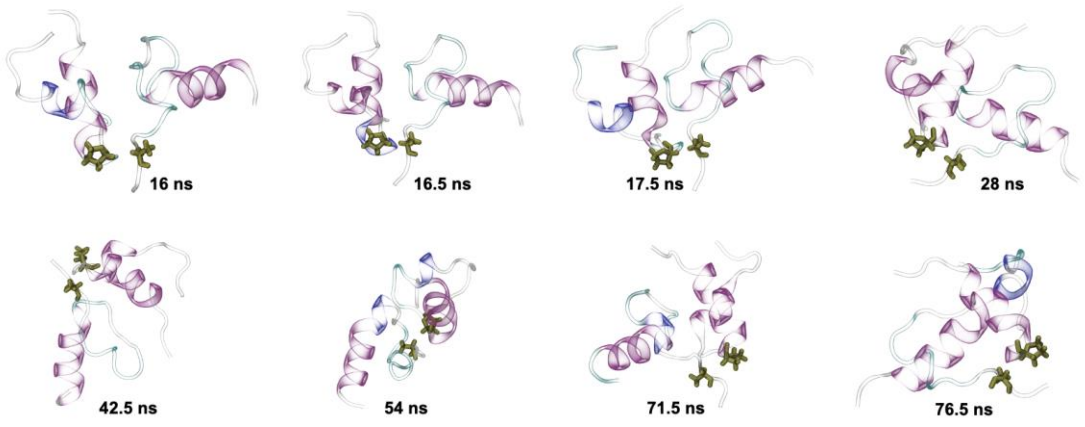

Figure 4. 14. Zoom-in view of chain G and chain F showing the representative snapshots of an isolated β-bridge. Residues in the isolated β-bridge, residue 3 Alanine on chain G and

residue 15 Proline on chain F, are depicted as dark yellow, thickened licorices. Secondary structures are indicated by the same color and single-letter codes as in Figure 4.9. Water molecules are not displayed for clarity.

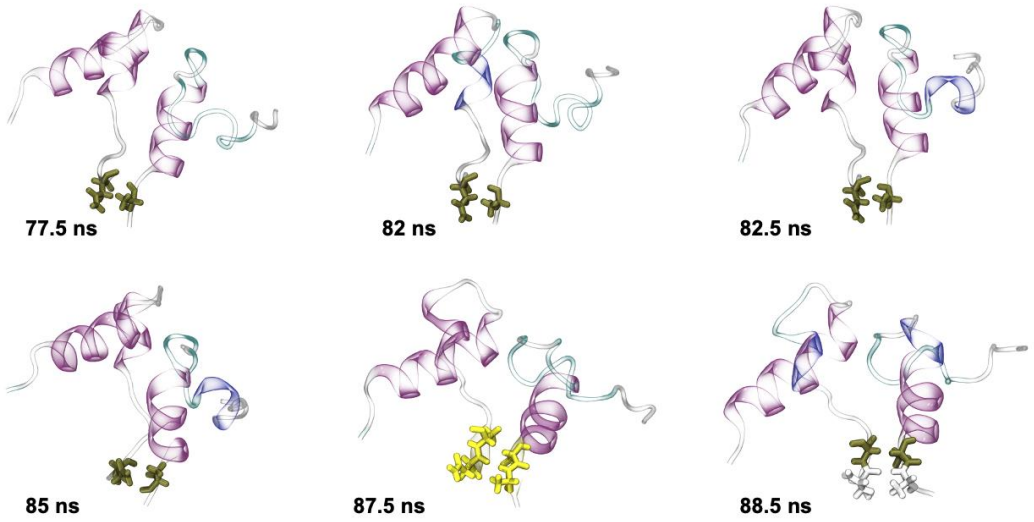

Figure 4. 15. Zoom-in view of chain C and chain G showing the representative snapshots of an isolated β-bridge. Residues in the isolated β-bridge, residue 2 Asparagine on chain G and residue 28 Alanine on chain G, are depicted as dark yellow, thickened licorices. At 87.5 ns, residue 3 Alanine on chain C and residue 27 Alanine on chain G joined in with the existing β-bridge to form an extended β-sheet, depicted as bright yellow, thickened licorices. Secondary structures are indicated by the same color and single-letter codes as in Figure 4.9. Water molecules are not displayed for clarity.

Apart from intermolecular β-sheet structure, we also observed β-sheet within a peptide chain itself. Figure 4.16 shows the formation of intramolecular β-sheet in chain E, between residue 4 Alanine & residue 5 Proline, and residue 27 Alanine & residue 28 Alanine. This β-sheet appeared to be stable and persistent, initially observed at 67 ns, and survived till the end of 100-ns-long MD simulation. Although the percentage of β-sheet among all secondary structures was small, our experimental collaborators were still able to identify the existence of β-sheet in peptide solution (Figure 4.5) via FTIR experiment.

Hence, we conclude that the self-assembly of WA30 peptides was accompanied by the formation of persistent, short β-sheet at the flexible domains (both termini and the central spacer PS) of WA30 peptide.

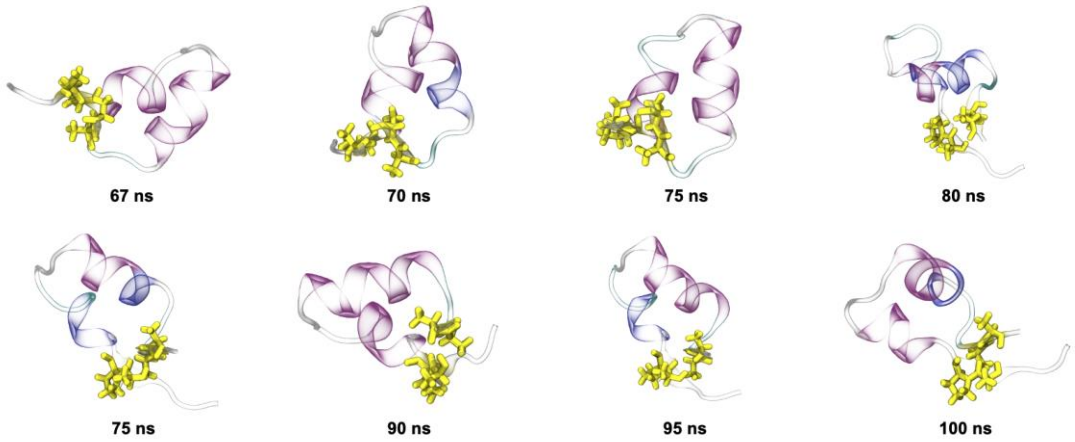

Figure 4. 16. Zoom-in view of chain E showing the representative snapshots of an extended β-sheet. Residues in the extended β-bridge, #4 Alanine, #5 Proline, #27 Alanine and #28 Alanine, are depicted as bright yellow, thickened licorices. Secondary structures are indicated by the same color and single-letter codes as in Figure 4.9. Water molecules are not displayed for clarity.

4.2.3.3.Driving force for peptide coacervation

To better understand the driving force for peptide coacervation, two indicators were evaluated: (1) the total potential energy of eight WA30 system, and (2) SASA for a complex of 8 WA30 peptide molecules, as shown in Figure 4.17. The total potential energy did not exhibit any noticeable changes, averaging of -2.07e+6 kJ/mol. SASA for eight peptide chains, however, exhibited a continuous decrease from 195 nm^2 at 0 ns to 141.8 nm^2 at 55 ns. After 55 ns, SASA levelled off with an average of 139.6 nm^2. As a result, SASA decreased by nearly 23% after coacervating into an octamer, suggesting hydrophobic interaction to be one of the driving forces for peptide coacervation. Moreover, intermolecular hydrogen bonds (H-bonds) might also facilitate peptide coacervation. We will investigate these two possible driving forces in the following sections.

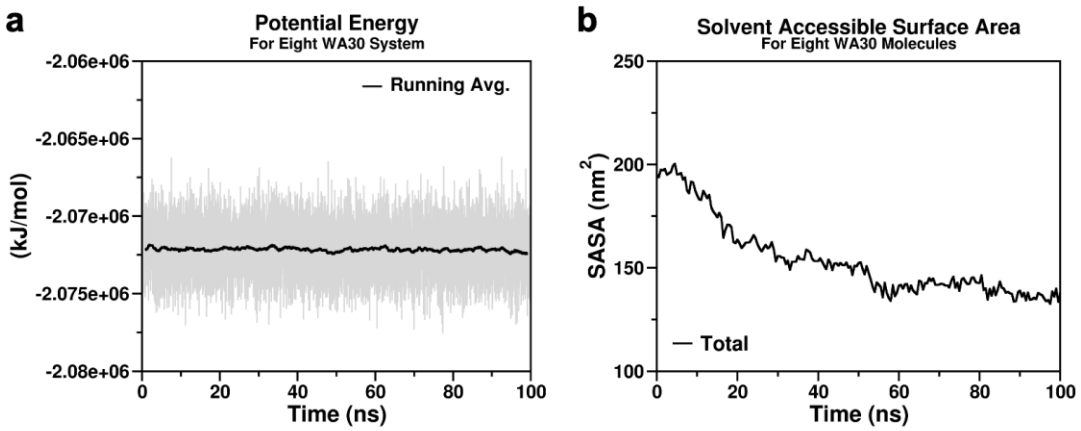

Figure 4. 17. a, Evolution of total potential energy for the eight WA30 peptides system showing negligible changes during peptide coacervation; **b**, Evolution of Solvent Accessible Surface Area (SASA) for the eight WA30 peptides system showing significant decrease until fully coacervated.

4.2.3.3.1. Hydrophobicity driven Tryptophan-stacking facilitates peptide coacervation

As mentioned in section 4.2.2, WA30 peptide consists of four highly hydrophobic Tryptophan (W) residues, while the overall hydrophobicity of the peptide is reduced by the hydrophilic Asparagine (N) and Proline (P) residues. Nevertheless, the hydrophobic side chain of W could induce high energy penalty when surrounded by water. It is energetically favorable for Tryptophan's aromatic side chains to stack on one another, so as to reduce the energy penalty. Figure 4.18 shows the simulation snapshots during the coacervation of a trimer (chain A, B, E) and a pentamer (chain F, G, C, D, H). Between 50 ns and 51.5 ns, two clusters of peptides moved towards each other without establishing any contact. At 52 ns, the W residue on chain A (blue) and on chain H (green) established initial contact. At 52.5 ns, the distance between two W residues decreased, forming a W-W stacking configuration. At 53 ns, two clusters coalesced into an octamer, with the stacking of W residues serving as docking sites. From 55 ns onwards, we observed more W-W stacking between chain A and chain H, indicated by the red circles in Figure 4.18. The stacking between W residues appeared to be stable and robust. In addition, the residues took part in W-W stacking were located on the α-helix region, which according to our calculation earlier, exhibits less fluctuation and appeared to be relatively rigid. We believed by establishing a W-W stacking, it also helped to anchor/dock the rigid α-helix structures. The flexible structures are not affected by W-W stacking, thus can explore the configurational space freely.

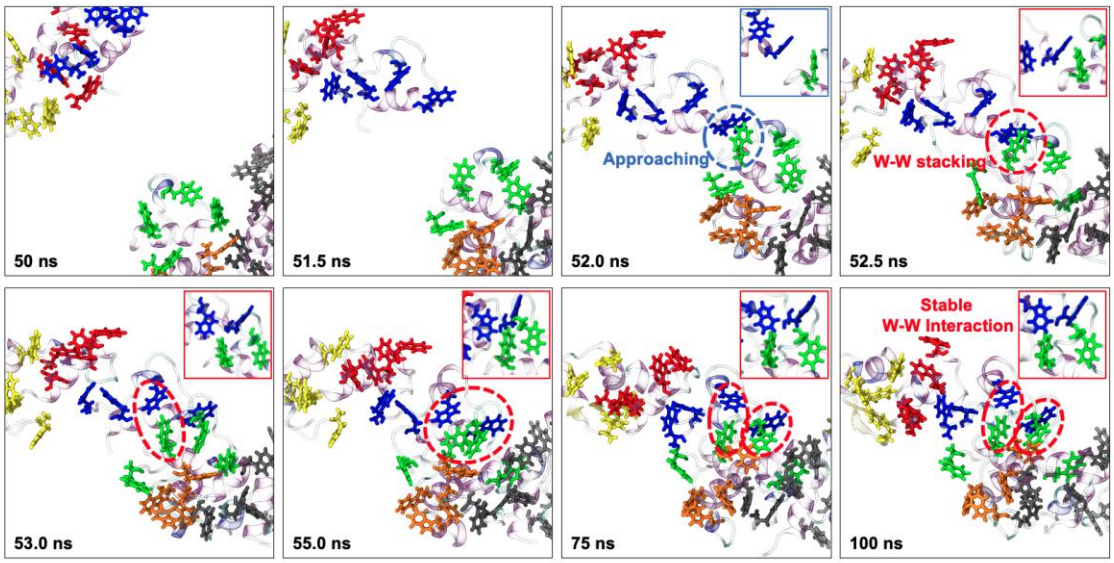

Figure 4. 18. Zoom-in view of the representative snapshots showing the coacervation of a trimer (chain A, B, E, top left) and a pentamer (chain H, D, C, G, F, bottom right). Tryptophan (W) residues are depicted as thickened licorices, the colors of W residues suggest the peptide chains they are located on. The insets, circled in blue and red on the top right corner of snapshot 52, 52.5, 55, 75 and 100 ns, show the magnified view of W-W interaction between chain A (light green) and chain H (blue). After 55 ns, the trimer and the pentamer coacervate into a stable octamer.

4.2.3.3.2. H-bond formation stabilize the assembly

Apart from hydrophobicity driven W-W stacking, intermolecular hydrogen bond (H-bond) is also a potential driving force for peptide coacervation. We calculated the number of intermolecular H-bonds between the all-peptide chains via proof by exhaustion. H-bonds were only found between those neighboring peptides in the coacervate/octamer, namely, F ⋯ G, G ⋯ C, C ⋯ D, D ⋯ H, H ⋯ A, A ⋯ B and B ⋯ E. Next, we plotted the number of H-bonds against simulation time (Figure 4.19). The increase of number of H-bonds would not occur until two peptide chains were brought together by W-W stacking. For instance, no intermolecular H-bonds were formed between chain H and chain A until 53 ns, when W-W stacking pulled chain H and chain A together. Details of the most frequent pairs of

H-bonds were listed underneath each graph, along with their percentage of occurrence. We noticed that, typically, residues located on the flexible domains (coils and turns) of WA30 tend to form intermolecular H-bonds with other peptides. The number of H-bonds between WA30 peptides and water kept decreasing during coacervation. This is because the formation of inter-peptide H-bonds gradually deplete the donors and acceptors available to form H-bonds with the surrounding water molecules. Therefore, H-bond is important in facilitating peptide coacervation.

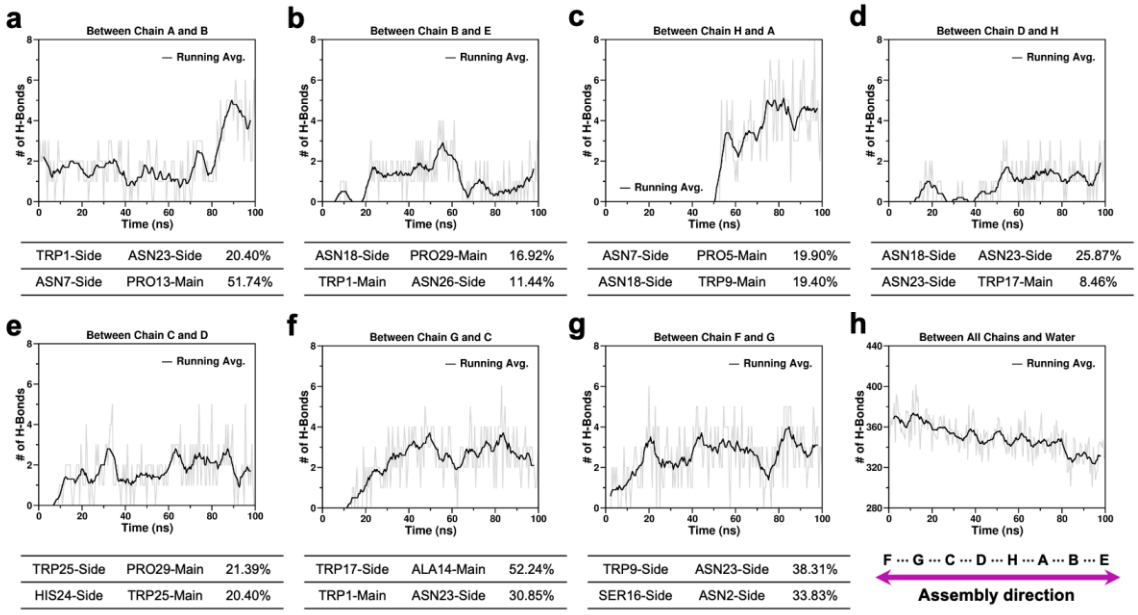

Figure 4. 19. a-g, Evolution of the number of H-bonds for each pair of neighboring peptides in the coacervate. Detailed information of the top two most frequent pairs of H-bonds and their percentage of occurrence are listed in the charts underneath the number of H-bonds graphs. Note that in each chart, the first column stands for the donor of an H-bond, the second column stands for the acceptor of an H-bond, and the third column stand for the occupancy of this H-bond in the 100-ns-long simulation; **h**, Evolution of the number of H-bonds between all WA30 peptides and water. An illustration showing the organization of peptides in the coacervate, and the self-assembly direction is placed underneath the graph.

4.2.3.4.RMSD and RMSF of WA30 during peptide coacervation

The molecular behaviors of WA30 during peptide coacervation was assessed by root-mean-square-deviation (RMSD) and root-mean-square-fluctuation (RMSF). Figure 4.20 shows the evolution of RMSD in each peptide chain. Focal increases of RMSD up to 8 nm were observed. However, these changes were not persistent, usually vanished within 10 ns. The MD trajectories revealed that such changes were associated with severe distortions on the flexible domain of WA30 peptide, after W-W stacking and during the intermolecular H-bonds formation. We also noticed that chain F and G experienced minor changes in RMSD. This is due to the following reasons: (1) chain F is located at the free end of peptide coacervate, only interacting with one neighboring peptide chain G. Thus, less distortion on chain F is expected. (2) chain G formed persistent β-sheet with chain F since the beginning of the simulation. β-sheet prevents the flexible regions of WA30 peptide from experiencing severe distortions. We also analyzed the RMSF of C-alpha atoms on the backbone of all WA30 peptide chains (Figure 4.21). RMSF for each peptide chain was one order of magnitude larger than the single peptide simulation. Apart from chain C, F, G, all other peptide chains exhibited relatively large RMSF with an average above 20 Å. In addition, the C-alpha atoms exhibiting large RMSF value are located on the flexible domains, with a higher chance to form intermolecular H-bonds with other peptides. As shown in Figure 4.21i, the average RMSF from MD simulation is consistent with the RMSF calculated from NMR B-factor. Hence, the RMSD and RMSF confirmed that the coacervation of WA30 peptides was realized by (1) W-W stacking to anchor two neighboring peptide chains, and (2) large fluctuations of flexible regions to enhance the formation of H-bonds. β-sheet formation, however, suppress the magnitude of both RMSD and RMSF.

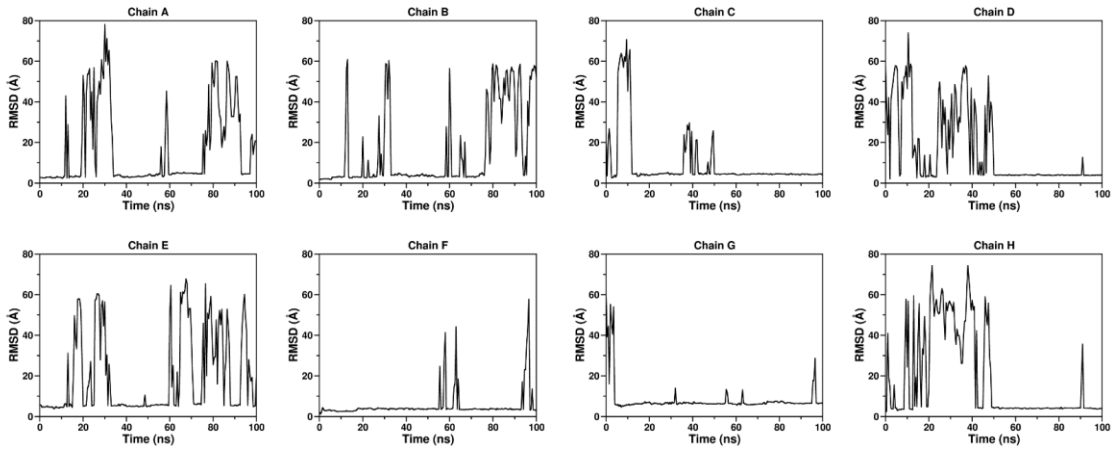

Figure 4. 20. Evolution of root-mean-square-deviation (RMSD) for each WA30 peptide in the 100-ns-long simulation. Focal changes of RMSD with magnitude up to 8 nm can be seen in chain A, B, C, D, E, and H. Chain F and G show minor changes of RMSD.

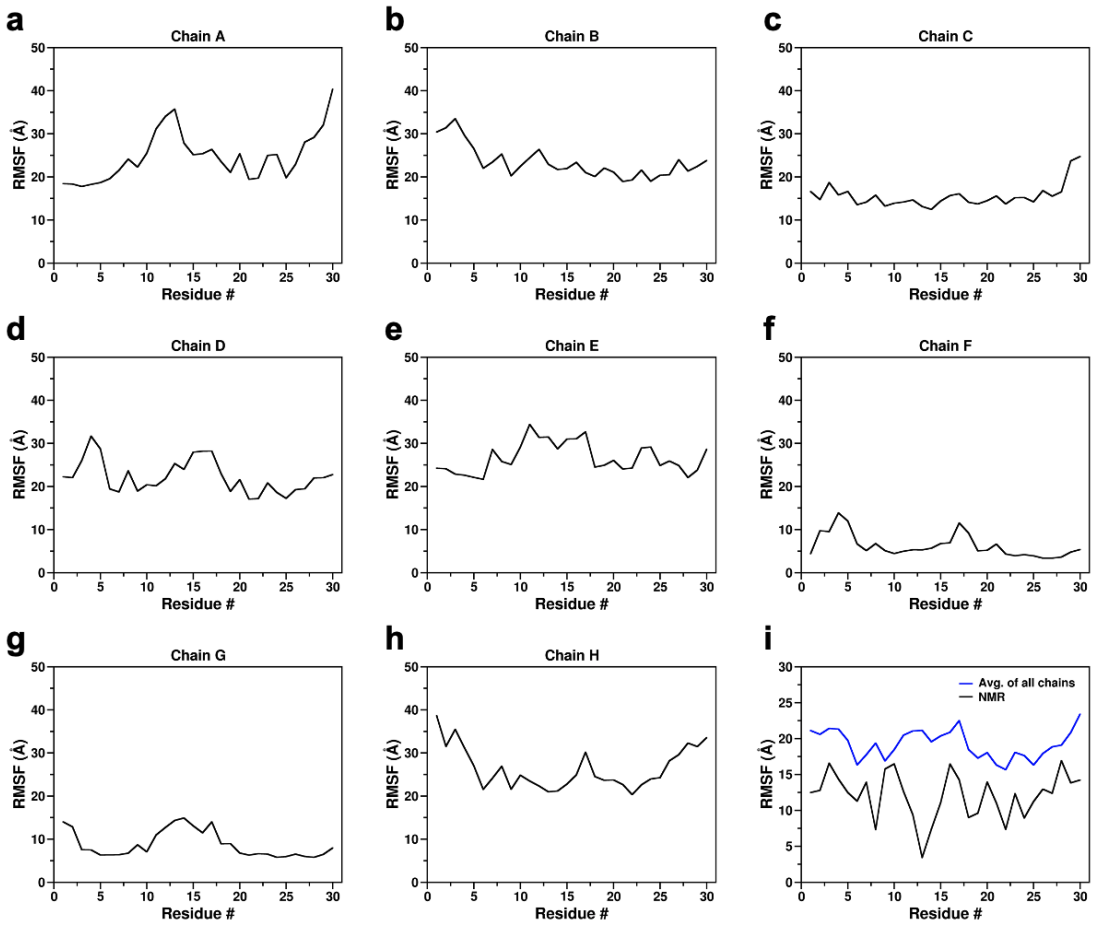

Figure 4. 21. a-h, The root-mean-square-fluctuation (RMSF) of C-alpha atoms located on the backbone of each WA30 peptide chain; **i**, the average RMSF of all peptide chains from the MD simulation (black) is consistent with the RMSF calculated from NMR B-factor (blue).

4.2.4. Mechanism for peptide encapsulation

Although solvable in water, WA30 is insolvable in acetone. Encapsulation of WA30 peptides into hollow spheres was achieved by flushing acetone into WA30 water solution (Figure 4.3a). A broad range of acetone-water volume ratios were tested to probe the ideal condition for WA30 encapsulation, and a phase diagram was plotted (Figure 4.5a). However, the molecular mechanism for peptide encapsulation is still unclear. As a first step towards understanding peptide encapsulation, we simulated a classical problem of biphasic mixing of acetone and water.

4.2.4.1.Biphasic mixing simulation of acetone and water

The acetone-water mixing is crucial to the encapsulation process of WA30 peptides. Figure 4.22a shows the biphasic mixing setup in MD simulation. The initial size of the simulation system was 10 nm in length, 5 nm in width and height. Although experiments proved that WA30 could not encapsulate into hollow spheres unless the volume ratio of Acetone to Water exceed 7:1, we choose volume ratio of 1:1 for the ease of simulation. In total, there were 951 acetone molecules and 4032 water molecules. After EM and equilibrium steps, a 30-ns-long simulation was run, and the simulated trajectory was analyzed. Figure 4.22b shows the molecular configuration by the end of the 30-ns-long simulation. Both acetone and water molecules diffused across the whole simulation box. For detailed analysis on acetone-water mixing, the horizontal axis along the longest box vector was selected to be the reaction coordinate, perpendicular to the initial acetone-water interface at t = 0 ns. Two indicators were evaluated: (1) the total potential energy, and (2) the total density of the biphasic mixing system, as shown in Figure 4.23. The total potential

energy exhibits a decrease between 0 and 5 ns, then levels off with an average of -4.20e+5 kJ/mol. The total density of the system exhibits a gradual increase between 0 and 6 ns, then plateaus with an average of -915.4 kg/m^3. The evolution of total potential energy and density suggests that biphasic mixing of acetone and water to be a rapid process.

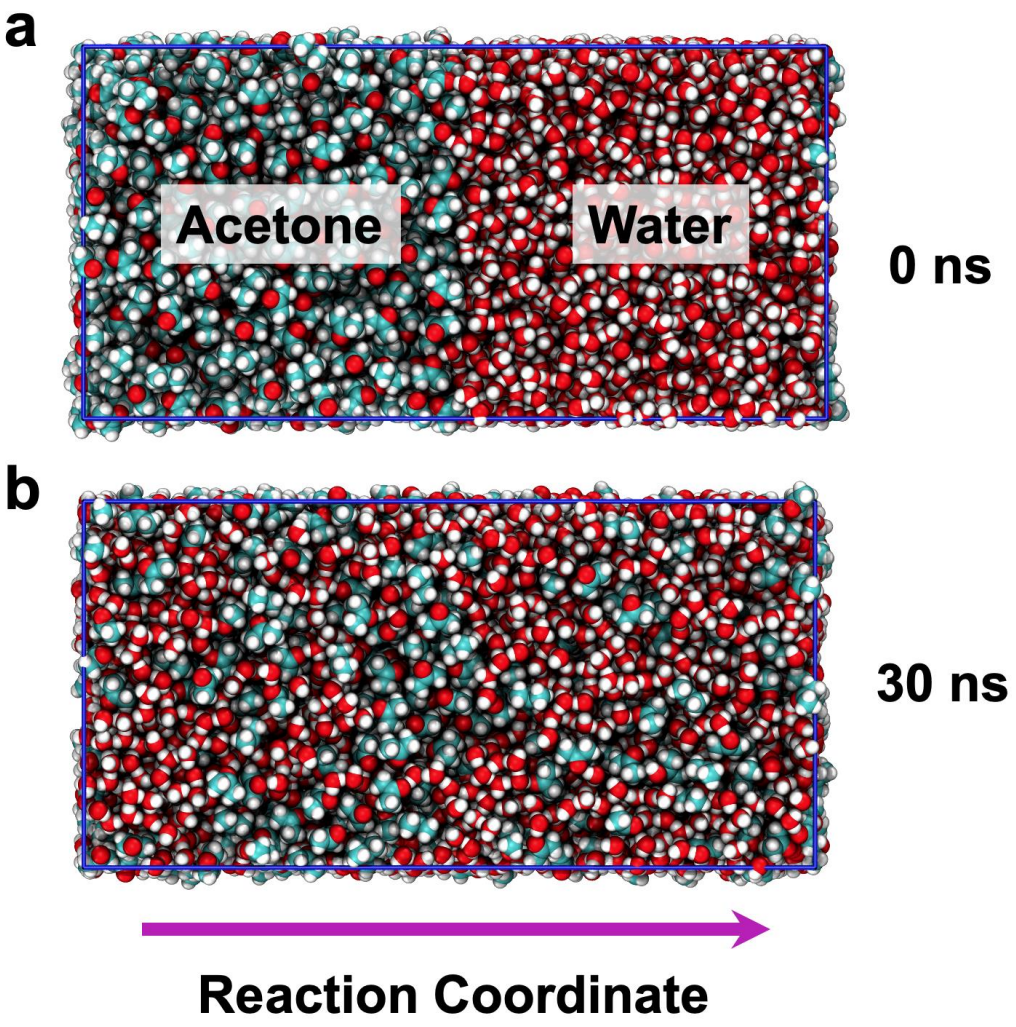

Figure 4. 22. a, The initial configuration for biphasic mixing MD simulation; **b**, the molecular configuration at the end of the 30-ns-long simulation. The reaction coordinate is indicated with a purple arrow. Atoms of acetone and water molecules are depicted as large spheres, and are colored as follows: hydrogen, white; carbon, cyan; oxygen, red.

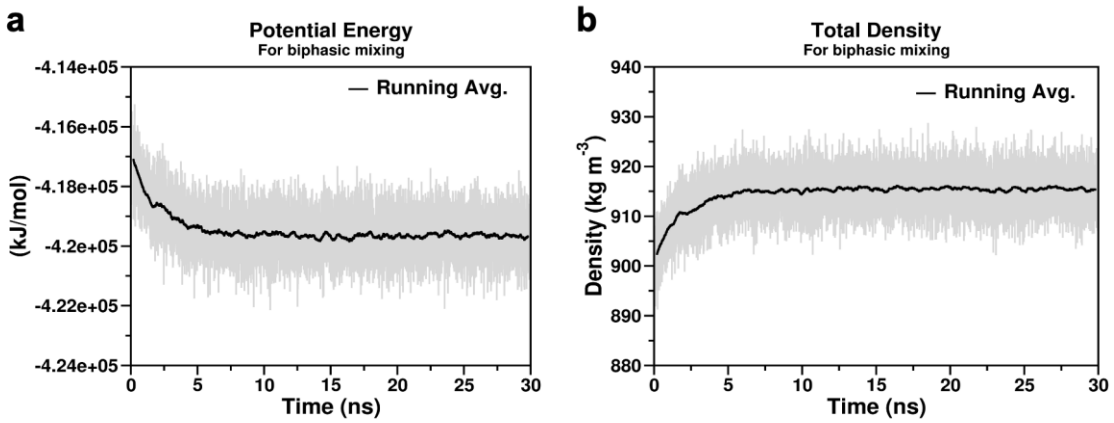

Figure 4. 23. a, Evolution of total potential energy for the biphasic mixing system showing a decrease in the first 5 ns; **b**, Evolution of total density showing an increase in the first 6 ns.

Next, we calculated the partial density of acetone, water, and the system along the reaction coordinate. As shown in Figure 4.24a, the partial density of acetone between 0 and 5 nm (the original acetone phase, at t = 0 ns) experiences a rapid decrease between 0 and 8 ns, and increases drastically between 0 and 10 ns in the original water phase between 5 and 10 nm. Similar behavior is observed in the partial density of water and the system (Figure 4.24b,c). Overall, the partial densities reached equilibrium in less than 10 ns, confirming the rapid mixing of acetone and water.

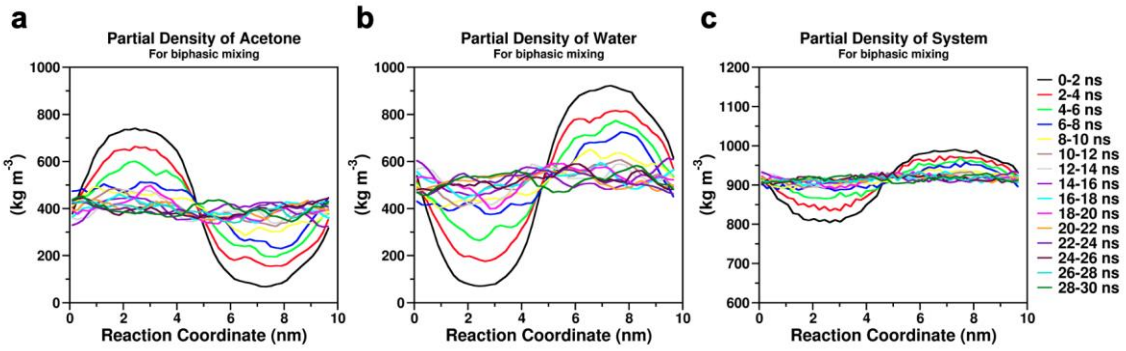

Figure 4. 24. a-c, The evolution of partial density for acetone (**a**), water (**b**), and the system (**c**) along the reaction coordinate. Partial densities were calculated based on 2 ns intervals.

We also evaluated their mean squared displacements (MSD) using GROMACS commands (gmx msd)[60, 170]. Figure 4.25 shows the evolution of MSD for water, acetone, and the system. To determine the diffusion coefficient D of acetone or water, we used the following equation [171]:

$$\lim_{t\to\infty}\left\langle \left\| \mathbf{r}_i(t) - \mathbf{r}_i(0) \right\|^2 \right\rangle_{i\in A} = 6D_A t$$

Where $\mathbf{r}_i$ is center of mass positions of the evaluated molecule A, D_A is the diffusion coefficient of molecule A. The left-hand side of the equation is the MSD for molecule A. Table 4.1 gives the calculated diffusion coefficients for acetone, water, and the system, fitted between t = 3 ns and t= 27 ns of the MSD. The diffusion coefficients fitted from MD simulation are consistent with previous experiments [172-174].

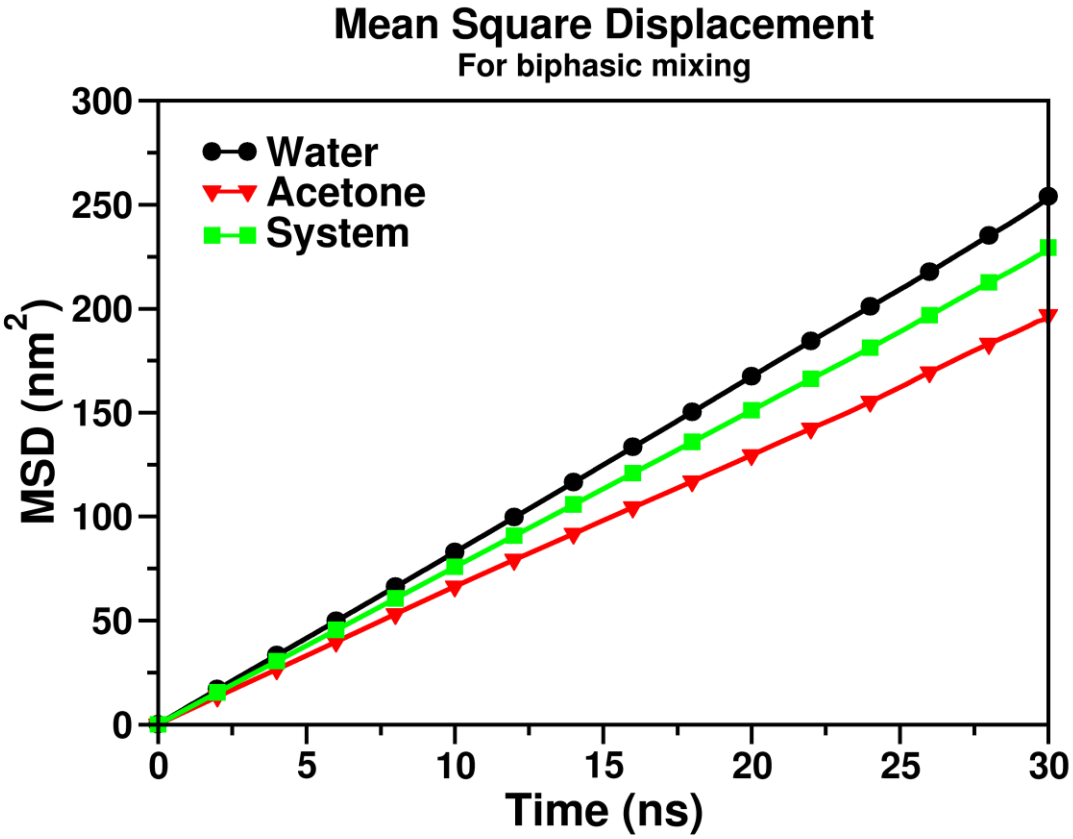

Figure 4. 25. The evolution of mean square displacement (MSD) for water, acetone, and the system.

Table 4. 1. The diffusion constant of water, acetone, and the system in simulation

Molecule Name	Diffusion Constant (1e-5 cm^2/s)
Water	1.4007 ± 0.0221
Acetone	1.0713 ± 0.0119
System	1.2583 ± 0.0074

4.2.4.2.Possible mechanism for peptide encapsulation

However, a force-field compatibility issue withheld us from simulating a system that includes water, acetone and WA30 peptides. Nevertheless, based on the simulation evidence and physical reasoning, we came up with a possible mechanism for peptide encapsulation: by adding sufficient acetone into peptide solution, it generates a rapid change of composition near the biphasic interface. This change may drive the pre-assembled WA30 coacervates into a larger, dense, coacervate phase. Meanwhile, this process will possibly enhance the β-sheet formation, leading to a tighter assembly of WA30 in the coacervate phase. Due to WA30's preference to self-assemble orientationally in water, the resulting WA30 coacervate may take the shape of a membrane instead of a solid bead. A planar membrane has free edges exposed to the water-acetone mixture, which is energetically unfavorable. Hence, the coacervate membrane may spontaneously enclose to form a sealed compartment to reduce free energy, similar to the strategy of a phospholipid bilayer to form an enclosed vesicle. [175, 176]. Although challenging, we plan to further study the behavior of WA30 coacervate near the rapid changing water-acetone interface, with a special focus on the higher-level assembly and the evolution of β-sheet secondary structures.

4.3. Summary

In this chapter, we first performed MD simulation of a single WA30 in water and compared it with the NMR result, confirming the validity of our MD model. Next, we augmented the simulation system to study the interaction of eight WA30 peptides in water. We found all eight WA30 peptides self-assembled along a fixed direction into a stable, rod-like coacervate. Secondary structure of WA-30 peptides shows negligible changes after self-assembly. Short, persistent, intermolecular, and intramolecular β-sheet secondary structures were found in the WA30 coacervate, at the flexible domains near the termini of WA30 peptides. ThT and FTIR experiments also confirmed the existence of β-sheet secondary structure prior to and after encapsulation. We hypothesize that the self-assembly/coacervation of WA30 is driven by the hydrophobic interactions of Tryptophan (W) residues and intermolecular H-bond formation. More specifically, the hydrophobic Tryptophan (W) residues drive neighboring WA30 peptides together, until intermolecular H-bonds form between the donors and acceptors on the flexible domains of each peptide, further stabilizing the assembly. MD trajectories, RMSD and RMSF measurements all confirm the above hypothesis. Finally, we wrapped up with a MD simulation of water-acetone mixing, which is the key to the encapsulation of WA30 peptide. Using a standard biphasic-mixing setup, we successfully reproduced the diffusion coefficient for acetone in water at room temperature. However, due to a force-field compatibility issue, we are yet unable to simulate a system which accommodates water, acetone and WA30 peptides. Nevertheless, based on the simulation evidence and physical reasoning, we proposed a possible mechanism for the encapsulation process of WA30 peptides.

To sum up, a combination of MD simulations, experiments, along with physical reasoning, has provided sufficient evidence for the proposed mechanisms of peptide coacervation and encapsulation into hollow spheres. This discovery may shed light on a broad range of opportunities for further research, i.e., single-point mutation to achieve hollow sphere formation of difference size and wall-thickness, the drug delivery capability of assembled hollow spheres, cell uptake and biocompatibility, etc.

Chapter 5

Conclusions and Perspectives

5.1. Concluding remarks

Using atomistic modeling and simulations, we have investigated the bio-nano-interaction mechanism in cell-nanomaterial interactions, biosurfactant aided liquid-phase exfoliation, as well as peptide coacervation and encapsulation. The scientific findings for each chapter are summarized as follows.

In chapter 2, with the state-of-the-art modeling, we have discovered a unique interaction mechanism between hBN flakes and lipid membrane: a sharp hBN could penetrate a lipid bilayer and form a cross-membrane water channel along its exposed polar edges. In contrast, a round hBN sheet could not penetrate a lipid bilayer due to high energy barrier and a lack of long enough polar edges. The discovery allows us to hypothesize a new mechanism of cytotoxicity of hBN: water channels induced lysosomal membrane permeabilization. The hypothesis was confirmed experimentally. The water channel mechanism is fundamentally different from all known membrane damaging mechanisms of 2D materials and may have general implications for all binary or multielement 2D materials with polar edges.

In chapter 3, our simulations of biosurfactant self-assembly on the interface of liquid-phase exfoliation (LPE) of hBN demonstrate that two types of biosurfactants, Flavin mononucleotide (FMN) and Sodium Cholate (SC), could self-assemble on the basal plane

of hBN via a toolbox of mechanisms including: π-π interactions, intermolecular hydrogen bonds, and hydrophobic interactions. We have conducted free energy calculations (FEC) to pinpoint the driving forces for biosurfactant self-assembly. FEC reveal that FMN to be superior to SC in assisting LPE of hBN. Experimental evidence has confirmed the theoretical and simulation results. Both surfactant molecules might be useful in the scalable production of other 2D materials. A general guideline was provided to aid the design of novel surfactant molecules for more efficient LPE of 2D materials, and the development of novel nanomedicine delivery systems.

In chapter 4, we have unraveled the molecular mechanisms of coacervation and encapsulation with a designed peptide, WA30. Our simulations show that WA30 peptides could self-assemble along a fixed direction into a stable, rod-like coacervate with negligible changes to the overall secondary structures. Short, persistent, intermolecular, and intramolecular β-sheet secondary structures were found in the WA30 coacervate, at the flexible domains near the termini of peptide chains. Two driving forces for peptide coacervation were identified: (1) the Tryptophan (W) residues drive neighboring WA30 peptides together due to hydrophobic interactions, and (2) intermolecular H-bonds form between the donors and acceptors on the flexible domains of neighboring peptides (pulled together by W-W stacking), further stabilizing the assembly. With MD simulation on biphasic mixing of acetone and water, we successfully reproduced the diffusion coefficient for acetone in water at room temperature, and discovered a rapid change of concentration near the biphasic interface. Based on these findings, we proposed a molecular mechanism to the encapsulation process. A combination of MD simulations, experiments, along with

physical reasoning, has provided sufficient evidence for the proposed mechanisms of peptide coacervation and encapsulation into hollow spheres.

5.2. Outlook of future research

It has been demonstrated that a fundamental understanding of bio-nano-interaction is important to biomedical and pharmaceutical applications, bioimaging, nanotechnology, safety, and regulation. Underlying mechanics and molecular mechanisms in three case studies of bio-nano-systems were discussed in this thesis. Knowledge acquired from these systems may have general implications. However, there are still many open questions and promising opportunities, a few of which are listed below.

(1) In the study of hBN - lipid membrane interaction, we have discovered cross-membrane water channels, with diameter of nanometers, *in silico*; however, it is beyond current experimental capabilities to directly visualize the water channels *in vitro*, due in part to the lack of high-resolution *in situ* imaging methods and the close-to-transparent appearance of hBN under TEM. Nevertheless, it will be significant to come up with a novel method to detect such water channels in experiment.

(2) The cross-membrane water channels are induced by the polar edges of c-hBN; however, this may prove to be generic. It will be worthwhile to study if the water channel mechanism still holds for other emerging, binary or multielement 2D materials with polar edges.

(3) Furthermore, the discovery of water channel mechanism may open a range of opportunities for future research, which, for instance, include strategies to functionalize hBN to achieve tunable channels and membrane permeability and cytotoxicity: for biomedical applications (such as drug delivery) which require low cytotoxicity of the nanomaterials, the polar edges should be shielded to inhibit the formation of cross-membrane water channels; for anticancer therapy and antibacterial practices, the polar edges should be exposed to maximize water channel formation, thereby inducing cytotoxicity to the target cells.

(4) In cell-nanomaterial interactions, size effect is an important factor. It will be worthwhile to study how the size of c-hBN affect the free energy evolution for hBN to pierce a lipid membrane. In addition, we only studied monolayer hBN piercing. It will be interesting to simulate multilayer c-hBN's interaction with lipid membrane: will it still induce a water channel? If so, is the radius of new water channel becoming larger?

(5) Apart from the size effect, temperature is also crucial to the water channel formation. The dynamics of a lipid membrane depend on temperature. In the simulation of chapter 2, we used POPC lipid molecules to model the lysosomal membrane. The phase transition temperature of POPC is lower than the room temperature (300 K, used in our simulation). It will be interesting to learn if the water channel formation could be enhanced by increasing the simulation temperature to beyond 300 K (such as the human body temperature) or inhibited by decreasing temperature to less than the gel point of POPC or other lipid membranes.

(6) In the study of biosurfactant-hBN interaction, we have demonstrated that FMN and SC molecules are both efficient in assisting LPE of hBN in water; however, these surfactants may be also useful in LPE of other 2D materials, which will be worthwhile to study both experimentally and computationally. It will also be interesting to explore biosurfactants' effect in safety, biocompatibility, and effectiveness of novel delivery systems.

(7) As we demonstrate in chapter 4, the repetitive peptide WA30 could coacervate and encapsulate into hollow spheres at room temperature; however, what is the behavior of WA30 coacervate following the exposure to acetone? Although challenging, a molecular picture of the WA30 coacervate near the rapid changing water-acetone interface, especially the higher-level assembly of WA30 coacervates and the evolution of β-sheet secondary structures, would be our final and crucial piece of puzzle to the understanding of WA30 peptide encapsulation process.

(8) Concurrently to our study in chapter 4, there has been increasing evidence that many naturally occurred bio-fabrication processes are enabled by peptide/protein coacervation [177-180]. What intrinsic properties or governing roles would ensure the coacervation? These are questions that need to be answered before the artificial design of peptide coacervation systems.

(9) Nowadays, Artificial Intelligence (AI) has given an enormous rise to applications in *de novo* design of peptide, drug discovery and design [181-183]. Is it possible for AI to aid the modeling of peptide coacervation and encapsulation in chapter 4? Furthermore, can AI help to screen, design, and optimize *de novo* peptides with a

focus to achieve enhanced functionality and precise control of coacervation and encapsulation?

Bibliography

1. Hui, Y., et al., *Role of Nanoparticle Mechanical Properties in Cancer Drug Delivery.* ACS Nano, 2019. **13**(7): p. 7410-7424.
2. Gu, W., et al., *Actively targeted nanomedicines for precision cancer therapy: Concept, construction, challenges and clinical translation.* J Control Release, 2021. **329**: p. 676-695.
3. Kim, W., et al., *A new class of synthetic retinoid antibiotics effective against bacterial persisters.* Nature, 2018. **556**(7699): p. 103-107.
4. Domi, B., et al., *Assessment of Physico-Chemical and Toxicological Properties of Commercial 2D Boron Nitride Nanopowder and Nanoplatelets.* Int J Mol Sci, 2021. **22**(2): p. 567.
5. Lucherelli, M.A., et al., *Boron Nitride Nanosheets Can Induce Water Channels Across Lipid Bilayers Leading to Lysosomal Permeabilization.* Adv Mater, 2021: p. e2103137.
6. Bastus, N.G. and V. Puntes, *Nanosafety: Towards Safer Nanoparticles by Design.* Current Medicinal Chemistry, 2018. **25**(35): p. 4587-4601.
7. Fadeel, B., et al., *Safety Assessment of Graphene-Based Materials: Focus on Human Health and the Environment.* Acs Nano, 2018. **12**(11): p. 10582-10620.
8. Mitrano, D.M., et al., *Review of nanomaterial aging and transformations through the life cycle of nano-enhanced products.* Environ Int, 2015. **77**: p. 132-47.
9. Lacerda, L., et al., *How do functionalized carbon nanotubes land on, bind to and pierce through model and plasma membranes.* Nanoscale, 2013. **5**(21): p. 10242-10250.
10. Li, Y., et al., *Graphene microsheets enter cells through spontaneous membrane penetration at edge asperities and corner sites.* Proc Natl Acad Sci U S A, 2013. **110**(30): p. 12295-300.
11. Shi, X.H., et al., *Cell entry of one-dimensional nanomaterials occurs by tip recognition and rotation.* Nature Nanotechnology, 2011. **6**(11): p. 714-719.
12. Tu, Y., et al., *Destructive extraction of phospholipids from Escherichia coli membranes by graphene nanosheets.* Nat Nanotechnol, 2013. **8**(8): p. 594-601.
13. Zhang, S.L., et al., *Size-Dependent Endocytosis of Nanoparticles.* Advanced Materials, 2009. **21**(4): p. 419-+.
14. Chu, Z., et al., *Unambiguous observation of shape effects on cellular fate of nanoparticles.* Sci Rep, 2014. **4**: p. 4495.
15. Ma, X.W., et al., *Future of nanotherapeutics: Targeting the cellular sub-organelles.* Biomaterials, 2016. **97**: p. 10-21.
16. Stern, S.T., P.P. Adiseshaiah, and R.M. Crist, *Autophagy and lysosomal dysfunction as emerging mechanisms of nanomaterial toxicity.* Particle and Fibre Toxicology, 2012. **9**.
17. Zou, G., et al., *Packing of flexible 2D materials in vesicles.* Journal of Physics D: Applied Physics, 2018. **51**(22): p. 224001.

18. Elbaum, M., D.K. Fygenson, and A. Libchaber, *Buckling microtubules in vesicles.* Physical Review Letters, 1996. **76**(21): p. 4078-4081.
19. Kraszewski, S., et al., *Insertion of Short Amino-Functionalized Single-Walled Carbon Nanotubes into Phospholipid Bilayer Occurs by Passive Diffusion.* Plos One, 2012. **7**(7).
20. Murphy, F.A., et al., *Length-Dependent Retention of Carbon Nanotubes in the Pleural Space of Mice Initiates Sustained Inflammation and Progressive Fibrosis on the Parietal Pleura.* American Journal of Pathology, 2011. **178**(6): p. 2587-2600.
21. Hilder, T.A. and N. Gaston, *Interaction of Boron Nitride Nanosheets with Model Cell Membranes.* Chemphyschem, 2016. **17**(11): p. 1573-8.
22. Ma, L., et al., *In vivo toxicity evaluation of boron nitride nanosheets in Bombyx mori silkworm model.* Chemosphere, 2020. **247**: p. 125877.
23. Merlo, A., et al., *Boron nitride nanomaterials: biocompatibility and bio-applications.* Biomaterials Science, 2018. **6**(9): p. 2298-2311.
24. Huang, X., Z. Zeng, and H. Zhang, *Metal dichalcogenide nanosheets: preparation, properties and applications.* Chemical Society Reviews, 2013. **42**(5): p. 1934.
25. Li, Y.Y., et al., *Nanocellulose as green dispersant for two-dimensional energy materials.* Nano Energy, 2015. **13**: p. 346-354.
26. McManus, D., et al., *Water-based and biocompatible 2D crystal inks for all-inkjet-printed heterostructures.* Nature Nanotechnology, 2017. **12**(4): p. 343-350.
27. Yao, Y., et al., *High-Concentration Aqueous Dispersions of MoS2.* Advanced Functional Materials, 2013. **23**(28): p. 3577-3583.
28. Lotya, M., et al., *High-Concentration, Surfactant-Stabilized Graphene Dispersions.* ACS Nano, 2010. **4**(6): p. 3155-3162.
29. Griffin, A., et al., *Effect of Surfactant Choice and Concentration on the Dimensions and Yield of Liquid-Phase-Exfoliated Nanosheets.* Chemistry of Materials, 2020. **32**(7): p. 2852-2862.
30. Ruiz, A., et al., *Toxicological evaluation of highly water dispersible few-layer graphene in vivo.* Carbon, 2020. **170**: p. 347-360.
31. Hou, X., et al., *Lipid nanoparticles for mRNA delivery.* Nature Reviews Materials, 2021.
32. O'Hagan, D.T. and N.M. Valiante, *Recent advances in the discovery and delivery of vaccine adjuvants.* Nature Reviews Drug Discovery, 2003. **2**(9): p. 727-735.
33. Ezhilarasi, P.N., et al., *Nanoencapsulation Techniques for Food Bioactive Components: A Review.* Food and Bioprocess Technology, 2013. **6**(3): p. 628-647.
34. Nuruzzaman, M., et al., *Nanoencapsulation, Nano-guard for Pesticides: A New Window for Safe Application.* Journal of Agricultural and Food Chemistry, 2016. **64**(7): p. 1447-1483.
35. Kumari, A., et al., *NANOENCAPSULATION FOR DRUG DELIVERY.* Excli Journal, 2014. **13**: p. 265-286.
36. Shchukina, E.M., et al., *Nanoencapsulation of phase change materials for advanced thermal energy storage systems.* Chemical Society Reviews, 2018. **47**(11): p. 4156-4175.
37. Abbas, M., et al., *Peptide-based coacervates as biomimetic protocells.* Chemical Society Reviews, 2021. **50**(6): p. 3690-3705.

38. Black, K.A., et al., *Protein Encapsulation via Polypeptide Complex Coacervation.* ACS Macro Letters, 2014. **3**(10): p. 1088-1091.
39. Russier, J., et al., *Evidencing the mask effect of graphene oxide: a comparative study on primary human and murine phagocytic cells.* Nanoscale, 2013. **5**(22): p. 11234-11247.
40. Wang, Z., et al., *Biological and environmental interactions of emerging two-dimensional nanomaterials.* Chem Soc Rev, 2016. **45**(6): p. 1750-80.
41. Liao, K.H., et al., *Cytotoxicity of graphene oxide and graphene in human erythrocytes and skin fibroblasts.* ACS Appl Mater Interfaces, 2011. **3**(7): p. 2607-15.
42. Meyer, D.E., M.A. Curran, and M.A. Gonzalez, *An Examination of Existing Data for the Industrial Manufacture and Use of Nanocomponents and Their Role in the Life Cycle Impact of Nanoproducts.* Environmental Science & Technology, 2009. **43**(5): p. 1256-1263.
43. Sasidharan, A., et al., *Differential nano-bio interactions and toxicity effects of pristine versus functionalized graphene.* Nanoscale, 2011. **3**(6): p. 2461-2464.
44. Zhou, R.H. and H.J. Gao, *Cytotoxicity of graphene: recent advances and future perspective.* Wiley Interdisciplinary Reviews-Nanomedicine and Nanobiotechnology, 2014. **6**(5): p. 452-474.
45. Aftab, S., et al., *Two-dimensional electronic devices modulated by the activation of donor-like states in boron nitride.* Nanoscale, 2020. **12**(35): p. 18171-18179.
46. Dean, C.R., et al., *Boron nitride substrates for high-quality graphene electronics.* Nature Nanotechnology, 2010. **5**(10): p. 722-726.
47. Jiang, X.-F., et al., *Recent Progress on Fabrications and Applications of Boron Nitride Nanomaterials: A Review.* Journal of Materials Science & Technology, 2015. **31**(6): p. 589-598.
48. Deb, J. and U. Sarkar, *Boron-nitride and boron-phosphide doped twin-graphene: Applications in electronics and optoelectronics.* Applied Surface Science, 2021. **541**: p. 148657.
49. Gu, J., et al., *Synergistic improvement of thermal conductivities of polyphenylene sulfide composites filled with boron nitride hybrid fillers.* Composites Part A: Applied Science and Manufacturing, 2017. **95**: p. 267-273.
50. Zhang, W., et al., *Van der Waals stacked 2D layered materials for optoelectronics.* 2D Materials, 2016. **3**(2): p. 022001.
51. Lu, T., et al., *Hexagonal boron nitride nanoplates as emerging biological nanovectors and their potential applications in biomedicine.* Journal of Materials Chemistry B, 2016. **4**(36): p. 6103-6110.
52. Cheng, C.C., et al., *Dual stimuli-responsive supramolecular boron nitride with tunable physical properties for controlled drug delivery.* Nanoscale, 2019. **11**(21): p. 10393-10401.
53. Ikram, M., et al., *Bactericidal behavior of chemically exfoliated boron nitride nanosheets doped with zirconium.* Applied Nanoscience, 2020. **10**(7): p. 2339-2349.
54. Onyszko, M., et al., *Few Layered Oxidized h-BN as Nanofiller of Cellulose-Based Paper with Superior Antibacterial Response and Enhanced Mechanical/Thermal Performance.* International Journal of Molecular Sciences, 2020. **21**(15).

55. Liu, S., et al., *Cytotoxicity and Efflux Pump Inhibition Induced by Molybdenum Disulfide and Boron Nitride Nanomaterials with Sheetlike Structure.* Environ Sci Technol, 2017. **51**(18): p. 10834-10842.
56. Czarniewska, E., et al., *Non-cytotoxic hydroxyl-functionalized exfoliated boron nitride nanoflakes impair the immunological function of insect haemocytes in vivo.* Sci Rep, 2019. **9**(1): p. 14027.
57. Thomas, M., M. Enciso, and T.A. Hilder, *Insertion Mechanism and Stability of Boron Nitride Nanotubes in Lipid Bilayers.* Journal of Physical Chemistry B, 2015. **119**(15): p. 4929-4936.
58. Li, Z., et al., *Temperature-Dependent Lipid Extraction from Membranes by Boron Nitride Nanosheets.* ACS Nano, 2018. **12**(3): p. 2764-2772.
59. Abraham, M.J., et al., *GROMACS: High performance molecular simulations through multi-level parallelism from laptops to supercomputers.* SoftwareX, 2015. **1**: p. 19-25.
60. M.J. Abraham, D.v.d.S., E. Lindahl, B. Hess, and the GROMACS development team, *GROMACS User Manual version 2018.* 2018.
61. Hilder, T.A., et al., *Validity of current force fields for simulations on boron nitride nanotubes.* Micro & Nano Letters, 2010. **5**(2): p. 150-156.
62. Kamath, G. and G.A. Baker, *Are ionic liquids suitable media for boron nitride exfoliation and dispersion? Insight via molecular dynamics.* RSC Advances, 2013. **3**(22): p. 8197-8202.
63. Wu, Y., L.K. Wagner, and N.R. Aluru, *Hexagonal boron nitride and water interaction parameters.* J Chem Phys, 2016. **144**(16): p. 164118.
64. Van Meer, G., D.R. Voelker, and G.W. Feigenson, *Membrane lipids: where they are and how they behave.* Nature reviews Molecular cell biology, 2008. **9**(2): p. 112-124.
65. Berger, O., O. Edholm, and F. Jahnig, *Molecular dynamics simulations of a fluid bilayer of dipalmitoylphosphatidylcholine at full hydration, constant pressure, and constant temperature.* Biophys J, 1997. **72**(5): p. 2002-13.
66. Anézo, C., et al., *Methodological Issues in Lipid Bilayer Simulations.* The Journal of Physical Chemistry B, 2003. **107**(35): p. 9424-9433.
67. Benz, R.W., et al., *Experimental validation of molecular dynamics simulations of lipid bilayers: a new approach.* Biophys J, 2005. **88**(2): p. 805-17.
68. Kandt, C., W.L. Ash, and D.P. Tieleman, *Setting up and running molecular dynamics simulations of membrane proteins.* Methods, 2007. **41**(4): p. 475-88.
69. Zhu, W., et al., *Nanomechanical mechanism for lipid bilayer damage induced by carbon nanotubes confined in intracellular vesicles.* Proc Natl Acad Sci U S A, 2016. **113**(44): p. 12374-12379.
70. Berendsen, H.J.C., J.R. Grigera, and T.P. Straatsma, *The missing term in effective pair potentials.* The Journal of Physical Chemistry, 1987. **91**(24): p. 6269-6271.
71. Essmann, U., et al., *A smooth particle mesh Ewald method.* The Journal of chemical physics, 1995. **103**(19): p. 8577-8593.
72. Leekumjorn, S. and A.K. Sum, *Molecular characterization of gel and liquid-crystalline structures of fully hydrated POPC and POPE bilayers.* J Phys Chem B, 2007. **111**(21): p. 6026-33.

73. Litman, B.J., E.N. Lewis, and I.W. Levin, *Packing characteristics of highly unsaturated bilayer lipids: Raman spectroscopic studies of multilamellar phosphatidylcholine dispersions.* Biochemistry, 1991. **30**(2): p. 313-9.
74. Humphrey, W., A. Dalke, and K. Schulten, *VMD: Visual molecular dynamics.* Journal of Molecular Graphics & Modelling, 1996. **14**(1): p. 33-38.
75. Hub, J.S., et al., *Potentials of Mean Force and Permeabilities for Carbon Dioxide, Ammonia, and Water Flux across a Rhesus Protein Channel and Lipid Membranes.* Journal of the American Chemical Society, 2010. **132**(38): p. 13251-13263.
76. Kumar, S., et al., *THE weighted histogram analysis method for free-energy calculations on biomolecules. I. The method.* Journal of Computational Chemistry, 1992. **13**(8): p. 1011-1021.
77. Helms, V. and R.C. Wade, *Computational Alchemy To Calculate Absolute Protein−Ligand Binding Free Energy.* Journal of the American Chemical Society, 1998. **120**(12): p. 2710-2713.
78. Gu, Z., et al., *Membrane Insertion and Phospholipids Extraction by Graphyne Nanosheets.* The Journal of Physical Chemistry C, 2017. **121**(4): p. 2444-2450.
79. Shirts, M.R. and J.D. Chodera, *Statistically optimal analysis of samples from multiple equilibrium states.* The Journal of Chemical Physics, 2008. **129**(12): p. 124105.
80. Khan, A.F., et al., *Surfactant-exfoliated 2D hexagonal boron nitride (2D-hBN): role of surfactant upon the electrochemical reduction of oxygen and capacitance applications.* Journal of Materials Chemistry A, 2017. **5**(8): p. 4103-4113.
81. Smith, R.J., et al., *Large-Scale Exfoliation of Inorganic Layered Compounds in Aqueous Surfactant Solutions.* Advanced Materials, 2011. **23**(34): p. 3944-+.
82. Song, L., et al., *Large scale growth and characterization of atomic hexagonal boron nitride layers.* Nano Lett, 2010. **10**(8): p. 3209-15.
83. Kurapati, R., et al., *White Graphene undergoes Peroxidase Degradation.* Angewandte Chemie-International Edition, 2016. **55**(18): p. 5506-5511.
84. Matovic, B., et al., *Synthesis and characterization of nanocrystaline hexagonal boron nitride powders: XRD and luminescence properties.* Ceramics International, 2016. **42**(15): p. 16655-16658.
85. Kettiger, H., et al., *Engineered nanomaterial uptake and tissue distribution: from cell to organism.* Int J Nanomedicine, 2013. **8**: p. 3255-69.
86. Jordans, S., et al., *Monitoring compartment-specific substrate cleavage by cathepsins B, K, L, and S at physiological pH and redox conditions.* BMC Biochem, 2009. **10**(1): p. 23.
87. Reiners, J.J., Jr., et al., *Release of cytochrome c and activation of pro-caspase-9 following lysosomal photodamage involves Bid cleavage.* Cell Death Differ, 2002. **9**(9): p. 934-44.
88. Akhavan, O. and E. Ghaderi, *Toxicity of graphene and graphene oxide nanowalls against bacteria.* ACS Nano, 2010. **4**(10): p. 5731-6.
89. Zhang, Y., et al., *Cytotoxicity effects of graphene and single-wall carbon nanotubes in neural phaeochromocytoma-derived PC12 cells.* ACS Nano, 2010. **4**(6): p. 3181-6.

90. Li, Y., et al., *The triggering of apoptosis in macrophages by pristine graphene through the MAPK and TGF-a,c signaling pathways.* Biomaterials, 2012. **33**(2): p. 402-11.
91. Chang, Y., et al., *In vitro toxicity evaluation of graphene oxide on A549 cells.* Toxicol Lett, 2011. **200**(3): p. 201-10.
92. Yue, H., et al., *The role of the lateral dimension of graphene oxide in the regulation of cellular responses.* Biomaterials, 2012. **33**(16): p. 4013-4021.
93. Luan, B.Q., et al., *Potential Toxicity of Graphene to Cell Functions via Disrupting Protein-Protein Interactions.* Acs Nano, 2015. **9**(1): p. 663-669.
94. Akhavan, O., E. Ghaderi, and A. Akhavan, *Size-dependent genotoxicity of graphene nanoplatelets in human stem cells.* Biomaterials, 2012. **33**(32): p. 8017-8025.
95. Yuan, J.F., et al., *Cytotoxicity Evaluation of Oxidized Single-Walled Carbon Nanotubes and Graphene Oxide on Human Hepatoma HepG2 cells: An iTRAQ-Coupled 2D LC-MS/MS Proteome Analysis.* Toxicological Sciences, 2012. **126**(1): p. 149-161.
96. Ono, K., S.O. Kim, and J. Han, *Susceptibility of lysosomes to rupture is a determinant for plasma membrane disruption in tumor necrosis factor alpha-induced cell death.* Mol Cell Biol, 2003. **23**(2): p. 665-76.
97. Tunuguntla, R.H., et al., *Ultrafast proton transport in sub-1-nm diameter carbon nanotube porins.* Nat Nanotechnol, 2016. **11**(7): p. 639-44.
98. Geng, J., et al., *Stochastic transport through carbon nanotubes in lipid bilayers and live cell membranes.* Nature, 2014. **514**(7524): p. 612-5.
99. Liu, L., et al., *Graphene nanosheets damage the lysosomal and mitochondrial membranes and induce the apoptosis of RBL-2H3 cells.* Sci Total Environ, 2020. **734**: p. 139229.
100. Zhang, C., et al., *The interrupted effect of autophagic flux and lysosomal function induced by graphene oxide in p62-dependent apoptosis of F98 cells.* J Nanobiotechnology, 2020. **18**(1): p. 52.
101. Wang, F., R. Gomez-Sintes, and P. Boya, *Lysosomal membrane permeabilization and cell death.* Traffic, 2018. **19**(12): p. 918-931.
102. Bové, J., et al., *BAX channel activity mediates lysosomal disruption linked to Parkinson disease.* Autophagy, 2014. **10**(5): p. 889-900.
103. Muller, R.H. and C.M. Keck, *Challenges and solutions for the delivery of biotech drugs – a review of drug nanocrystal technology and lipid nanoparticles.* Journal of Biotechnology, 2004. **113**(1): p. 151-170.
104. Aldeghi, M., et al., *Accurate calculation of the absolute free energy of binding for drug molecules.* Chem Sci, 2016. **7**(1): p. 207-218.
105. Hu, C.-X., et al., *Dispersant-assisted liquid-phase exfoliation of 2D materials beyond graphene.* Nanoscale, 2021. **13**(2): p. 460-484.
106. Schlierf, A., et al., *Nanoscale insight into the exfoliation mechanism of graphene with organic dyes: effect of charge, dipole and molecular structure.* Nanoscale, 2013. **5**(10): p. 4205.
107. Massey, V., *The Chemical and Biological Versatility of Riboflavin.* Biochemical Society Transactions, 2000. **28**(4): p. 283-296.
108. Stryer, L., *Biochemistry 4th ed, New York.* 1995, WH Freeman and Co.

109. Walsh, C., *Flavin coenzymes: at the crossroads of biological redox chemistry.* Accounts of Chemical Research, 1980. **13**(5): p. 148-155.
110. Ju, S.-Y., et al., *Selection of carbon nanotubes with specific chiralities using helical assemblies of flavin mononucleotide.* Nature Nanotechnology, 2008. **3**(6): p. 356-362.
111. Ju, S.-Y. and F. Papadimitrakopoulos, *Synthesis and Redox Behavior of Flavin Mononucleotide-Functionalized Single-Walled Carbon Nanotubes.* Journal of the American Chemical Society, 2008. **130**(2): p. 655-664.
112. Yoon, W., et al., *Graphene nanoribbons formed by a sonochemical graphene unzipping using flavin mononucleotide as a template.* Carbon, 2015. **81**: p. 629-638.
113. Ayán-Varela, M., et al., *Achieving Extremely Concentrated Aqueous Dispersions of Graphene Flakes and Catalytically Efficient Graphene-Metal Nanoparticle Hybrids with Flavin Mononucleotide as a High-Performance Stabilizer.* ACS Applied Materials & Interfaces, 2015. **7**(19): p. 10293-10307.
114. Zhi, C., et al., *Large-Scale Fabrication of Boron Nitride Nanosheets and Their Utilization in Polymeric Composites with Improved Thermal and Mechanical Properties.* Advanced Materials, 2009. **21**(28): p. 2889-2893.
115. Ciesielski, A. and P. Samorì, *Grapheneviasonication assisted liquid-phase exfoliation.* Chem. Soc. Rev., 2014. **43**(1): p. 381-398.
116. Chae, A., et al., *Enhanced dispersion of boron nitride nanosheets in aqueous media by using bile acid-based surfactants.* Materials Research Express, 2018. **5**(1): p. 015036.
117. Gao, Z., et al., *Noncovalent Functionalization of Disentangled Boron Nitride Nanotubes with Flavin Mononucleotides for Strong and Stable Visible-Light Emission in Aqueous Solution.* ACS Applied Materials & Interfaces, 2011. **3**(3): p. 627-632.
118. Gao, Z., et al., *Noncovalent Functionalization of Boron Nitride Nanotubes in Aqueous Media Opens Application Roads in Nanobiomedicine.* Nanobiomedicine, 2014. **1**: p. 7.
119. Smith Mcwilliams, A.D., et al., *Understanding the Exfoliation and Dispersion of Hexagonal Boron Nitride Nanosheets by Surfactants: Implications for Antibacterial and Thermally Resistant Coatings.* ACS Applied Nano Materials, 2021. **4**(1): p. 142-151.
120. Malde, A.K., et al., *An Automated Force Field Topology Builder (ATB) and Repository: Version 1.0.* Journal of Chemical Theory and Computation, 2011. **7**(12): p. 4026-4037.
121. Schmid, N., et al., *Definition and testing of the GROMOS force-field versions 54A7 and 54B7.* European Biophysics Journal, 2011. **40**(7): p. 843-856.
122. Deng, J.-H., et al., *π-π stacking interactions: Non-negligible forces for stabilizing porous supramolecular frameworks.* Science Advances, 2020. **6**(2): p. eaax9976.
123. Lee, B. and F.M. Richards, *The interpretation of protein structures: Estimation of static accessibility.* Journal of Molecular Biology, 1971. **55**(3): p. 379-IN4.
124. Chen, H. and A.Z. Panagiotopoulos, *Molecular Modeling of Surfactant Micellization Using Solvent-Accessible Surface Area.* Langmuir, 2019. **35**(6): p. 2443-2450.

125. Syed Ausaf, A., et al., *A Review of Methods Available to Estimate Solvent-Accessible Surface Areas of Soluble Proteins in the Folded and Unfolded States.* Current Protein & Peptide Science, 2014. **15**(5): p. 456-476.
126. Sarma, R.H., P. Dannies, and N.O. Kaplan, *Investigations of inter- and intramolecular interactions in flavine-adenine dinucleotide by proton magnetic resonance.* Biochemistry, 1968. **7**(12): p. 4359-4367.
127. Kainosho, M. and Y. Kyogoku, *High-resolution proton and phosphorus nuclear magnetic resonance spectra of flavine adenine dinucleotide and its conformation in aqueous solution.* Biochemistry, 1972. **11**(5): p. 741-752.
128. Ju, S.Y., W.P. Kopcha, and F. Papadimitrakopoulos, *Brightly Fluorescent Single-Walled Carbon Nanotubes via an Oxygen-Excluding Surfactant Organization.* Science, 2009. **323**(5919): p. 1319-1323.
129. Oh, H., J. Sim, and S.-Y. Ju, *Binding Affinities and Thermodynamics of Noncovalent Functionalization of Carbon Nanotubes with Surfactants.* Langmuir, 2013. **29**(35): p. 11154-11162.
130. Bailey, S., et al., *A study of planar anchor groups for graphene-based single-molecule electronics.* The Journal of Chemical Physics, 2014. **140**(5): p. 054708.
131. Robinson, B.J., et al., *Formation of Two-Dimensional Micelles on Graphene: Multi-Scale Theoretical and Experimental Study.* ACS Nano, 2017. **11**(3): p. 3404-3412.
132. Zhao, W., et al., *Graphene and Flavin Mononucleotide Interaction in Aqueous Graphene Dispersions.* The Journal of Physical Chemistry C, 2019. **123**(43): p. 26282-26288.
133. Grajek, H., et al., *Flavin mononucleotide fluorescence intensity decay in concentrated aqueous solutions.* Chemical Physics Letters, 2007. **439**(1-3): p. 151-156.
134. Ciesielski, A. and P. Samorì, *Supramolecular Approaches to Graphene: From Self-Assembly to Molecule-Assisted Liquid-Phase Exfoliation.* Advanced Materials, 2016. **28**(29): p. 6030-6051.
135. Lin, C.S., et al., *Geometric and Electronic Structures of Carbon Nanotubes Adsorbed with Flavin Adenine Dinucleotide: A Theoretical Study.* The Journal of Physical Chemistry C, 2007. **111**(11): p. 4069-4073.
136. Sim, J., et al., *Effect of tight flavin mononucleotide wrapping and its binding affinity on carbon nanotube covalent reactivities.* Physical Chemistry Chemical Physics, 2013. **15**(44): p. 19169.
137. Tao, H., et al., *Scalable exfoliation and dispersion of two-dimensional materials – an update.* Physical Chemistry Chemical Physics, 2017. **19**(2): p. 921-960.
138. Rostamabadi, H., S.R. Falsafi, and S.M. Jafari, *Nanoencapsulation of carotenoids within lipid-based nanocarriers.* Journal of Controlled Release, 2019. **298**: p. 38-67.
139. Katouzian, I. and S.M. Jafari, *Nano-encapsulation as a promising approach for targeted delivery and controlled release of vitamins.* Trends in Food Science & Technology, 2016. **53**: p. 34-48.
140. Zhu, M., R. Wang, and G. Nie, *Applications of nanomaterials as vaccine adjuvants.* Human Vaccines & Immunotherapeutics, 2014. **10**(9): p. 2761-2774.

141. Gagliardi, A., et al., *Biodegradable Polymeric Nanoparticles for Drug Delivery to Solid Tumors.* Frontiers in Pharmacology, 2021. **12**: p. 24.
142. Shanmugapriya, K., et al., *Astaxanthin-alpha tocopherol nanoemulsion formulation by emulsification methods: Investigation on anticancer, wound healing, and antibacterial effects.* Colloids and Surfaces B: Biointerfaces, 2018. **172**: p. 170-179.
143. Lim, F. and A.M. Sun, *MICROENCAPSULATED ISLETS AS BIOARTIFICIAL ENDOCRINE PANCREAS.* Science, 1980. **210**(4472): p. 908-910.
144. Lee, K.Y. and D.J. Mooney, *Alginate: Properties and biomedical applications.* Progress in Polymer Science, 2012. **37**(1): p. 106-126.
145. Axpe, E. and M. Oyen, *Applications of Alginate-Based Bioinks in 3D Bioprinting.* International Journal of Molecular Sciences, 2016. **17**(12): p. 1976.
146. Jiao, Y., et al., *Polypeptide – decorated nanoliposomes as novel delivery systems for lutein.* RSC Advances, 2018. **8**(55): p. 31372-31381.
147. Qu, W., et al., *Avidin–Biotin Interaction Mediated Peptide Assemblies as Efficient Gene Delivery Vectors for Cancer Therapy.* Molecular Pharmaceutics, 2013. **10**(1): p. 261-269.
148. Wicki, A., et al., *Nanomedicine in cancer therapy: Challenges, opportunities, and clinical applications.* Journal of Controlled Release, 2015. **200**: p. 138-157.
149. Ellis, R.J., *Macromolecular crowding: obvious but underappreciated.* Trends in Biochemical Sciences, 2001. **26**(10): p. 597-604.
150. Mitrea, D.M. and R.W. Kriwacki, *Phase separation in biology; functional organization of a higher order.* Cell Communication and Signaling, 2016. **14**(1).
151. Crowe, C.D. and C.D. Keating, *Liquid–liquid phase separation in artificial cells.* Interface Focus, 2018. **8**(5): p. 20180032.
152. Sarmento, B., et al., *Alginate/Chitosan Nanoparticles are Effective for Oral Insulin Delivery.* Pharmaceutical Research, 2007. **24**(12): p. 2198-2206.
153. Chu, H., et al., *Injectable fibroblast growth factor-2 coacervate for persistent angiogenesis.* Proceedings of the National Academy of Sciences, 2011. **108**(33): p. 13444-13449.
154. Guo, J., et al., *The Asian corn borerOstrinia furnacalisfeeding increases the direct and indirect defence of mid-whorl stage commercial maize in the field.* Plant Biotechnology Journal, 2019. **17**(1): p. 88-102.
155. Nafus, D.M. and I.H. Schreiner, *Location of Ostrinia furnacalis (Lepidoptera: Pyralidae) Eggs and Larvae on Sweet Corn in Relation to Plant Growth Stage.* Journal of Economic Entomology, 1987. **80**(2): p. 411-416.
156. Hill, D.S., *Pests of crops in warmer climates and their control*. 2008: Springer Science & Business Media.
157. Lindorff-Larsen, K., et al., *Improved side-chain torsion potentials for the Amber ff99SB protein force field.* Proteins: Structure, Function, and Bioinformatics, 2010. **78**(8): p. 1950-1958.
158. Jorgensen, W.L., et al., *Comparison of simple potential functions for simulating liquid water.* The Journal of Chemical Physics, 1983. **79**(2): p. 926-935.
159. Emperador, A., R. Crehuet, and E. Guàrdia, *Effect of the Water Model in Simulations of Protein–Protein Recognition and Association.* Polymers, 2021. **13**(2): p. 176.

160. Dawson, W.M., et al., *Structural resolution of switchable states of a de novo peptide assembly.* Nature Communications, 2021. **12**(1): p. 1530.
161. Parrinello, M. and A. Rahman, *Polymorphic transitions in single crystals: A new molecular dynamics method.* Journal of Applied Physics, 1981. **52**(12): p. 7182-7190.
162. Bussi, G., D. Donadio, and M. Parrinello, *Canonical sampling through velocity rescaling.* The Journal of Chemical Physics, 2007. **126**(1): p. 014101.
163. Bussi, G., T. Zykova-Timan, and M. Parrinello, *Isothermal-isobaric molecular dynamics using stochastic velocity rescaling.* The Journal of Chemical Physics, 2009. **130**(7): p. 074101.
164. Caleman, C., et al., *Force Field Benchmark of Organic Liquids: Density, Enthalpy of Vaporization, Heat Capacities, Surface Tension, Isothermal Compressibility, Volumetric Expansion Coefficient, and Dielectric Constant.* J Chem Theory Comput, 2012. **8**(1): p. 61-74.
165. Debye, P., *Interferenz von Röntgenstrahlen und Wärmebewegung.* Annalen der Physik, 1913. **348**(1): p. 49-92.
166. Waller, I., *Zur Frage der Einwirkung der Wärmebewegung auf die Interferenz von Röntgenstrahlen.* Zeitschrift für Physik, 1923. **17**(1): p. 398-408.
167. Sun, Z., et al., *Utility of B-Factors in Protein Science: Interpreting Rigidity, Flexibility, and Internal Motion and Engineering Thermostability.* Chemical Reviews, 2019. **119**(3): p. 1626-1665.
168. Fenwick, R.B., et al., *Integrated description of protein dynamics from room-temperature X-ray crystallography and NMR.* Proceedings of the National Academy of Sciences, 2014. **111**(4): p. E445-E454.
169. Reinknecht, C., et al., *Patterns in Protein Flexibility: A Comparison of NMR "Ensembles", MD Trajectories, and Crystallographic B-Factors.* Molecules, 2021. **26**(5): p. 1484.
170. Qian, H., M.P. Sheetz, and E.L. Elson, *Single particle tracking. Analysis of diffusion and flow in two-dimensional systems.* Biophysical Journal, 1991. **60**(4): p. 910-921.
171. Allen, M.P. and D.J. Tildesley, *Computer simulation of liquids*. 2017: Oxford university press.
172. Lavino, A.D., et al., *Extended Charge-On-Particle Optimized Potentials for Liquid Simulation Acetone Model: The Case of Acetone-Water Mixtures.* J Phys Chem B, 2018. **122**(20): p. 5234-5241.
173. Cussler, E.L. and E.L. Cussler, *Diffusion: mass transfer in fluid systems*. 2009: Cambridge university press.
174. Toryanik, A.I. and V.N. Taranenko, *MOLECULAR MOBILITY AND STRUCTURE IN WATER-ACETONE MIXTURES.* Journal of Structural Chemistry, 1987. **28**(5): p. 714-719.
175. Monnard, P.-A. and D.W. Deamer, *Membrane self-assembly processes: Steps toward the first cellular life.* The Anatomical Record, 2002. **268**(3): p. 196-207.
176. Alberts B, J.A., Lewis J, et al., *Molecular Biology of the Cell. 4th edition.* Garland Science, 2002.

177. Deepankumar, K., et al., *Liquid-Liquid Phase Separation of the Green Mussel Adhesive Protein Pvfp-5 is Regulated by the Post-Translated Dopa Amino Acid.* Adv Mater, 2021: p. e2103828.
178. Priemel, T., et al., *Rapid self-assembly of complex biomolecular architectures during mussel byssus biofabrication.* Nature Communications, 2017. **8**(1): p. 14539.
179. Amini, S., et al., *Preventing mussel adhesion using lubricant-infused materials.* Science, 2017. **357**(6352): p. 668-+.
180. Petrone, L., et al., *Mussel adhesion is dictated by time-regulated secretion and molecular conformation of mussel adhesive proteins.* Nature Communications, 2015. **6**(1): p. 8737.
181. Grisoni, F., et al., *De novo design of anticancer peptides by ensemble artificial neural networks.* Journal of Molecular Modeling, 2019. **25**(5).
182. Schneider, G., *Automating drug discovery.* Nature Reviews Drug Discovery, 2018. **17**(2): p. 97-113.
183. Jing, Y., et al., *Deep Learning for Drug Design: an Artificial Intelligence Paradigm for Drug Discovery in the Big Data Era.* The AAPS Journal, 2018. **20**(3).